

学位論文

A Measurement of Cosmic Ray Antiproton Flux

(宇宙線反陽子流束の測定)



平成8年 12月 博士(理学)申請

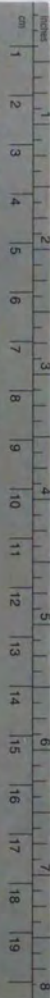
東京大学 大学院 理学系研究科

物理学専攻

松 永 浩 之

Kodak Color Control Patches

Blue Cyan Green Yellow Red Magenta White 3/Color Black



Kodak Gray Scale

A 1 2 3 4 5 6 M 8 9 10 11 12 13 14 15 B 17 18 19



© Kodak, 2007 TM, Kodak



A Measurement of  
Cosmic Ray Antiproton Flux

By  
Hiroyuki Matsunaga

Department of Physics,  
School of Science,  
University of Tokyo

1996

## Abstract

A measurement of antiprotons ( $\bar{p}$ 's) in the cosmic radiation was performed using the BESS balloon-borne magnetic spectrometer. After two successful flights were made in 1993 and 1994, the third flight was made in 1995 with the improved detector at a residual atmosphere below  $5 \text{ g/cm}^2$  and the geomagnetic cutoff rigidity below  $0.6 \text{ GV}$ . Clear identification of the antiprotons with negligible backgrounds is obtained by the precise measurements of rigidity, time of flight and energy losses. Using '95 flight data, forty three antiprotons were detected in the kinetic energy range  $175\text{--}1400 \text{ MeV}$ , giving the antiproton fluxes of  $(1.36^{+1.41+0.24}_{-0.79-0.23}) \times 10^{-2}$ ,  $(1.36^{+0.83+0.26}_{-0.57-0.20}) \times 10^{-2}$ ,  $(1.22^{+0.81+0.32}_{-0.55-0.20}) \times 10^{-2}$ ,  $(1.25^{+0.67+0.45}_{-0.50-0.26}) \times 10^{-2}$  and  $(1.85^{+0.79+0.59}_{-0.61-0.35}) \times 10^{-2} \text{ m}^{-2}\text{sr}^{-1}\text{sec}^{-1}\text{GeV}^{-1}$  in the kinetic energy range of  $175\text{--}300 \text{ MeV}$ ,  $300\text{--}500 \text{ MeV}$ ,  $500\text{--}700 \text{ MeV}$ ,  $700\text{--}1000 \text{ MeV}$  and  $1000\text{--}1400 \text{ MeV}$  respectively, after correcting for the selectional efficiencies and for the losses due to the interactions. These data provide the first measurement of the energy spectrum of the cosmic antiprotons at this low energy region, and allow us to search for the primary antiprotons from the hypothetical novel processes such as the evaporation of primordial black holes or the annihilation of supersymmetric dark matters. The observed energy spectrum is consistent to be flat, not in contradiction with possible existence of primary antiproton components, although the statistical accuracy is not yet good enough to exclude purely secondary origin.



## Contents

<b>1</b>	<b>Introduction</b>	<b>1</b>
<b>2</b>	<b>Experimental Apparatus</b>	<b>7</b>
2.1	Basic Features . . . . .	7
2.2	Superconducting Solenoidal Magnet . . . . .	8
2.3	JET chamber . . . . .	12
2.4	Inner and Outer Drift Chambers . . . . .	16
2.5	Time-of-Flight Hodoscope . . . . .	21
2.5.1	TOF Hodoscope in BESS '93 and '94 instrumentation . . . . .	21
2.5.2	TOF Hodoscope in BESS '95 instrumentation . . . . .	27
2.6	Čerenkov Counters . . . . .	28
2.7	Trigger . . . . .	31
2.7.1	T0 Trigger . . . . .	31
2.7.2	Track Trigger . . . . .	32
2.7.3	Master Trigger and Fast Clear . . . . .	37
2.8	Data Acquisition System . . . . .	37
2.8.1	Communication subsystem . . . . .	38
2.8.2	Monitor subsystem . . . . .	39
2.8.3	Event Process subsystem . . . . .	39
2.8.4	Data Storage subsystem . . . . .	42
<b>3</b>	<b>Flight</b>	<b>43</b>
<b>4</b>	<b>Data Analysis</b>	<b>55</b>
4.1	Flight Data Sample . . . . .	55
4.2	Event Reconstruction . . . . .	58
4.2.1	Track Reconstruction . . . . .	58
4.2.2	Time-of-Flight Measurement . . . . .	59
4.2.3	$dE/dx$ Measurement . . . . .	61
4.3	Simulation . . . . .	62
4.4	Event Selections . . . . .	65
4.4.1	Selections for Good Single Track . . . . .	65
4.4.2	Track Quality Cut . . . . .	66
4.4.3	TOF Quality Cut . . . . .	68
4.5	General Data Quality . . . . .	69



4.6	Selections of Proton and Antiproton Events	81
4.6.1	$dE/dx$ cut	84
4.6.2	Albedo Rejection	92
4.6.3	Mass cut	92
4.6.4	$\beta$ cut	92
4.7	Selected Events and Background Estimation	93
4.7.1	Supplementary confirmation by Čerenkov signals	93
4.7.2	Background estimation	110
<b>5</b>	<b>Flux determination</b>	<b>115</b>
5.1	Antiproton Events	115
5.2	Corrections	115
5.2.1	Ionization Energy Loss	115
5.2.2	Exposure Factor	121
5.2.3	Selection Efficiencies	121
5.2.4	Single Track Efficiency and the Trigger Efficiencies	124
5.2.5	Atmospheric Secondary Production	124
5.2.6	Losses in the Atmosphere	126
5.2.7	Interactions in the Atmosphere	126
5.2.8	Re-entrant Albedo Particle	129
5.2.9	Geomagnetic Cutoff	130
5.2.10	Summary of Corrections	131
5.3	Antiproton Flux	131
<b>6</b>	<b>Discussions</b>	<b>139</b>
<b>7</b>	<b>Conclusions</b>	<b>141</b>

## List of Tables

1.1	Summary of experimental results on $\bar{p}/p$ ratio	4
2.1	Main specifications of the BESS instrument	10
2.2	Main specifications of the superconducting solenoidal magnet	11
2.3	The conditions of the Track Trigger hit-pattern selection	35
3.1	Flight summary of BESS experiment	43
3.2	Summary of the dead time	50
3.3	The conditions of the T0 trigger and the trigger rates	51
3.4	The settings of the Master Trigger and the trigger rate ('93 and '94-1)	52
3.5	The settings of the Master Trigger and the trigger rate ('94-2 and '95)	53
4.1	Summary of BESS flight data ('93 and '94)	56
4.2	Summary of BESS flight data ('95)	57
4.3	Summary of the event selection cuts	78
4.4	Summary of the proton/antiproton selection	110
5.1	The principal properties of the antiproton events	116
5.2	Summary of the number of antiprotons and the correction values to derive the $\bar{p}$ flux (1)	132
5.3	Summary of the number of antiprotons and the correction values to derive the $\bar{p}$ flux (2)	133
5.4	The cumulated values and the $\bar{p}$ flux	134
5.5	Statistical errors of the $\bar{p}$ flux	135
5.6	Summary of systematic errors of $\bar{p}$ flux	137



## List of Figures

1.1	Previous data on the antiproton flux and predicted spectra with various solar modulations . . . . .	3
1.2	Current summary of $\bar{p}/p$ ratio from experiments and calculations . . .	5
2.1	Cross-sectional view of the BESS instrument ('93 and '94) . . . . .	8
2.2	(a) Cross-sectional view and (b) photograph of the BESS instrument ('95) . . . . .	9
2.3	Cross-sectional view of the superconducting solenoidal magnet . . . .	10
2.4	Schematic view of the JET chamber . . . . .	12
2.5	Circuit model of the charge division method used for determining the $z$ -coordinate . . . . .	14
2.6	Residual distribution of the JET chamber $r\phi$ hit points . . . . .	15
2.7	JET chamber $r\phi$ resolution as a function of (a) the drift distance, and (b) the angle $\phi$ across the cathode wire plane . . . . .	15
2.8	Residual plot of the JET chamber along the $z$ -coordinate for (a) single-charged and (b) multiple-charged particles . . . . .	16
2.9	Diagram showing a cross-sectional view of IDC and ODC . . . . .	17
2.10	Diagram showing a cross-sectional view of the IDC and ODC in $r\phi$ plane . . . . .	18
2.11	(a) Equipotential and (b) electric field strength contours of the IDC .	18
2.12	Read-out scheme for IDC and ODC signals . . . . .	19
2.13	Residual distribution of the IDC $r\phi$ hit points . . . . .	20
2.14	IDC $r\phi$ resolution as a function of (a) drift distance, and (b) angle $\phi$ with respect to the axial direction . . . . .	20
2.15	Corresponding sets of vernier pads . . . . .	21
2.16	Scatter plot of the $\epsilon$ parameter of the inner and outer pad . . . . .	22
2.17	Spatial resolution of the $z$ -coordinate measurement in the IDC . . . .	22
2.18	Time-of-flight counter of BESS '93 and '94 instrument . . . . .	23
2.19	Read-out scheme for PMT signals . . . . .	24
2.20	(a) $z$ -position dependence of the measured PMT charge and (b) charge distribution at the center of the counter ( $z = 0$ ) ('93) . . . . .	26
2.21	Timing resolution as a function of (a) the $z$ -position and (b) square root of $N_{pe}$ at the center ('93) . . . . .	26
2.22	$\Delta TOF$ for proton events with the rigidities above 5 GV ('93) . . . .	27
2.23	Time-of-flight counter of BESS '95 instrument . . . . .	27



2.24	(a) $z$ -position dependence of the measured PMT charge and (b) charge distribution at the center of the counter ( $z = 0$ ) ('95)	29
2.25	$\Delta$ TOF for proton events with the rigidities above 5 GV ('95)	29
2.26	Čerenkov counter of BESS '95 instrument	30
2.27	Basic scheme of the Track Trigger	33
2.28	Block diagram of TT process	33
2.29	Simulated Track Trigger efficiency	36
2.30	Schematic diagram of the data acquisition system	38
2.31	The block diagram of the Data Process and the Data Storage subsystem	40
3.1	The data of neutron monitors	44
3.2	Flight trajectories for BESS '93, '94 and '95	45
3.3	The contour map for geomagnetic cutoff rigidity	45
3.4	House-keeping data on altitude, temperatures and pressures in BESS '93 flight	46
3.5	House-keeping data on altitude, temperatures and pressures in BESS '94 flight	47
3.6	House-keeping data on altitude, temperatures and pressures in BESS '95 flight	48
3.7	Acceleration loads in '93, '94 and '95 flights	49
4.1	Method of the rigidity measurement	58
4.2	Method of the TOF measurement	60
4.3	Simulated BESS detector	63
4.4	Inelastic and Elastic cross sections for antiproton to carbon and aluminum	64
4.5	Track Quality Cut 1,2,3.	70
4.6	Track Quality Cut 4,5,6,7.	71
4.7	Track Quality Cut 8.	72
4.8	Track Quality Cut 9.	73
4.9	Number of hits in each IDC	74
4.10	TOF Quality Cut 1,2.	75
4.11	TOF Quality Cut 3.	76
4.12	TOF Quality Cut 4.	77
4.13	The estimated error of $1/R_t$ in $r\phi$ -fitting	79
4.14	$\Delta(1/R_t)$ as a function of the absolute rigidity	79
4.15	$\beta^{-1}$ vs Rigidity	80
4.16	Velocity resolution as a function of $\beta^{-1}$	80
4.17	$dE/dx$ (Scintillator) distribution	82
4.18	$dE/dx$ (JET chamber) vs Rigidity	83
4.19	$(m/z)^2$ distribution	84
4.20	$(m/z)^2$ distribution at various rigidities	85
4.21	(a) Scatter plot of $(\beta\gamma)^{-1}$ vs deflection and (b) its profile histogram	86
4.22	Proton selection by $dE/dx$ in the scintillators	87
4.23	Proton selection by $dE/dx$ in JET chamber	88

4.24	$dE/dx$ distribution relative to the proton peak	89
4.25	$\beta^{-1}$ vs Rigidity for all event samples before $dE/dx$ cut	90
4.26	$\beta^{-1}$ vs Rigidity for all event samples after $dE/dx$ cut	91
4.27	$\beta^{-1}$ distribution of events with rigidities $-4 \text{ GV} < R < 0 \text{ GV}$ after $dE/dx$ cut	93
4.28	The identification of antiproton events (1)	94
4.29	The identification of antiproton events (2)	95
4.30	Close-up view of $\beta^{-1}$ vs rigidity for negative-charged particles	96
4.31	Close-up view of $\beta^{-1}$ vs deflection for negative-charged particles	97
4.32	Mass of the proton/antiproton events	98
4.33	Distribution of $dE/dx$ vs Rigidity of the antiproton events	99
4.34	Distribution of $dE/dx$ vs Rigidity of the antiproton events	100
4.35	$dE/dx$ distribution relative to the proton peak	101
4.36	The properties of the proton/antiproton events (1)	102
4.37	The properties of the proton/antiproton events (2)	103
4.38	The properties of the proton/antiproton events (3)	104
4.39	The properties of the proton/antiproton events (4)	105
4.40	The properties of the proton/antiproton events (5)	106
4.41	The properties of the proton/antiproton events (6)	107
4.42	The properties of the proton/antiproton events (7)	108
4.43	The properties of the proton/antiproton events (8)	109
4.44	Distribution of Čerenkov signal size vs Rigidity	111
4.45	$\beta^{-1}$ distribution of negative-charged particles	113
4.46	$\beta^{-1}$ distribution of light negative particles	114
5.1	Event display of an antiproton candidate (1)	117
5.2	Event display of an antiproton candidate (2)	118
5.3	Event display of an antiproton candidate (3)	119
5.4	Event display of an antiproton candidate (4)	120
5.5	Estimation of the fluctuations of the energy losses using Monte Carlo simulation	122
5.6	The geometrical acceptance ( $S\Omega$ ) as function of the energy.	123
5.7	Off-line Selection efficiencies for protons and antiprotons	125
5.8	The single track efficiency as function of the energy	126
5.9	Track Trigger hit-pattern selection efficiency	127
5.10	Track Trigger deflection selection efficiency	127
5.11	Secondary antiproton flux	128
5.12	Survival probability of protons/antiprotons for $5 \text{ g/cm}^2$ of the atmosphere	128
5.13	Deformation of the antiprotons spectrum due to $5 \text{ g/cm}^2$ of the atmosphere	129
5.14	Ratio of the observed number of proton per unit time in the last run to one in the first four runs	130
5.15	Measured $\bar{p}$ flux	138

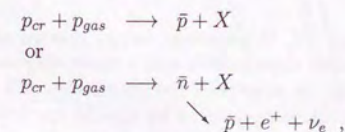


## Chapter 1

### Introduction

The energy spectrum of cosmic ray antiprotons ( $\bar{p}$ 's) is of great importance providing information on the cosmic ray propagation models. The energy spectrum especially at the low energy could also be a unique window to search for the hypothetical novel processes such as the evaporation of primordial black holes or the annihilation of supersymmetric dark matters (neutralinos).

It is expected that a large portion of cosmic ray antiprotons originates from the collisions of cosmic ray protons (and nuclei) with the interstellar medium. Since the interstellar medium consists mainly of hydrogen gas, these secondary antiprotons are produced through the following reactions:



where  $X$  represents other particles which emerge with the antiproton from the interaction. The energy spectrum of the secondary antiprotons to be observed depends on that of protons, on the characteristics of the interactions in  $pp$ -collisions, and on the subsequent propagation in the Galaxy. The kinematic conditions on the interactions require the lowest threshold energy on the cosmic ray protons of  $E_{p_{cr}}^{th} \sim 6$  GeV. The particles produced at this threshold are  $ppp\bar{p}$  at rest in the center of mass system, having a kinetic energy of about 1 GeV in the laboratory system. The energy of the antiproton could be lower than 1 GeV when the cosmic ray proton has a higher energy and the antiproton is produced in the backward direction to the incoming cosmic ray proton in the center of mass system, but this probability is reduced by the small phase space factor. As the result, the spectrum of the antiprotons is expected to have a peak around 2 GeV and decline steeply at energies below 1 GeV, with the shape which does not depend on propagation models very much.

On the other hand, no such suppression of low energy antiprotons is expected for primary sources such as the evaporation of the primordial black holes, or the annihilation of the supersymmetric (neutralino) dark matters. Actually the antiprotons from these primary sources are expected to exhibit very soft energy spectra. The low



energy antiprotons could thus be a unique window to search for the novel primary processes.

Figure 1.1 shows the predicted antiproton energy spectra for the cosmic ray secondaries, for the annihilation of neutralino dark matters and for the evaporation of primordial black holes.

The “standard leaky box (SLB) model” is the most popular model of the cosmic ray propagation, in which the cosmic rays escape from the galactic disk after having traversed about  $10 \text{ g/cm}^2$  of interstellar medium. Antiprotons will be produced in the collisions of the cosmic ray protons and heliums with the interstellar medium, and will propagate in the Galaxy. The flux of this secondary antiprotons can be calculated using the escape length determined by fitting the observed ratios of secondary to primary nuclei, such as B/C [2, 3, 4, 5].

The “diffusive reacceleration (DR) model” [6] proposed recently, takes into account a link between diffusion and reacceleration during propagation. It interprets the propagation of cosmic rays as a diffusive process, and requires no further effective mechanisms for the escape of particles below  $\sim 1 \text{ GeV/nucleon}$  from the Galaxy which is needed in the standard leaky box model in order to explain the observations on cosmic ray nuclei.

The spectra of the antiprotons predicted by these two models have their peaks around  $2 \text{ GeV}$  of kinetic energy, showing a steep decline at lower energies due to the kinematical suppression, as well as at higher energies due to the decline of the cosmic ray fluxes.

In a recent systematic study [1], the absolute energy spectra of the secondary antiprotons has been calculated for these models with a reasonably small uncertainty. It is also realized that these energy spectra of the antiprotons will not be affected very much by the solar modulations because of its specific spectral shape. Hence the measurement of the antiproton flux at the top of the atmosphere will provide informations to examine the model.

A possible novel source of primary antiprotons is the evaporation of mini black holes. The “primordial black holes” (PBHs), which might have formed in the early universe [7, 8, 9], are the only black holes small enough for the quantum emissions to be significant. The rate of the quantum emission from a black hole with a mass of  $M$  is just the same as the rate of a thermal radiation from a body with temperature of  $T \propto M^{-1}$  [10, 11]. PBHs would thus radiate rapidly, lose their mass, and will reach higher and higher temperatures. Finally the temperature would get extremely high and PBHs would explosively radiate various particles, including antiprotons [12, 13, 14]. The flux of these antiprotons would rise toward the lower energy, and could clearly be distinguished from the secondary antiproton flux. In a recent detailed study [15], the energy spectrum of these antiprotons is calculated with a reasonably small uncertainty, and it has become possible to place a limit on the local explosion rate.

The annihilation of the supersymmetric (neutralino) dark matters could also be

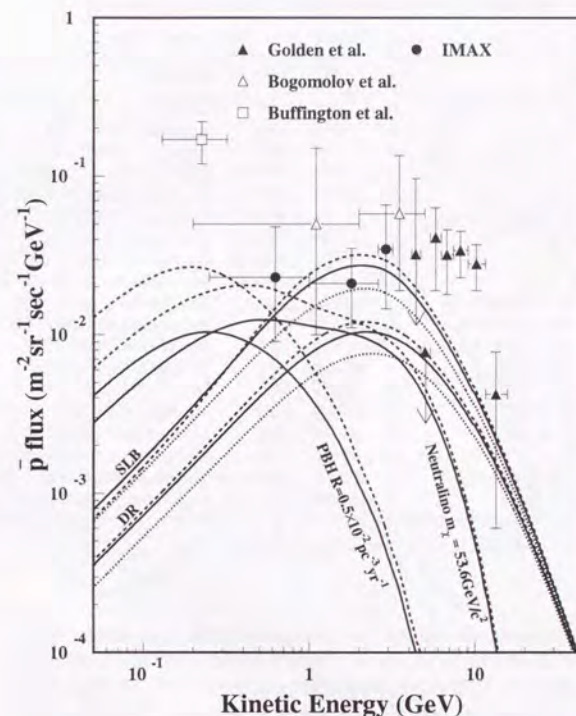


Figure 1.1: Previous data on the antiproton flux and predicted spectra with various solar modulations. The experimental data points are from Golden *et al.* [23, 24] (filled triangles), Bogomolov *et al.* [26, 27, 24] (open triangles), Buffington *et al.* [25] (open square), and IMAX experiment [32] (filled circles). The solid, dashed and dotted curves labeled “SLB” and “DR” are the calculations by Mitsui [1] based on standard leaky box model [5] and on diffusive reacceleration model [6], respectively. The spectra for neutralino annihilation (the curves labeled “Neutralino”) are from Mitsui *et al.* [16]. The spectra for primordial black holes (the curves labeled “PBH”) are the calculations by Maki *et al.* [15] for a specific evaporation rate. The dashed curves are modulated to solar minimum (the mean energy loss  $\phi = 350 \text{ MeV}$ ), the dotted are modulated to solar maximum ( $\phi = 1000 \text{ MeV}$ ) and the solid are modulated to 1995 levels ( $\phi = 550 \text{ MeV}$ ).



Table 1.1: Summary of experimental results on  $\bar{p}/p$  ratio.

Energy (GeV)	$\bar{p}/p$ ratio	$N_{\bar{p}}$	$N_p$	Year	Reference
—	$< 1 \times 10^{-3}$	0	1000	1957	Aizu <i>et al.</i> (1961) <sup>†</sup> [18]
0.10 – 0.15	$> 3 \times 10^{-4}$	0	3500	1962	Apparao (1967) <sup>†</sup> [19]
0.05 – 0.15	$< 4.3 \times 10^{-4}$ (1 $\sigma$ )	0	—	1972	Apparao (1985) <sup>†</sup> [20]
2 – 5	$(6 \pm 4) \times 10^{-4}$	2	3400	1972–77	Bogomolov <i>et al.</i> (1979) <sup>††</sup> [21]
4.7 – 11.6	$(5.2 \pm 1.5) \times 10^{-4}$	34.9	54600	1979	Golden <i>et al.</i> (1979) <sup>††</sup> [22, 23]
0.13 – 0.37	$(2.2 \pm 0.6) \times 10^{-4}$	14	—	1980	Buffington <i>et al.</i> (1981) <sup>†</sup> [25]
0.2 – 2	$(6^{+14}_{-5}) \times 10^{-5}$	1	17800	1984–85	Bogomolov <i>et al.</i> (1987) <sup>††</sup> [26]
2 – 5	$(3^{+4}_{-2}) \times 10^{-4}$	2+0	$\frac{3400}{+2200}$	1972–86	Bogomolov <i>et al.</i> (1987) <sup>††</sup> [26]
2 – 5	$(2.4^{+2.4}_{-1.3}) \times 10^{-4}$	3	12400	1986–88	Bogomolov <i>et al.</i> (1990) <sup>††</sup> [27]
0.1 – 0.64	$< 2.8 \times 10^{-5}$ (85% C.L.)	0	87213	1987	Salamon <i>et al.</i> (1990) <sup>‡</sup> [28]
0.64 – 1.58	$< 6.1 \times 10^{-5}$ (85% C.L.)	0	38590	1987	Salamon <i>et al.</i> (1990) <sup>‡</sup> [28]
0.6 – 0.8	$< 2.3 \times 10^{-4}$ (90% C.L.)	3	41514	1987	Moats <i>et al.</i> (1990) <sup>††</sup> [29]
0.12 – 0.60	$< 8.4 \times 10^{-6}$ (2 $\sigma$ )	1	322281	1987	Stochaj (1990) <sup>‡</sup> [30]
3.70 – 19.08	$(1.24^{+0.68}_{-0.51}) \times 10^{-4}$	11	69311	1991	Hof <i>et al.</i> (1996) <sup>††</sup> [31]
0.25 – 1.0	$(3.14^{+3.4}_{-1.9}) \times 10^{-5}$	3	127000	1992	Mitchell <i>et al.</i> (1996) <sup>‡</sup> [32]
1.0 – 2.6	$(5.36^{+3.5}_{-2.4}) \times 10^{-5}$	8	141000	1992	Mitchell <i>et al.</i> (1996) <sup>‡</sup> [32]
2.6 – 3.2	$(1.94^{+1.8}_{-1.1}) \times 10^{-4}$	5	23100	1992	Mitchell <i>et al.</i> (1996) <sup>‡</sup> [32]
0.175 – 0.300	$< 2.9 \times 10^{-5}$ (90% C.L.)	0	405860	1993	Yoshimura <i>et al.</i> (1995) <sup>‡</sup> [33]
0.300 – 0.500	$(1.2^{+1.0}_{-0.65}) \times 10^{-5}$	4	772940	1993	Yoshimura <i>et al.</i> (1995) <sup>‡</sup> [33]

<sup>†</sup>annihilation identification    <sup>††</sup>Čerenkov veto    <sup>‡</sup>mass measurement

a source of the primary antiprotons. Neutralino is supposed to be the lightest supersymmetric particle, and therefore to be stable. Such a weakly interacting massive particle (WIMP) is a popular dark matter candidate in the view of the primordial nucleosynthesis and the formation and the clustering of galaxies. Supposing the galactic halo contains the neutralinos, their annihilation in their collisions would produce cosmic primary antiprotons in some fraction. It was pointed out that this antiproton flux might possibly reach a detectable level [17]. A more recent calculation showed that the flux of these antiprotons might exceed that of secondary antiprotons at energies below 1 GeV [16].

It is noted, however, that the flux of these antiprotons would be affected by solar activity, shown in Figure 1.1, and it has the highest value at solar minimum.

There have been many balloon experiments searching for cosmic ray antiprotons, as summarized in Table 1.1 and in Figure 1.2. The methods used in the searches are categorized in three. The first method is to identify the antiprotons stopped in the instrument by their specific annihilation radiation in the materials. For this annihilation identification, the backgrounds of the nuclear interaction could be a problem. The second method uses Čerenkov counters as a veto of backgrounds, after separating negative particles from positive ones by measuring their deflection in the magnetic field. This way of identification is vulnerable to various backgrounds as well as to the errors in determining the efficiencies of the Čerenkov counters. The

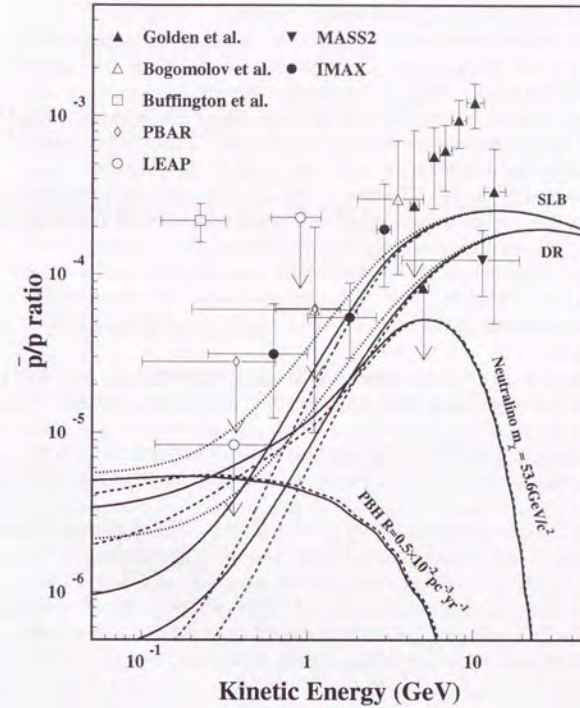


Figure 1.2: Current summary of  $\bar{p}/p$  ratio from experiments and calculations. The data points are Golden *et al.*[23] (filled triangles), Bogomolov *et al.*[26, 27] (open triangles), Buffington *et al.*[25] (open square), PBAR experiment [28] (open diamonds), LEAP experiment [29, 30] (open circles), MASS2 experiment [31] (filled reverse-triangles), and IMAX experiment [32] (filled circles). The solid, dashed and dotted curves labeled “SLB” and “DR” are the calculations by Mitsui [1] based on the standard leaky box model (SLB) [5] and on the diffusive reacceleration model (DR) [6]. The spectra from neutralino annihilation (“Neutralino”) are the calculations by Mitsui *et al.*[16]. The spectra from the evaporation of primordial black holes (“PBH”) are the calculations by Maki *et al.*[16]. The dashed curves are modulated to solar minimum (the mean energy loss  $\phi = 350$  MeV), the dotted are modulated to solar maximum ( $\phi = 1000$  MeV) and the solid are modulated to 1995 levels ( $\phi = 550$  MeV).



most positive identification can be made by determining the mass of the particles, based on the measurement of their magnetic rigidity, velocity, and  $dE/dx$ .

The earliest experiments were performed based on the annihilation identification using emulsion stacks [18, 19, 20], however, the solid angle of the stacks were small and failed to observe a signal. The first reports of the observations of cosmic ray antiprotons [21, 22] and the proceedings [26, 27, 29] were based on the searches at higher energies, where higher antiproton fluxes are expected. These experiments, however, lacked the definitive identification since the mass of the particles cannot be determined in those energy region. Therefore these observations had to rely on the Čerenkov veto. At low energies, one experiment reported a positive detection of antiprotons utilizing the annihilation-identification method [25]. However, more recent and more reliable experiments which employ the mass-measurement method failed to see the signal at a level an order of magnitude below the reported flux [28, 30]. Therefore it is probably fair to say that there existed no definite detection of the cosmic antiprotons.

Very recently, using a magnetic spectrometer with a larger acceptance, we have performed the first definite detection of eight antiprotons by measuring their masses. [33, 34].

In this thesis, we report on the first measurement of the cosmic ray antiproton flux at the low energy region up to 1.4 GeV, based on 43 antiproton events detected in 1995 flight.

Chapter 2 gives a brief description of the BESS instruments. Flight information is described in Chapter 3. Chapter 4 describes the data analysis procedure to select antiprotons and protons using both the experimental data and the Monte Carlo simulation data. In chapter 5, some corrections and results of the antiproton flux measurement is described. In chapter 6, comparisons with previous measurements and with theoretical predictions are discussed. Finally, a summary of this thesis is presented in chapter 7.

## Chapter 2

# Experimental Apparatus

### 2.1 Basic Features

The Balloon-borne Experiment with a Superconducting solenoidal magnet Spectrometer (BESS) was proposed [35] to investigate cosmic rays, especially antiprotons and antiheliums. The BESS detector is designed as an omnipurpose detector with a very large solid angle and a high tracking capability, and it is suitable for distinct detection of rare cosmic antimatter existing among an abundance of protons and heliums, as well as precise measurement of absolute cosmic ray fluxes. The detector is constructed using technologies from the modern collider experiments such as the thin superconducting solenoid, the precision drift chambers with cylindrical configuration, the precision time of flight system, and the high speed data acquisition system [36, 37, 38, 39, 40, 41, 42]. The present BESS collaboration is composed of University of Tokyo, National Laboratory for High Energy Physics (KEK), Institute for Space and Astronautical Science (ISAS), Kobe University, Goddard Space Flight Center of National Aeronautics and Space Administration (NASA/GSFC), New Mexico State University (NMSU) and University of Maryland.

Figure 2.1 shows a cross-sectional view of the BESS instrument in '93 and '94 flight, being comprised of a jet-type drift (JET) chamber, inner drift chambers (IDCs), superconducting solenoid, outer drift chambers (ODCs), and a Time-of-Flight (TOF) hodoscope. In '94 flight, Čerenkov counters were added outside of the pressure vessel as an additional particle identifier.

Figure 2.2 shows a cross-sectional view and a photograph of the BESS instrument in '95 flight, where a new pressure vessel with larger capacity was provided. Then Čerenkov counters were installed inside the vessel. The remarkable improvement in BESS '95 instrumentation was the installation of new TOF system, in which the width of each paddle became half the size of old one and the shape of the light guide is selected carefully. As a result, about three times as good resolution was obtained for the timing measurement.

These components are arranged radially from the center of the device, and along with the front-end electronics and microcomputers, are enclosed by a 2 mm (2.5 mm for '95 instrumentation) thick aluminum pressure vessel that keeps the inside pressure as the sea level during flights. Situated outside the vessel are an 8 mm tape



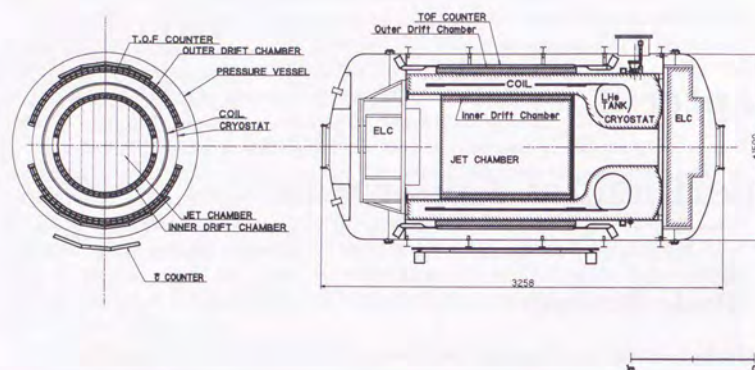


Figure 2.1: Cross-sectional view of the BESS instrument ('93 and '94). Čerenkov counters were added in '94 flight.

storage device shielded by iron containers, a power supply system, and a consolidated instrument package (CIP) communication unit which handles communications between the payload and ground station. For the BESS '93 and '94 instrumentation the entire unit weighs 2.1 t. The dimension is 1.5 m in diameter and 3.3 m in length. For the BESS '95 instrumentation, the entire unit was extended to 1.7 m in diameter and 3.8 m in length provided with the new pressure vessel with the thickness of 2.5 mm. Then the weight increased to 2.2 t. When suspended from a 29.7 Mft<sup>3</sup> balloon, they were compact and light enough to travel at an altitude of about 35 km.

A thin entrance wall of about 9.0 g/cm<sup>2</sup> enables low energy particles to pass through the detectors, while a cylindrical configuration provides large tracking volume and a geometrical acceptance of 0.4 m<sup>2</sup> · sr for '93 and '94 instrumentation. This became 0.32 m<sup>2</sup> · sr for '95 instrumentation due to the dimension of new TOF counter. The JET chamber is capable of precisely detecting particles and measuring their magnetic rigidities (Rigidity means momentum per charge). Since the tracking devices are equipped with 32 measurement positions, even a complicated event having interactions inside the detector can easily be monitored. Time-of-Flight hodoscope is utilized to determine the velocity and the charge of the particle, measuring the time of flight and the energy loss in the scintillator. Table 2.1 summarizes the main specifications of BESS instrument and difference among the three flights.

## 2.2 Superconducting Solenoidal Magnet

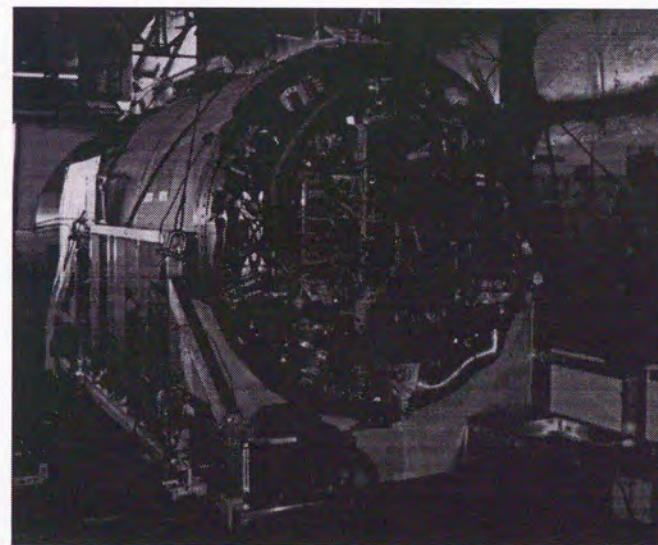
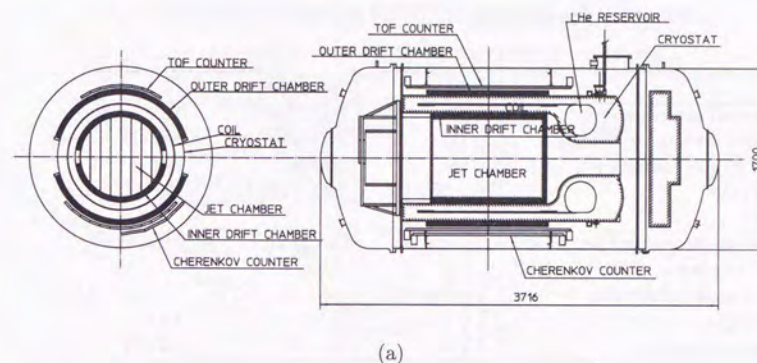


Figure 2.2: (a) Cross-sectional view and (b) photograph of the BESS instrument ('95).



Table 2.1: Main specifications of the BESS instrument.

	'93 flight	'94 flight	'95 flight
Geometrical acceptance	0.4 m <sup>2</sup> sr	0.4 m <sup>2</sup> sr	0.32 m <sup>2</sup> sr
Maximum detectable rigidity	200 GV	200 GV	200 GV
Time-of-Flight resolution	300 ps	300 ps	110 ps
Trigger rate	100 – 200 Hz	100 – 200 Hz	100 – 200 Hz
Material			
in the spectrometer (per wall)	9.0 g/cm <sup>2</sup>	9.0 g/cm <sup>2</sup>	9.0 g/cm <sup>2</sup>
for $\tilde{C}$ at bottom		2.3 g/cm <sup>2</sup>	2.5 g/cm <sup>2</sup>
Pressure vessel dimension	1.5 m $\phi$ $\times$ 3.2 m	1.5 m $\phi$ $\times$ 3.2 m	1.7 m $\phi$ $\times$ 3.8 m
Total weight	2.1 t	2.1 t	2.2 t
Power consumption	1.2 kW	1.2 kW	1.2 kW

Figure 2.3 shows cross-sectional views of the superconducting solenoidal magnet (MAG), which has a 0.85 m  $\phi$   $\times$  1.0 m warm bore that encloses the JET and inner drift chambers. A magnetic field of 1 T (maximum 1.2 T) is generated inside the bore at a nominal current of 430(520) A, with the resultant field uniformity being  $\pm 15\%$ . A solenoid coil (1 m  $\phi$   $\times$  1 m( $\ell$ )  $\times$  5.4 mm( $t$ )) made of aluminum-stabilized superconductor NbTi(Cu) is installed inside the double thermal shielded cryostat, and is indirectly cooled through the aluminum cylinder by a toroidal-shaped liquid

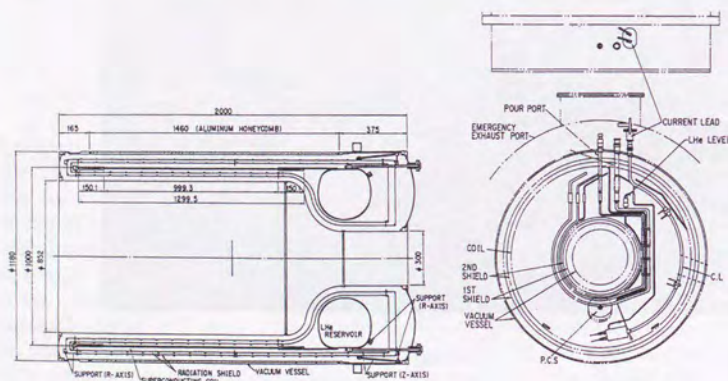


Figure 2.3: Cross-sectional view of the superconducting solenoidal magnet.

Table 2.2: Main specifications of the superconducting solenoidal magnet.

Coil		
material	conductor	NbTi/Cu
	stabilizer	Pure Al (99.999%)
diameter		1.0 m
length		1.3 m
thickness	(center)	5.2 mm
	(end notch)	10.4 mm
Support cylinder		
material		A2219
thickness	(center)	2 mm
	(end notch)	4 mm
Cryostat		
diameter		1.18 m
length		2.0 m
LHe capacity		150 $\ell$
Warm bore		
aperture		0.85 m
length		1.0 m
Central field		(maximum) 1.2 T
	(operational)	1.0 T
Current		(maximum) 520 A
	(operational)	430 A
Stored energy		(maximum) 815 kJ
	(operational)	557 kJ
Wall thickness		4 g/cm <sup>2</sup> per wall
		0.21 $X_0$ per wall
Total weight		430 kg

helium reservoir tank with 150  $\ell$  capacity (static indirect cooling method) [43, 44]. This method has an advantage over the bath cooling method in that it allows using a thinner cryostat wall. The MAG's thickness including the cryostat is 0.21 radiation length per wall and its total weight with helium is 430 kg. The amount of stored energy at 1(1.2) T is 557(815) kJ. Pure aluminum strips [43] are attached to the inner surface of the solenoid for quenching, *i.e.*, they rapidly conduct thermal energy in the axial direction and homogenize the thermal distribution Table 2.2 summarizes the main specifications of the MAG.

The magnet is equipped with a persistent current switch (PCS) fabricated from a superconductor and heater. It is heated up to break the superconduction during



magnet excitation, then cooled and automatically shortcut after being charged. The current from the magnet is subsequently able to pass through the PCS. Since the decay constant of this current is more than 900 years, if helium is filled to its maximum level, the current persists for as long as 6 days with no energy supply to the magnet. The magnet can be safely discharged by switching off the PCS and shunting the magnet current into a resistor located external to the vessel. Further details of the performance of the magnet will be found in Makida *et al.*[45].

## 2.3 JET chamber

The JET chamber, shown in Fig. 2.4, is a cylindrical jet-type [46] drift chamber situated inside the magnet, having a large tracking volume of  $0.754 \text{ m} \phi \times 1 \text{ m}$ . Cathode planes partition the chamber into four sections, with each plane consisting of 100 aluminum wires with a  $200 \mu\text{m}$  diameter. The wires are laid out, though actually they are stretched, at  $6.7 \text{ mm}$  intervals, and a high voltage of  $-10.8 \text{ kV}$  is applied to produce a constant electric field which drifts ionized electrons to the sense wires. At the center of each section, the sense and potential wires are alternately laid out at  $13.4 \text{ mm}$  intervals. The sense and potential (cathode) wires are respectively  $20 \mu\text{m} \phi$  gold-plated tungsten-rhenium wires and  $200 \mu\text{m} \phi$  gold-plated aluminum wires, and are stretched with a tension of 40 and 350 gw. The sense wires are staggered by  $\pm 0.5 \text{ mm}$  to resolve left-right ambiguity. The outer two sections have 32 sense wires and 33 potential wires, while the inner two correspondingly have 52

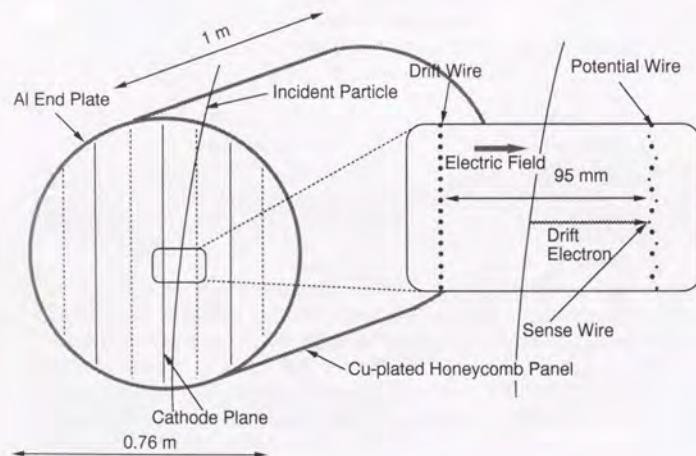


Figure 2.4: Schematic view of the JET chamber.

and 53 potential wires. The maximum drift distance of ionized electrons is  $95 \text{ mm}$ .

The cylindrical side walls are made of aramid core honeycomb to minimize material thickness and weight. The inner surface of the honeycomb panel is made of a copper-plated KAPTON sheet, on which the field-shaping patterns are etched. The two end-plates are  $25 \text{ mm}$  thick aluminum discs. The chamber's total weight is  $60 \text{ kg}$ .

The chamber is filled with a mixture of 90 %  $\text{CO}_2$  and 10 % Ar, being suitable for this experiment due to the following reasons:

1. The drift velocity of this gas mixture is slow enough to achieve good position resolution using a relatively slow electronics package designed for low power consumption.
2. Due to a small diffusion coefficient, timing fluctuations caused by the longitudinal diffusion of the electron cloud are small even after a long drift of  $95 \text{ mm}$ .
3. The gas mixture is non-flammable and easy to handle.

This mixture was used for the other drift chambers for the same reasons, in fact, the entire vessel is filled with it so that any chamber suffering a small gas leak will remain operational.

The signals from the sense wires are picked up by 352 preamplifier channels mounted on the end-plates, then amplified and converted into voltage signals that are directly fed into  $28.5 \text{ MHz}$  flash-type analog-to-digital converter (FADC) modules. A FADC module has sixteen channels in it and sixteen modules can be installed at the maximum for JET and IDC readout. Eight modules for '93 instrument and nine modules for '94 and '95 instruments were installed for JET readout. Each channel amplifies the signals and digitizes them into 8 bit digits every  $35 \text{ ns}$ . The output data of each FADC channel contains information on the charge and timing, in other words, four-hundred sets of the charge and timing data for  $14 \mu\text{s}$  of the full drift time. Since a typical single pulse has a pulse width of about  $400 \text{ ns}$ , multiple hits in a single wire can be well separated and recognized. However, the total amount of FADC data is too large to record all, and consequently, on-line zero-suppression circuits are employed to reduce the data amount, where digitized data is discriminated by a digital comparator and only data above a threshold value is accumulated into first-in-first-out (FIFO) memory. Furthermore, a data compressor circuit sequentially reads all FIFO memories of the FADC channels and compresses them into formatted data-packet, where the timing, total integrated charge, width, rising shape, and readout channel number of a pulse signal were packed into a 8 byte formatted data, however the entire pulse shapes were lost. This data compression scheme reduced the data size of an event by a factor of 3 and it takes  $200 \mu\text{s}$  for the compressor to scan all channels and complete the process for an event of the typical data size.

The position of the hits are three-dimensionally measured by the timing and charge of the signals. In this dissertation, cylindrical coordinates ( $r\phi z$ ) are used,



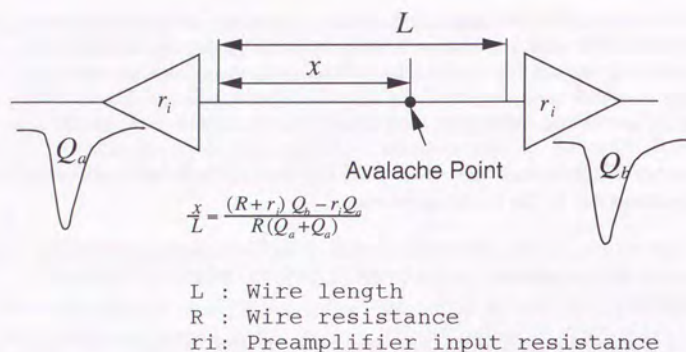


Figure 2.5: Circuit model of the charge division method used for determining the  $z$ -coordinate.

with the magnet field direction being defined as the  $z$ -axis and the perpendicular plane as the  $r\phi$  plane. The hit position in the  $r\phi$  plane is calculated by its drift time. Although drift length  $x$  and drift time  $t$  are nearly proportional, some nonlinear effects nevertheless exist due to distortion of the electric field and inclination of the track in the cell. Such nonlinearity, however, is corrected by fitting the deviation of the hit position to a third-ordered polynomial. The hit position along the  $z$ -coordinate is obtained by applying the charge division method [46], where Fig. 2.5 shows the employed circuit model. To minimize errors, the internal resistor and gain of the preamplifier are calibrated and adjusted using the actual flight data.

The FADCs read signals from 80 sense wires, some of which are read from both ends to determine the  $z$ -coordinate via charge division method. 32 wires were read from both sides in '93 flight. This number increased to 48 wires in '94 and 95 flights by installing one additional FADC module. As the tracks pass through the central region, where the signals can be read through the two longer columns of wires, a maximum of 24 positions can be measured in the  $r\phi$  plain. As for  $z$  direction, 16 and 24 positions can be measured in '93 and '94-'95 flights, respectively. Based on the residuals obtained from the fitted track (Fig. 2.6), the overall resolution of  $r\phi$  plane is estimated to be  $200 \mu\text{m}$ . These resolutions are dependent on the drift length due to the diffusion of electrons. Figure 2.7 shows the resolution as a function of (a) the drift distance and (b) the angle of the track trajectory across the cathode wire plane, where both resolutions are gradually degraded according to the drift distance and angle.

The resolution of the  $z$ -coordinate measurement is 2.5 cm for single-charged particles (Fig. 2.8 (a)), being worse than the expected value of 1 cm, since all the charge information below the threshold value is lost using the zero-suppress and compress scheme, and cannot be precisely corrected. On the other hand, 1.5

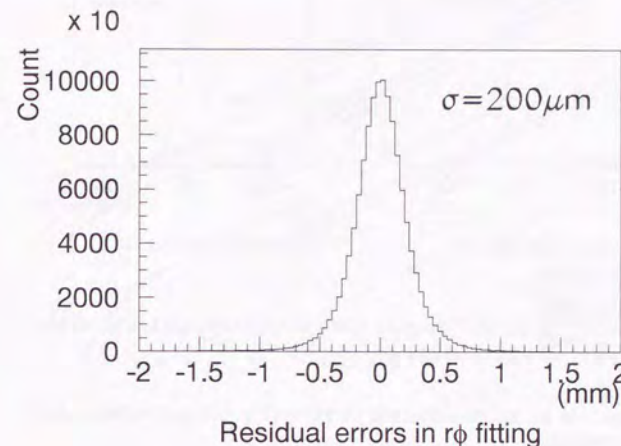


Figure 2.6: Residual distribution of the JET chamber  $r\phi$  hit points.

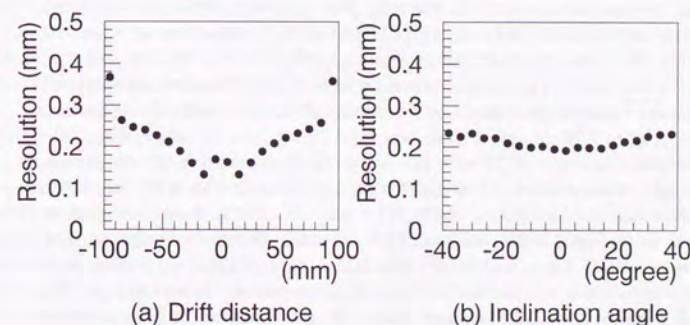


Figure 2.7: JET chamber  $r\phi$  resolution as a function of (a) the drift distance, and (b) the angle  $\phi$  across the cathode wire plane.



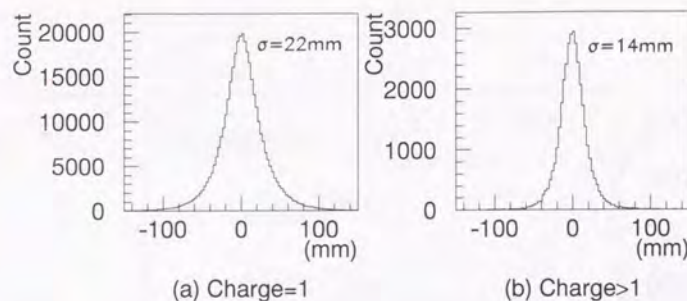


Figure 2.8: Residual plot of the JET chamber along the  $z$ -coordinate for (a) single-charged and (b) multiple-charged particles.

cm resolution is obtained for multiple-charged particles (Fig. 2.8 (b)) because they reduce the threshold effect.

## 2.4 Inner and Outer Drift Chambers

The inner drift chamber (IDC) and the outer drift chamber (ODC) are cell-type arc-shaped drift chambers located inside and outside the magnet, respectively (Fig. 2.9). The IDC (ODC) is a 1.06 m long (1.18 m) and 36 mm thick (44 mm) chamber located between the radii of 384 mm (594 mm) and 420 mm (638 mm) covering a polar angle from 8 (18) to 172 (162) degrees. Both chambers are identical except for their dimensions and magnetic field strength, *i.e.*, 1 T for the IDC and about 0.1 T for the ODC. The mechanical structure of each chamber is composed of four aramid core honeycomb panels with end and side plates made of engineering plastic (G10). Figure 2.10 depicts a cross-sectional view of the  $r\phi$  plane, where the surface of the panel is made of 18 and 125  $\mu\text{m}$ -thick copper and KAPTON sheets, respectively. The outer surface of the copper sheet is covered with a 0.5 mm thick Al sheet to increase mechanical strength. The inner KAPTON sheet is etched at 3 mm interval to form a 1.5 mm wide and 18  $\mu\text{m}$  thick electric field shaper, and corresponding pairs of 7.5 mm wide and 18  $\mu\text{m}$  thick diamond-shaped vernier pads surround the sense wires to detect the  $z$ -coordinate position. The inside of the chamber is divided into two 12 mm thick layers. At the center of each layer, sense wires and field wires are alternately laid out in about 50 mm spacing intervals. This wire configuration also acts to calibrate the drift velocity which is obtained by adjusting the sum of the drift length of both layers to the wire spacing, *i.e.*, 50 mm.

The sense and field wires are respectively gold-plated 25  $\mu\text{m}\phi$  tungsten-rhenium and 250  $\mu\text{m}\phi$  aluminum wires, respectively. They are stretched with a tension of 55 gw and 400 gw, respectively.

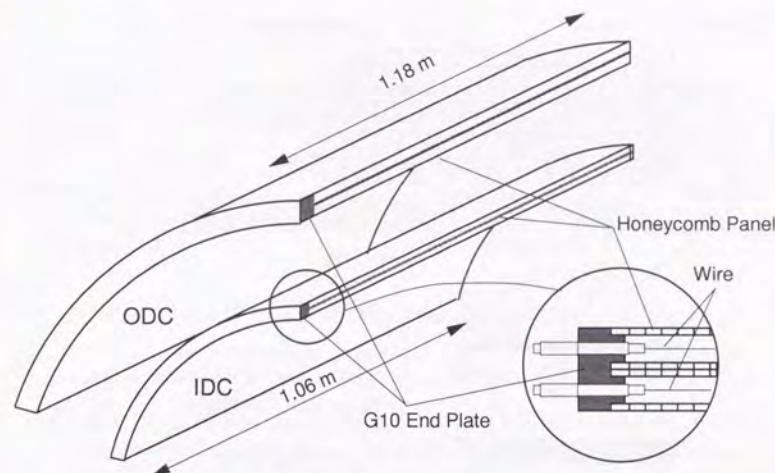


Figure 2.9: Diagram showing a cross-sectional view of IDC and ODC.

A high voltage of 2.7 kV (2.6 kV) is applied to the sense wires of the IDC (ODC), while  $-4.0$  kV ( $-4.5$  kV) to the field wires and field shapers. Figure 2.11 shows contours of the equipotential and electric field strength of the IDC. The electric field is inclined 5.5 degrees to the drift direction to compensate for the Lorentz angle produced by the magnetic field, and is constant across most of its drift region. The shape of the ODC's electric field is almost the same as the IDC's, with the exception that the Lorentz angle is negligibly small.

Both chambers are filled with the same gas mixture used in the JET chamber (90 %  $\text{CO}_2$ , 10% Ar).

The chamber signals from the sense wires and vernier pads are both amplified by preamplifiers mounted on an aluminum plate attached to the end-plate. Figure 2.12 shows a diagram depicting the read-out scheme of the IDC and ODC, where one signal is read from each IDC sense wire, two for each ODC sense wire, and four signals are read from each corresponding pair of vernier pads. Thus, a total of five or six signals are obtained per IDC or ODC sense wire. As explained next, these signals are distributed among amplifier and discriminator (AMP/DISCRIM) modules, analog-to-digital converter (ADC) and time-to-digital converter (TDC) modules, and flash-type analog-to-digital converter (FADC) modules.

1. The IDC and ODC sense wire signals are amplified and discriminated in the AMP/DISCRIM modules. If the discriminated signal in the inner and outer layer of each chamber coincide, they are fed through the track trigger (TT)



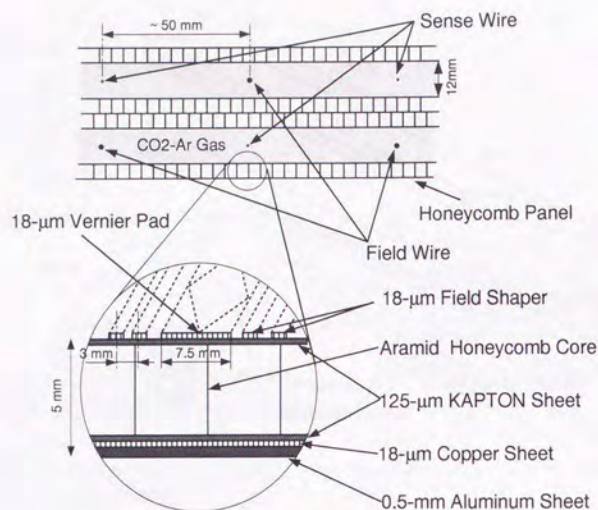


Figure 2.10: Diagram showing a cross-sectional view of the IDC and ODC in  $r\phi$  plane.

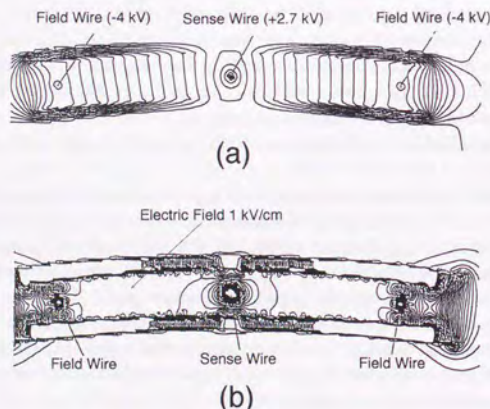


Figure 2.11: (a) Equipotential and (b) electric field strength contours of the IDC.

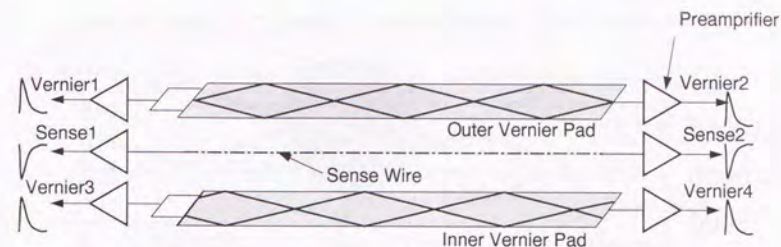


Figure 2.12: Read-out scheme for IDC and ODC signals.

module, which performs a rapid analysis of their rigidity (see Section 2.7.2).

2. The ODC sense wire signals are then fed to the TDC modules which convert their timing into 12-bit digits, while the ODC vernier signals are processed by the ADC modules which integrate their charge during a 500 ns gate and convert them into 12-bit digits. The timing information is utilized for determining the hit position of the ODC in the  $r\phi$  plane, while the charge information for determining the hit position along the  $z$ -axis.
3. The IDC vernier signals are processed and converted into timing and charge information by 28.5-MHz FADC modules and compressors in the same manner as the signals from the JET sense wires. Hit positions in the  $r\phi$  plane and along  $z$ -axis are respectively determined using the timing and charge information.

The hit positions of the IDC (ODC) in the  $r\phi$  plane are determined using the measured drift time. Briefly, the drift velocity is calibrated using the sum of the drift times of the inner and outer layers of the IDC (ODC), after which the polynomial corrections are applied to minimize errors in the tracks. The overall resolution of the  $r\phi$  plane is estimated to be  $200 \mu\text{m}$  based on the residuals obtained from the fitted track (Fig. 2.13). Figure 2.14 shows the IDC's  $r\phi$  resolution as a function of (a) the drift distance and (b) the angle of the track trajectory with respect to the axial direction, where both resolutions are gradually degraded according to the drift distance and angle.

The hit position along  $z$ -axis is measured using the signals generated on the corresponding sets of vernier pads, *i.e.*, each pad is situated on the inner and outer KAPTON sheet such that they surround one sense wire [47]. Each set is cut as shown in Fig. 2.15, having a cycle of 100 mm for the IDC (120 mm for the ODC). The corresponding set of pads are situated such that they are shifted along  $z$ -direction by a quarter cycle with respect to another.

When the drifted electrons avalanche near a sense wire and deposit their charge on it, induced signals are generated on the corresponding set of pads. The charge on each pad is divided into the two parts (A and B) of the pad and the both charge



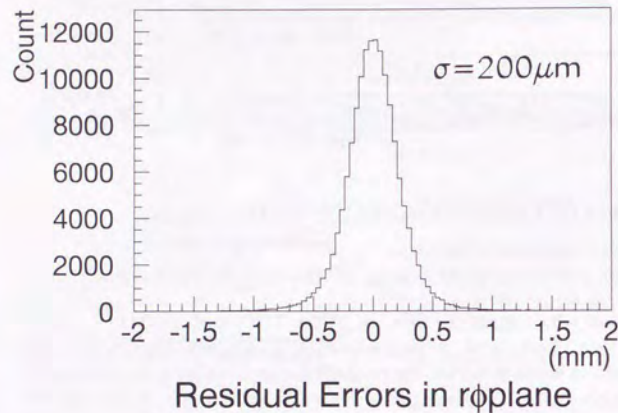
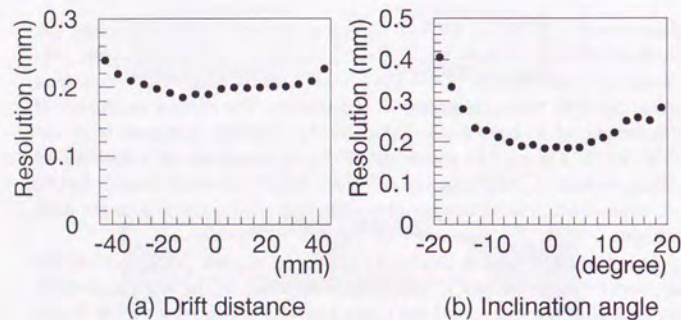
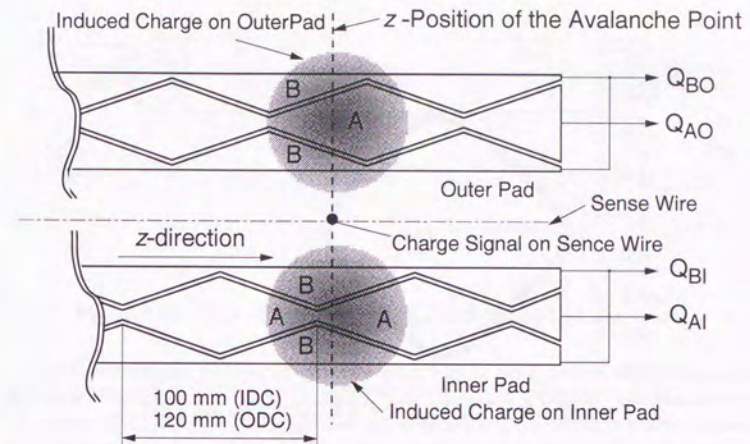
Figure 2.13: Residual distribution of the IDC  $r\phi$  hit points.Figure 2.14: IDC  $r\phi$  resolution as a function of (a) drift distance, and (b) angle  $\phi$  with respect to the axial direction.

Figure 2.15: Corresponding sets of vernier pads.

are separately read out. We define the normalized charge ratio of A and B for each pad as:

$$\epsilon_{I(O)} = \frac{Q_{AI(O)} - Q_{BI(O)}}{Q_{AI(O)} + Q_{BI(O)}}$$

where  $Q_{AI(O)}$ ,  $Q_{BI(O)}$  are the charge on A and B for inner pad (outer pad), respectively. Each  $\epsilon$  parameter is linearly related to the  $z$ -axis position of the avalanche point. Figure 2.16 shows the scatter plot of the  $\epsilon$  parameter. One cycle around the round square locus represents a movement of 100 mm (120 mm) along  $z$ -axis. The line in the figure shows the  $\epsilon_1$  and  $\epsilon_0$  calculated numerically for various  $z$ -position. We can then derive the hit position along the  $z$ -coordinate by comparing the measured  $\epsilon$  pair to the numerical calculation. The spread of the measured  $\epsilon$  values around the numerical line provide the estimation of the  $z$ -axis resolution (Fig 2.17). When the coarse  $z$ -position obtained by the charge division of the JET chamber, absolute  $z$ -position can be determined by the precision of 350  $\mu$ m.

## 2.5 Time-of-Flight Hodoscope

### 2.5.1 TOF Hodoscope in BESS '93 and '94 instrumentation

In BESS '93 and '94 instrumentation, the Time-of-Flight hodoscope (TOF) consists four upper and six lower plastic scintillation counters which are placed just outside the ODC at the radius of 65 cm



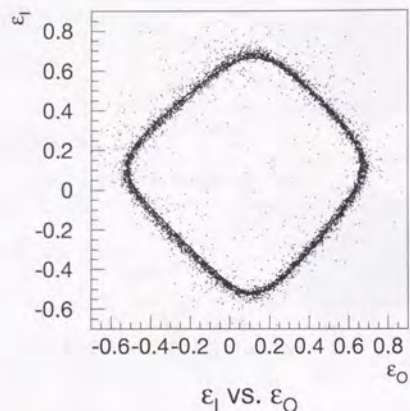
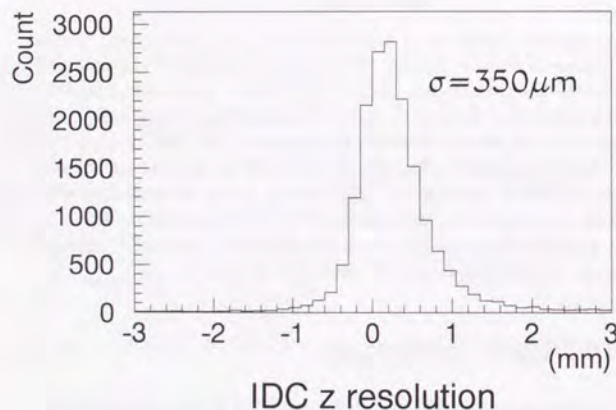
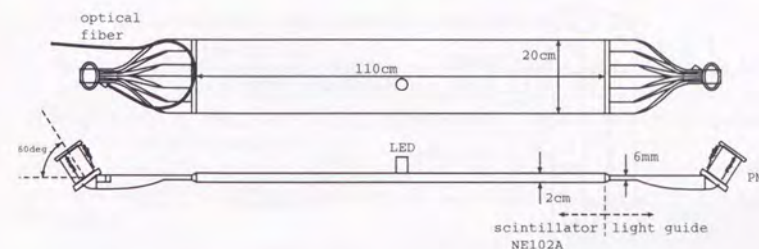
Figure 2.16: Scatter plot of the  $\epsilon$  parameter of the inner and outer pad.Figure 2.17: Spatial resolution of the  $z$ -coordinate measurement in the IDC.

Figure 2.18: Time-of-flight counter of BESS '93 and '94 instrument.

Each scintillation counter, shown in Figure 2.18, is composed of a NE Technology NE102A scintillator with dimensions  $110 \text{ cm} \times 20 \text{ cm} \times 2 \text{ cm}$  and two Hamamatsu Photonics H2611SXA photo-multiplier tubes (PMTs) with  $36 \text{ mm}\phi$  photo-cathode. The light signals are transmitted in the scintillator and are guided adiabatically through the twisted-strip acrylic light guide to the photo-multiplier tubes (PMTs) on both ends. For a daily check and calibration use, there equipped a light-emitting-diode (LED) at the center of the scintillator, and the connector for the laser light are fixed on the side of the light guide. The whole counter is wrapped with one layer of aluminized mylar and two layers of black vinyl sheet to reflect the light and to shield the light from outside, respectively.

Since the PMTs are operated in the magnetic field of  $1.8 \text{ kG}$ , where ordinary PMTs could not be used, we use PMTs with 19 stages of mesh-typed dynodes, which is specially designed for usage in a high magnetic field. Besides, to reduce the effect of the field, the axis of the PMT is aligned with the field direction by  $15$  degrees. The test of PMT in the  $1.8 \text{ kG}$  reveals that the PMT gain increases by at most  $10\%$  and the timing shifts by  $100 \text{ ps}$ , however, no degradation in the timing resolution is observed. Various high voltage values between  $-1.7 \text{ kV}$  and  $-2.1 \text{ kV}$  are applied to adjust the gains of all PMTs to the same value.

The output signals of the counter are utilized for three different purposes; a timing measurement, a charge measurement, a fast trigger. To avoid interference with one another, three signals are extracted separately from the anode, 19th dynode, and 18th dynode, respectively (Fig. 2.19). Each signals are processed in the following ways:

- The anode signals are used for generating the stop signal in the timing measurement. They are discriminated by a CAMAC discriminator (DSC) module and fed into the CAMAC TDC through a  $150 \text{ ns}$  delay cable. The threshold of the DSC can be set via CAMAC command in  $0.75 \text{ mV}$  step. Although the minimum threshold of DISCRI can be set as low as  $5 \text{ mV}$ , a value of  $10 \text{ mV}$  ('93) and  $15 \text{ mV}$  ('94 and '95) is selected to compromise between the timing resolution and the probability of spurious stop signal due to noise of the electronics. The TDC is a modified version of Lecroy 2208, which accepts eight



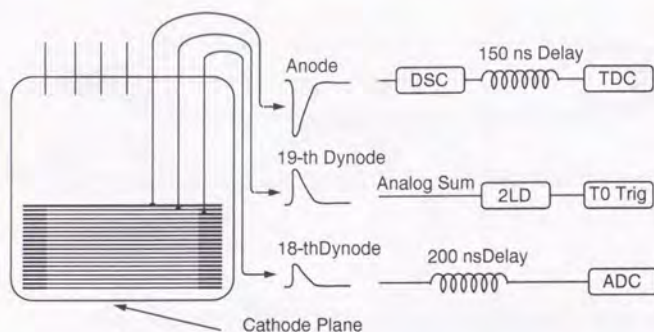


Figure 2.19: Read-out scheme for PMT signals.

ECL-level signal from the DSC and one NIM-level start signals from a T0 trigger module. The dynamic range is 11 bits and conversion gain is 50 ps/count. According to the test, the timing resolution of 70 ps and the linearity of 0.1 % over a full scale are obtained. Since inductive parts are used in the oscillator circuit, the timing conversion gain is shifted by 6 ~ 7 % in the actual operating field. However there is no effect on TDC resolution and linearity.

- The 19th dynode signals are used for generating a fast trigger signal. First each PMT signal at the both ends is summed up after integration with time constant of 20 ns to reduce the position dependence of the signal amplitude. The summed signals are fed into the two-level discriminator (2LD) modules, which has a capability of setting two level thresholds for all eight channels. One threshold is set to 30 mV, which corresponds to 30 % of the minimum ionizing pulses. The other is set to 150 mV ('93) and 160 ~ 250 mV for the multiple charged particles. Four kinds of the 2LD outputs, *i.e.*, top low-threshold (LOW), top high-threshold (HIGH), bottom LOW, bottom HIGH are ORed separately in the 2LDs. The resultant four signals are fed into the T0 trigger module to generate a fast trigger pulse by combining them. Detailed trigger scheme will be described later in Section 2.7.
- The 18th dynode signals are utilized for the charge measurement. It is fed to a charge-to-voltage type analog-to-digital-converter (ADC) module [48], which is the same module as used to read the vernier signals of ODCs, through a 200 ns analog delay line. The charge is integrated during the gate width of 250 ns and converted into 12 bit digits. The conversion gain is 0.6 pC/count. The integrated nonlinearity is below 1 count over the full-scale, which provide a wide dynamic range of charge measurement, from 1/20 to 100 times as large as the charge corresponding to minimum ionizing particles. The intrinsic resolution of the charge measurement is 10 % for minimum ionizing particles,

which is dominated by photo-electron statistics in the PMT.

The gain and timing of each counter were first calibrated using the beams from the proton synchrotron at KEK before the installation. Protons and pions with 1 GeV/c is used to determine the high-voltage applied to each counter and parameters for a time-walk correction.

After installation into the BESS instrument, the gain and the timing are monitored and calibrated both in the ground and in the flight situation by the following three ways:

1. The laser light pulsar (Hamamatsu PLP-02) is used for the precise measurement of the TDC conversion gain and timing offset for each counter in the actual operating condition. The output light has a wave length of 410 nm and is led into the counter through a 1 mm $\phi$  quartz fiber. The excellent stability of the pulse height and the timing of laser pulse enable to calibrate the timing and gain of each counter, though this calibration scheme is not available when the endcap is closed.
2. The blue LED light is also used to monitor the gain and timing of the counters. Although LED signals have slower rise-time and less stability than the laser signals, there are two advantages in the calibration with the LED. Calibration can be performed even after the pressure vessel closed. PMTs at both ends are simultaneously calibrated and their gain can be relatively adjusted.
3. In the flight situation, cosmic-rays are used to determine all calibration parameters used in the off-line analysis. Since both the gain and the timing fluctuate according to the temperature during the flight, we divided the flight data into several runs and calibrate them in the individual run.

The performance of the TOF counter is studied using the '93 flight data samples. Figure 2.20 shows the  $z$ -dependence of the PMT charge measured for the proton samples with the rigidities above 5 GV. The charge is corrected for angle of incidence on the counter. Figure 2.20-(a) shows the charge distribution versus the  $z$  position. The line in the figure indicates the fitted curve for the peak of the distribution using the following equation, *i.e.*,  $a + be^{cz}$ , where  $a, b$  and  $c$  are parameters to be fitted. Figure 2.20-(b) shows the charge distribution at  $z = 0$ . The resolution determined from the distribution below peak is about 10% at the center of the counter, which means that about forty photo-electrons are obtained for energetic protons. Figure 2.21-(a) shows the timing resolution of the PMT versus the  $z$  position. At the center of the counter, the timing resolution of 300 ps is observed. Figure 2.21-(b) shows the timing resolution versus square root of the number of the photo-electrons ( $N_{pe}$ ). The linear correlation between two variables is clearly observed.

Figure 2.22 shows the residuals of measured TOF from the expected TOF for proton sample and helium sample in BESS '93 flight data. These are calculated by following equation;

$$\Delta\text{TOF} = \text{TOF}_{\text{meas}} - L/v$$



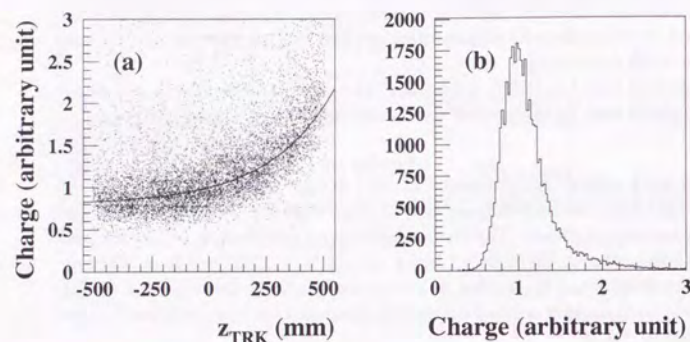


Figure 2.20: (a)  $z$ -position dependence of the measured PMT charge. (b) Charge distribution at the center of the counter ( $z = 0$ ) ('93). Charge is corrected for angle of incidence on the counter.

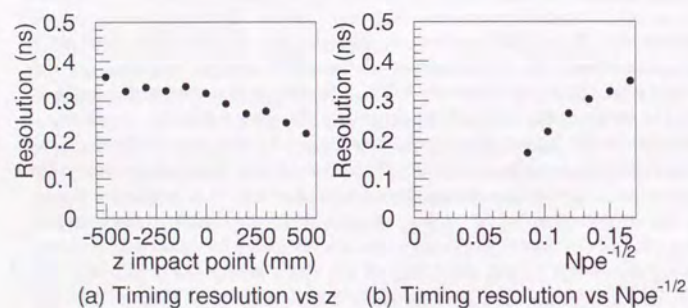


Figure 2.21: Timing resolution as a function of (a) the  $z$ -position and (b) square root of  $N_{pe}$  at the center ('93).

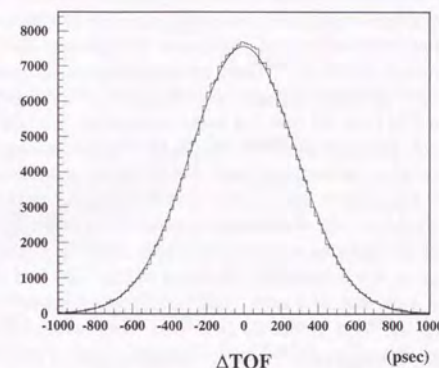


Figure 2.22:  $\Delta\text{TOF}$  for proton events with the rigidities above 5 GV ('93).

where  $L$  is the path length and  $v$  is the velocity, which is calculated from the measured momentum and mass of the identified particle species. The curves in the figure are the results of Gaussian fit and the resultant sigmas are 280 ps for protons.

### 2.5.2 TOF Hodoscope in BESS '95 instrumentation

In order to obtain better timing resolution, TOF system was improved in BESS '95 instrument, where eight upper and twelve lower plastic scintillation counters with a dimension of 95 cm  $\times$  10 cm  $\times$  2 cm were installed. The schematic view of a single new TOF counter is shown in Figure 2.23.

For the design of a new TOF counter, an optical simulation program GUIDE 7 [49] was used. From the simulation, it was concluded that the width of scintillator should be much narrower for better timing resolution, and the fish-tail type light guide is more efficient than the twisted-strip type in this case. Careful considerations



Figure 2.23: Time-of-flight counter of BESS '95 instrument.



resulted that the LED should not be fixed to the new counter because the hole defect of mylar sheet would degrade the reflection efficiency. From the constraints of the number of the readout electronics and the power dissipation, the width of a single paddle was determined as 10 cm. Then some prototype counters which had Bicon BC404 and BC420 scintillators with various types of light guide, were made, employing the same PMT as '93 and '94 instrumentation, *i.e.* H2611SXA. Related with the direction of the magnetic field, the PMT attachment angles of 60 and 90 degrees were tested using proton and pion beams with momentum of 1.1 and 2.0 GeV/ $c$  at KEK PS. From these beam tests, it was concluded that BC404 is preferable than BC420, the angle of the attachment should be 90 degrees, and then the timing resolution of 100 ps might be expected in a real scientific flight. Finally the design of new TOF counter was determined as shown in Fig. 2.23 and they were fabricated. Then the scintillator part of a new TOF paddle was wrapped with one layer of Millipore sheet and the light guides at both ends were wrapped with one layer of aluminized mylar to obtain good efficiency of the reflection. Furthermore, a part of the light guide near the PMT is wrapped with one layer of silver mylar. At last, the entire counter is wrapped with two layers of black vinyl sheet to shield the light from outside.

Although the fundamental readout method was not changed, the number of the TDC and ADC electronics were doubled and especially, the new TDC modules [50] were installed according to the improvement of the counter. The new module's conversion gain is 25 ps/count and the dynamic range of 12 bits. The integrated nonlinearity is below 1 count in the time range of more than 80 ns. In addition, invulnerability in magnetic field and low power consumption were realized. The high voltage supply unit of the TOF system was also improved in the conversion efficiency to save power consumption.

After simple calibration of the new TOF counter with the beam test data, the system was installed in the BESS instrument. Then the gain and timing of each counter were thoroughly calibrated using the data obtained from cosmic ray runs by the whole detectors on the ground. Then various high voltage values between -1.6 and 2.0 kV were applied to adjust the gains of all PMTs to the same value.

The performance of the TOF counter is studied using the '95 flight data samples. Figure 2.24 shows the  $z$ -dependence of the PMT charge measured for the proton samples with rigidities above 5 GV. Figure 2.24 shows (a) the charge distribution versus the  $z$  position and (b) shows the charge distribution at  $z = 0$ . The resolution determined from the distribution below peak is about 6 % at the center of the counter, which means that about 120 photo-electrons are obtained for energetic protons. Figure 2.25 shows the residuals of measured TOF from the expected TOF for proton and helium samples in BESS '95 flight data. The curves in the figure are the results of Gaussian fit and the resultant sigmas are 110 ps for the protons.

## 2.6 Čerenkov Counters

BESS was designed for the purpose of search for antiproton, as well as antihelium.

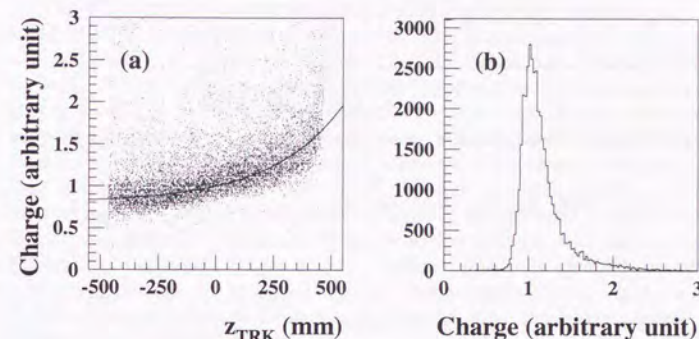


Figure 2.24: (a)  $z$ -position dependence of the measured PMT charge. (b) Charge distribution at the center of the counter ( $z = 0$ ) ('95). Charge is corrected for angle of incidence on the counter.

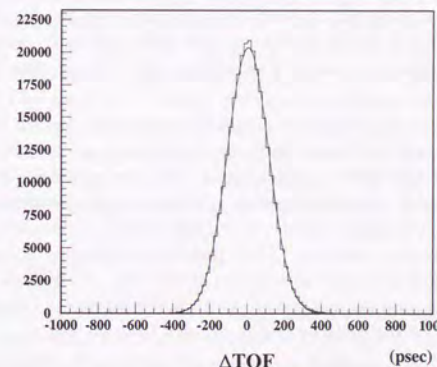


Figure 2.25:  $\Delta\text{TOF}$  for proton events with the rigidities above 5 GV ('95).



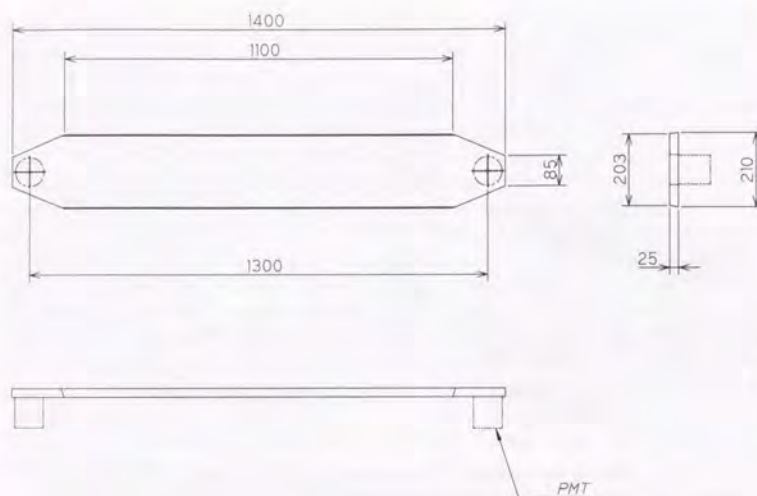


Figure 2.26: Čerenkov counter of BESS '95 instrument.

From the results of '93 flight, the  $\bar{p}/p$  ratio was shown up below the kinetic energy of 0.5 GeV [33]. In order to determine the flux ratio up to 1 GeV, Čerenkov counter was designed for BESS '94 instrument. A prototype counters were made and tested by the  $\pi^2$  beam line of KEK PS. Then, it was concluded that up to the momentum of 1.7 GeV, protons can be clearly separated from lighter particles, *i.e.* mainly pions, muons and electrons.

Figure 2.26 shows a schematic view of a single Čerenkov counter. In BESS '94 instrument, the single counter, 1500 mm (250 mm of tapering part to each end)  $\times$  240 mm  $\times$  23 mm, is made with UVT acrylic plastic, and is wrapped in aluminized mylar to obtain good efficiency of light reflection. Originally, the pressure vessel of BESS '94 instrument was not designed to carry Čerenkov counter inside, hence it was installed outside to be operated in vacuum. Three paddles of Čerenkov counter were arranged cylindrically around the vessel at a radius of 820 mm. Each single counter was viewed on both ends by two vacuum-proof photomultiplier tubes (Hamamatsu R5542SP), whose diameter of the photo-cathode is more than 64 mm.

In BESS '95 instrument, the pressure vessel was extended so that the Čerenkov counter was installed inside. In the result, the counter was arranged much closer to the the bottom TOF counter, where no more aluminum vessel wall of 2 mm thickness, and photomultiplier tubes was changed to Hamamatsu R5542S which isn't vacuum-proof tubes. In addition, wrapping was changed to Millipore sheets for better efficiency of light reflection.

## 2.7 Trigger

The BESS trigger system was designed for the primary objective of the BESS experiment, to detect signals of antiprotons and antiheliums efficiently. Because of a large geometrical acceptance, a primary (T0) trigger rate of the BESS detector exceeds a few thousand per second, which is far above the maximum rate to be able to handle by the BESS data acquisition system (see Section refsec:daq). We adopted a trigger scheme biased toward negative charged particles in order to reduce the high trigger rate, in which events of protons and heliums, the dominant component of the cosmic radiation, were to be discarded and the population of negative charged particles were to be relatively enriched in the collected data. For a diagnostic purpose, samples of unbiased events were also collected and used to obtain the efficiency of the biased trigger and the fluxes of positively charged particles. The trigger system was also equipped with two other trigger modes, one for a study of future experiment plan on gamma rays, and the other for external inputs used in calibrations on ground.

The BESS trigger system is composed of three trigger modules (T0 Trigger, Track Trigger and Master Trigger), and produces two level triggers (T0 and MT). The T0 trigger module produces T0 data words and "T0" triggers from the signals at the top and the bottom scintillation counters. These first level triggers are "fast" triggers to start digitizations of the read-out signals and also activate the other trigger modules. The Track Trigger module produces "TT" data words from the hit patterns in IDCs and ODCs. These signals assure that an incident particle passed through drift chambers (JET/IDCs/ODCs) while "T0" triggers do not, though they are rather slower because of drift time in drift chambers and cannot be used as "fast" triggers. The main purpose of Track Trigger module is to bias the events to be collected toward those of negatively charged particles. The sign of the deflection of incident particles are to be determined by the hit patterns. The Master trigger module produces "MT" triggers from T0 data words and TT data words, some of which are "biased" triggers for negatively charged particles and others are "unbiased" sampling triggers of "T0" triggers. These are the second level triggers to start data gathering processes. The Master trigger module also produces "fast clear" signals to stop the digitizations and reset the read-out and the trigger modules in case that a "MT" trigger is not produced after the system is activated by a "T0" trigger.

### 2.7.1 T0 Trigger

The T0 triggers are the first level or "fast" triggers to start the read-out electronics digitizing the signals. Once a T0 trigger is produced in the T0 trigger module from the signals of the scintillation counters, no T0 trigger will be produced again until the T0 trigger module is reset by a clear pulse, *i.e.*, the T0 triggers are locked out during the digitizing and data gathering processes. There are four modes to produce T0 triggers:

- Low — aiming at charged particles.



- High — aiming at  $z \geq 2$  charged particles.
- Gamma — aiming at gamma-rays.
- External — initiated by an input signal and used for diagnoses and calibrations of the instrument.

A "Low" trigger is produced from a simple coincidence of hits at the top and the bottom scintillation counter. A "High" trigger is produced when the both hits at the top counters and the bottom counters provide high amplitudes. It is clear that a "Low" trigger will be produced at the same time. A gamma-ray would possibly be converted into an electron-positron pair at the coil of the magnet and detected at the drift chambers and the bottom scintillators, where there are no hits in top scintillators and some hits in bottom. A "Gamma" trigger requires that there is null hit in top scintillators and at least one hit in bottom scintillators.

To sum up, the T0 trigger module used the four signals of 2LD modules, *i.e.*, top low-threshold (LOW), top high-threshold (HIGH), bottom LOW, and bottom HIGH, to produce T0 triggers by following logics;

- T0-Low —  $\text{top-Low} \wedge \text{bottom-Low}$
- T0-High —  $\text{top-High} \wedge \text{bottom-High}$
- T0-Gamma —  $\overline{\text{top-Low}} \wedge \text{bottom-Low}$
- T0-External — External input

The module is equipped with trigger reduction circuits for all four modes to be used when the T0 trigger rate is too high. The reduction rates  $1/N$  are set by a CAMAC command, and they can be changed even during the flight. In the experiment, since we activated T0-Gamma mode only for a study of the gamma-ray triggering, and the trigger rate for the mode is about the sum of the single rate of the TOFL counters reaching a too high rate of about 20kHz, the reduction rate for the mode was selected to be  $1/256$ . The reduction rates for other trigger modes were set to  $1/1$ , *i.e.* no reduction, and not needed to be changed during the experiment.

### 2.7.2 Track Trigger

The Track Trigger module provides the TT data words from the hit pattern of IDCs and ODCs, which were used to produce the triggers "biased" toward negative charged particles. In Fig 2.27 is shown the basic concept of the TT. The signal of the sense wires of IDCs and ODCs are discriminated and fed into the coincidence modules. They are then combined into "hit-cell" signals by requiring the coincidence of two nearest wires in different layers of each IDC/ODC by which spurious hits caused by electric noise or by radiations from local radio-activated materials are eliminated, and the width of the possible range of the hit points are halved. Total of 30 and 22 cells are defined in each ODC and IDC, respectively. The hit-cells give

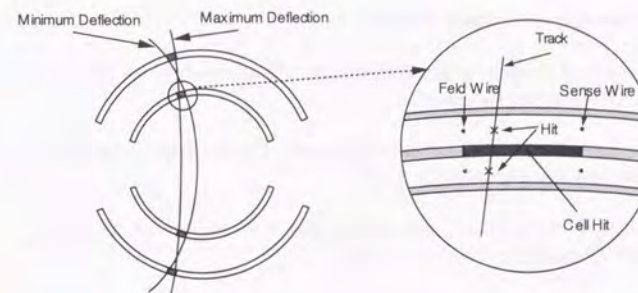


Figure 2.27: Basic scheme of the Track Trigger.

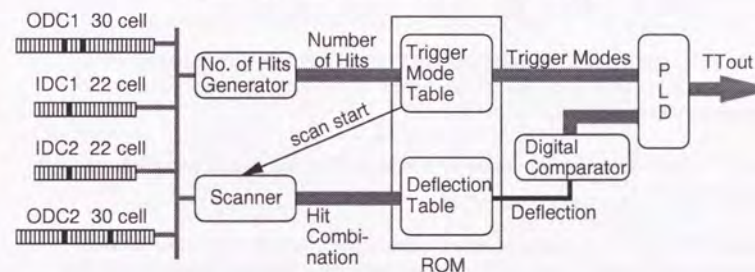


Figure 2.28: Block diagram of TT process.

coarse hit position information with a resolution of the cell width, *i.e.* about 50 mm, and a combination of three or four hit-cells from four drift chambers provides rough estimation of the deflection ( $\equiv \text{rigidity}^{-1}$ ) of the incident particle. The two trajectories in Figure 2.27 are shown to illustrate the possible maximum and minimum deflections for a certain combination of hit-cells. We define the mean value of two deflections as a deflection of the hit-cell combination. By calculating the deflection for all hit-cell combinations, and storing them in a look-up table beforehand, a quick deflection analysis is possible without any time-consuming calculation.

The Track Trigger module consists of a 2 Mbyte read only memory (ROM) as the look-up table and a microcode-programmable sequencer, and carries out the event selection (Figure 2.28). The selection scheme can be programmed with 8 modes and output data of the module are 8-bit data words corresponding to them. The modes were programmed as follows;

- Mode 1:  $\bar{p}$ -clear — A mode to select antiprotons. The numbers of hit cells in



the four drift chambers are strictly limited.

- Mode 2:  *$\bar{p}$ -dirty* — A mode to select antiprotons. The numbers of hit cells in the four drift chambers are less limited.
- Mode 3:  *$\overline{He}$ -clear* — A mode to select antiheliums. The numbers of hit cells in the four drift chambers are strictly limited.
- Mode 4:  *$\overline{He}$ -dirty* — A mode to select antiheliums. The numbers of hit cells in the four drift chambers are less restricted.
- Mode 5: *Missing-a-hit* — A mode to select negatively charged particles with only three hit cells in four chambers. The chambers have some 'dead' region near the sense wires for the signals of the hits near the wires are fed into the electronics earlier than the trigger activates them. The events of negatively charged particles with such a 'missing hit' can be selected here.
- Mode 6: *Multi-clear* — A mode to select negatively charged particles which could not selected the modes above. This time extra hits due to noise or interactions are considered.
- Mode 7: *Multi-dirty* — The same as Mode 6. The number of extra hits are less restricted.
- Mode 8: *Gamma* — A mode to select gamma-ray events in which the incident gamma-ray is converted into a electron-positron pair, making hits in two IDCs and the bottom ODC.

The selections are performed in two stages, hit-pattern selection and deflection selection.

### Hit-pattern selection

Events with too few or too many hit cells were eliminated before examining the deflection of tracks. Most of the events with showers or without tracks in JET chamber were rejected by this selection. Different selection conditions were set for the individual selection modes. The "number of hits generator" logic circuit yields the total number of hit-cells of each drift chamber, the set of which makes a address of the "Trigger Mode Table", which is stored in a half of the ROM look-up table. The combinations and the permutations of the numbers of hit-cells are examined by this table and resulting Trigger Mode bits are produced. The number of hits conditions for each trigger mode are summarized in Table 2.7.2. If any of the hit-pattern selection conditions is satisfied, a "scan-start" will be issued to the scanner so as to initiate the deflection selection.

Table 2.3: The conditions of the Track Trigger hit-pattern selection.  $C(i,j,k,l)$  means any combination of  $N_{i1}, N_{i2}, N_{o1}, N_{o2}$  matches  $(i,j,k,l)$  and  $P(i,j,k,l)$  means the permutation  $(N_{iu}, N_{il}, N_{ou}, N_{ol})$  matches  $(i,j,k,l)$ , where  $N_{iu}$  — the number of hit-cells in upper IDC,  $N_{il}$  — the number of hit-cells in lower IDC,  $N_{ou}$  — the number of hit-cells in upper ODC,  $N_{ol}$  — the number of hit-cells in lower ODC.

Mode	BESS '93	BESS '94 and '95
1	$C(1,1,1,1)$	$C(1,1,1,1), C(1,1,1,2)$
2	$C(1,1,1,2)$	$C(1,1,1,3), C(1,1,2,2)$
3	$C(1,1,1,1)$	$C(1,1,1,1), C(1,1,1,2)$
4	$C(1,1,1,2)$	$C(1,1,1,3), C(1,1,2,2)$ $C(1,1,2,3), C(1,2,2,2)$ $C(1,2,2,3), C(2,2,2,2)$ $C(1,1,3,3)$
5	$C(0,1,1,1)$	$C(0,1,1,1)$
6	$P(1,1,1,i), (i=3,4)$ $P(1,1,2,j), (j=2,3,4)$	$P(1,1,i,j), (i,j=1,2,3,4)$
7	$P(2,i,j,k), (i=1,2)$ $(j=1,2,3), (k=1,2,3,4)$ except for $P(2,1,1,1)$	—
8	$P(0,i,j,k) (i,j,k=1,2)$	$P(0,i,j,k) (i,j,k=1,2)$



### Deflection selection

The events that have passed through the hit-pattern selection are then subject to the deflection selection. All possible combinations of hit-cells are scanned and the pattern of the four hits (one hit in each drift chamber) makes an address to refer the "Deflection Table", which is stored in the other half of the ROM look-up table. The output deflection is compared with the seven threshold values, each of which corresponds to one of the selection modes, except that the thresholds for Multi-clear and Multi-dirty are common. If the deflection is above some of the thresholds, *i.e.*, the track has more negative deflection than the threshold, a bit corresponding to the mode in the TT output data word is asserted.

The Mode 2 and 4 ( $\bar{p}$  and  $\bar{\text{He}}$  dirty) were less accurate in deflection resolution than Mode 1 and 3, and their deflection threshold were set higher than that of Mode 1 and 3. Since the population of heliums in the cosmic rays are less than protons, the deflection threshold of Mode 3 and 4 were set looser than that of Mode 1 and 2. The Mode 6 and 7 in BESS '93 flight were prepared as an insurance in case of the Mode 1 to 4 not working well. In fact, the efficiency of the hit-pattern selection was very low because of much more extra hits than expected, which were produced by cross-talks. In BESS '94 and '95 flight, the thresholds of the discriminators were tuned and the hit-pattern conditions were less strict, the efficiencies was much higher than in BESS '93 flight. The Mode 6 was used especially aiming to select antiprotons which annihilated at the bottom of the instrument.

Figure 2.29 shows the efficiency of the rigidity selection as a function of deflection calculated by the simulation. The threshold values indicate the deflections where the efficiency become 50 %. The left figure is for the threshold used for the  $\bar{p}$  selection in the BESS '93 flight. The right figure is for the threshold used for an antihelium selection. The curve for the  $\bar{p}$  selection is set being shifted to the negative direction

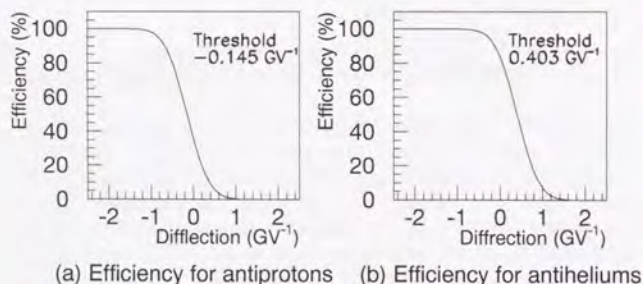


Figure 2.29: Simulated Track Trigger efficiency. (a) for the  $\bar{p}$  search (b) for the antihelium search.

compared to that for the antihelium selection because a large number of protons should be cut more tightly by the rigidity selection.

### 2.7.3 Master Trigger and Fast Clear

The Track Trigger module only concerns the hit-pattern and deflection of the particles. The Master trigger module combines the signal size information from the T0 Trigger module, with which protons and heliums are discriminated, and the track information from the Track Trigger module, with which the signs of the charge of the particles are discriminated. Here the categorization  $\bar{p}$  and  $\bar{\text{He}}$  in the Track Trigger module are added the real sense. The Master Trigger module also generates unbiased triggers by sampling the T0 Trigger at a rate. There equipped 12 sampling circuits corresponding to 4 T0 Trigger modes and 8 Track Trigger modes. In a sampling circuit is used a count down IC, and loading a number  $N$  to it, a reduction rate  $1/(N+1)$  will be obtained. The MT trigger is generated as the logical 'OR' of the twelve modes. If no MT trigger is generated, a fast clear signal is issued to the "Fast Clear" module. The Fast Clear module issues clear signal to all read-out electronics and then clear the lock-out of the T0 Trigger module making the system ready for the next event.

## 2.8 Data Acquisition System

The BESS data acquisition system is required to handle a high trigger rate of about 2 kHz due to the large geometrical acceptance and a large data size of about 1.2 kbytes per event yielded by the large number of signal read-out. The system has a capability to gather the data of each single event within 1.2 ms, utilizing multi-processor and pipe-line scheme, and to store the data up to 10 Gbytes with a recording rate of 500 kbytes/s [51]. Thus, it is necessary to reduce the trigger rate down to a few hundred hertz so as to restrain the dead-time of the system at an approvable amount. As described in Section 2.7, the trigger system is capable to reduce the second level (MT) trigger rate. The parameters of reduction scheme are adjusted to make a MT trigger rate of about 100 to 200 Hz.

It is also important for a balloon-borne experiment to reduce the power consumption. The amount of batteries possible to be loaded is limited in view of the maximum total weight of the payload. A larger power consumption demands more batteries resulting in a smaller margin of the weight, or shortens the exposure time of the experiment. It also produces a larger amount of heat in the instrument and causes a cooling problem. To avoid these problems, most of the electronics are self-made or custom-made being reduced in power consumption while retaining the processing speed and desired resolutions.

Figure 2.30 shows schematic view of the BESS data acquisition system. The system is composed of four subsystems which function as follows:

- Communication subsystem manages the communication between the data acquisition system on-board and the ground system. It receives the commands



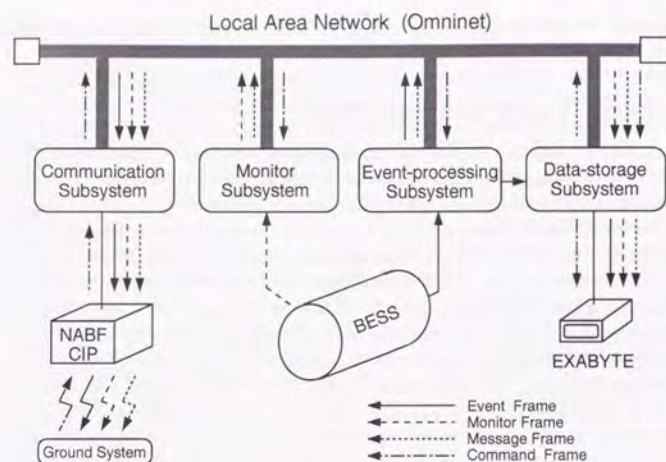


Figure 2.30: Schematic diagram of the data acquisition system.

from the ground system and deliver them to the proper subsystem. It also receives the data and the messages from the subsystems and send them to the ground system.

- Monitor subsystem gathers the house-keeping data such as temperatures and pressures inside and outside of the instrument.
- Event process subsystem gathers the event data and make event frames, then perform the on-line software reduction of the data.
- Data storage subsystem records the event data and house-keeping data gathered by the Event process subsystem and the Monitor subsystem, and also the commands and messages the Communication subsystem receives.

The four subsystems are linked with each other by a serial bus line composing a local network based on Corvus Omni-net protocol.  
through serial

### 2.8.1 Communication subsystem

The Communication subsystem is constructed in a STD-bus crate and controlled by a NEC V40 ( $\mu$ PD70208) CPU on a Yamashita Systems CMOS CPU-F microcomputer board [52]. It interfaces with the command/telemetry device provided by NSBF (the consolidated instrument package; CIP), and with the Omni-net bus.

The commands transmitted from the ground station to the payload are received by CIP, from which 16-bit data words are supplied with a strobe signal. The communication subsystem takes in those signals via photo-couplers for electrical isolation. The command words were sent at a rate of about 1 word/s.

The telemetry data such as messages from four subsystems, house keeping data from the Monitor subsystem, and event sample data from the Data process subsystem are gathered via the Omni-net. The data are fed to the CIP via a serial line and transmitted to the ground station. The capacity of the transmission was 10 kbyte/s.

### 2.8.2 Monitor subsystem

The Monitor subsystem is composed of a controller module constructed in a STD-bus crate and a digitizing module. The controller module is governed by a NEC V40 ( $\mu$ PD70208) CPU on a Yamashita Systems CMOS CPU-F microcomputer board. The digitizing module has 64 individual differential-amplifiers and one analog-to-digital converter and digitize various sensor signals: temperatures (16 points), pressures (10 points), magnet status (16 points), chamber high voltage status (10 points), and solar sensors and clinometers. The digitized data are sent to the Communication subsystem as telemetry data, and to the Data storage subsystem so as to be recorded in the magnetic tapes. Thus, the house-keeping data can be monitored during the flight as well as can be used in the off-line analysis.

### 2.8.3 Event Process subsystem

Figure 2.31 shows the block diagram of the Event Process subsystem together with the Data Storage subsystem. The main function of the subsystem is realized by INMOS transputers (shadowed boxes in the figure), which have a processing speed of 20 MIPS and a capability of parallel processing realized by hardware. The interfaces with the Omni-net is realized by Mikasa System Engineering pro216/II microcomputer board on which a NEC V50 ( $\mu$ PD70216) CPU is installed. The transputers are connected by point-to-point serial links, which has maximum transmission rate of 1 Mbyte/s. Four such links are equipped in each transputer and a complicated network can be constructed easily with a flexible configuration.

The signals from the detectors are fed into the ADC and TDC modules in the two CAMAC crates and FADC modules in the FADC crate. The CAMAC and FADC crate controllers are self-made using a transputer in each of them, and gathers the digitized read-out signals in parallel. The FADC crate controller also functions as the event builder and makes the event frames, packing the digitized data received from the CAMAC crate controllers with the FADC data. The event frames are fed into the transputer bank, where a single transputer processes the data, driven by the data, and functions as a filter. Thus, 9 events are possible to be processed at a time and the next event data can be gathered while the transputer bank is processing the previous event data. The number of transputers in the bank can be increased if necessary. The command links in the transputer bank is separated from the event data links, therefore the full band width of the event data links can be



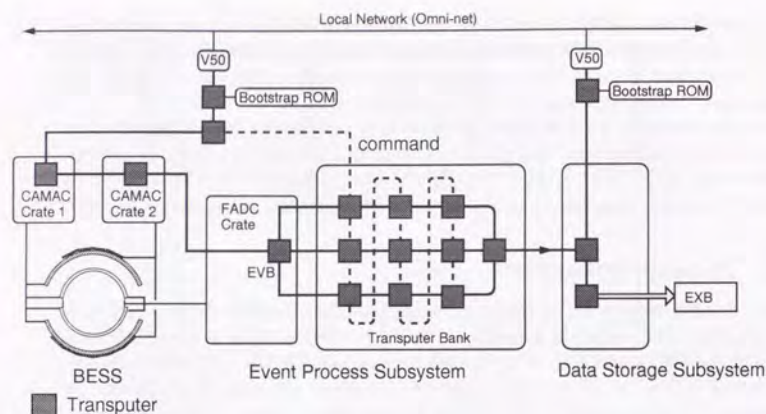


Figure 2.31: The block diagram of the Data Process and the Data Storage subsystem. A network of transputers are constructed for the main function of the subsystems.

utilized by the event frame flow. The data transmission by point-to-point links has an advantage that no arbitration method is needed.

#### CDC crates

The signals from the sense wires of IDCs and ODCs are fed into the CDC crates, where the amplifiers, the discriminators and the coincidence circuits are installed. The input signals from the drift chambers are amplified and then fed to the discriminators. The output signal of the discriminators are used as the input signals of the coincidence modules and also as the stop signals for the TDC modules in the CAMAC crate. The coincidence signals are used as the input to the Track Trigger module, providing the hit-cell information. The thresholds of the discriminators were too low in BESS '93, and as a result, there were noise hits in coincidence signals due to the cross-talks. This caused a lower efficiency of the Track Trigger in BESS '93.

#### CAMAC crates

Two CAMAC crates are used in the data acquisition system and contain the read-out modules such as ADCs and TDCs, and the trigger modules. Each crate is controlled by an intelligent crate-controller equipped with a transputer [53]. Thus, the data digitized at the modules in the CAMAC crates are gathered in parallel by the two crate controllers. The initial set up of the modules are also done by the crate controllers automatically. The modules installed in the CAMAC crates are:

- TOF read-out electronics Discriminators, TDCs, and ADCs to digitize the signals from TOF counters.
- ODC read-out electronics TDCs, and ADCs to digitize the signals from ODCs
- Trigger modules Discriminators for the signals from the scintillation counters (TOF counters) and T0, TT, MT trigger modules. Trigger conditions can be set or changed by the crate controller, using CAMAC commands. Trigger modes and other informations are read by the crate controller.
- 24-bit scalers Two 12-channel 24-bit scalers are installed to count the numbers such as the number of triggers, the number of coincidences. The trigger rates, the trigger efficiencies, and the dead time are derived using the scaler data. The scaler data are read only once a second to reduce the total data amount and the data gathering time.
- Event-timing module An event-timing module with a 0.1ms resolution is installed to obtain the time when the events are occurred.
- Gate generators Gate generators to make the gates for ADCs, the start pulses for TDCs and clear pulses for the adequate modules.

The data read from the modules are packed in the crate controllers and are transferred to the Event Builder via serial links. The CAMAC data of a single event amounts to about 300 bytes.

#### FADC crate

In the FADC crate are installed FADC modules, a compressor module, and a crate controller [54]. The signals from JET chamber and the vernier signals from IDCs are fed into FADC modules, and digitized with 8-bit resolution and 35-ns sampling period. The digitized values are stored into first-in-first-out (FIFO) memories after the zero-suppression process. The compressor module compresses the FADC data read from the FIFO's and extract the information of each pulse, such as timing, width, total charge, and the first two signal height data with which the pulse height can be estimated. The pulse information data are stored into the FIFO on the compressor module, and then read by the crate controller.

The FADC data of a single event amounts to about 700-900 bytes and are transferred to the Event Builder via the internal memory bus, since the Event Builder process runs on the FADC crate controller.

#### Event Builder

The data collected in parallel in the two CAMAC crates are transferred to the FADC crate controller via the serial links. The event-building process running in the transputer of the FADC crate controller gathers the CAMAC and FADC data, and packs them into a event frame. After packing the data, the Event Builder clears the



CAMAC and FADC modules using the Fast Clear module, and prepare for the next event. Then, one of three data transferring processes sends the event frame to the transputer bank via the corresponding serial link. The data-transferring processes run in parallel to each other, and also to the data gathering and event building processes. Thus, the event gathering and event building processes can be active even when a huge event or two take time to be transferred to the transputer bank. The event data of a single event amounts to about 1.0-1.2 kbytes typically and the event building process completes within 1.2 ms from the T0 trigger.

### Transputer Bank

The role of the transputer bank is a event-driven filter to sieve the events using the detector informations. It contains nine transputers (fifteen or more can be installed if necessary), arranged in three-by-three array (or three-by- $n$ ) and receives the event frames from the Event Builder via three serial links. All the transputers are programmed the same, and the individual transputer processes one event at a time. Thus, nine events can be processed in parallel.

The filtering process removes the junk events with too much FADC data, that is, with too many hits in JET chamber and IDC, and the events in which ODC hits and TOF hits are inconsistent. About 2 % of the events were removed by this process, and the numbers of events removed in these categories are added to the scaler data and also sent to the ground system. The process also removes the overflowed TDC data which do not contain hit informations, and reduce the event data size. The whole process completes within at most 20 ms and the transputer bank can handle 450 events per second.

In future the filter process will be more sophisticated in order to reduce the number of events to be recorded more effectively, and thus, to loosen the Track Trigger selection conditions. The reduction methods are in study using the real flight data.

### 2.8.4 Data Storage subsystem

In a part of Figure 2.31 is shown the Data Storage subsystem. In the subsystem the data frames received from other subsystems are recorded into cartridge tapes. A Mikasa System Engineering pro216/II microcomputer board with NEC V50 ( $\mu$ PD70216) CPU was employed for the communication via OMNI net. Transputer modules are employed for the main tasks of the data storage, one of which was a module specialized for the SCSI bus control. The monitor frames and the message frames are transferred via Omni-net, while the event frames are via a serial link which connected a transputer in the Data Process subsystem to another in the Data Storage subsystem. Two EXABYTE EXB-8500 (EXB-8505 for '95 flight) 8 mm tape data recorders were employed as the storage devices. The capacity of the tapes was 5 Gbytes each, providing 10 Gbytes of storage capacity in two tapes. The maximum data recording speed was 500 kbytes/s.

## Chapter 3

### Flight

The BESS apparatus was launched from Lynn Lake, Manitoba, Canada in the evening of July 26. in 1993, of July 31. of 1994, and of July 25. in 1995, close to the solar minimum as shown in Figure 3.1. In these flights, the balloon of 29 Mft<sup>3</sup> ( $8.3 \times 10^5 m^3$ ) lifted BESS detector into an altitude over 36 km (residual atmosphere of 5 g/cm<sup>2</sup>). The suspended weight was 2,700 kg consisting of 2,060 kg BESS apparatus, 330 kg ballast and others. (In 1995 flight, weight of BESS apparatus is 2190 kg and weight of ballast is 200 kg.) After about 20 hour level flight, the balloon flight was terminated under the condition of both magnetic field and power off. The instrument was recovered near Peace River, Alberta, which locates 1000 km east from Lynn Lake. Table 3.1 summarizes three flights from 1993 to 1995. The trajectories of each flight are shown in Figure 3.2.

Over these flights, the magnetic cutoff rigidity (Figure 3.3) seemed to be lower than the instrumental cutoff, for there were no significant changes in the spectral shape of the proton flux obtained in the analysis.

The environment in the pressure vessel was kept in good state, as shown in Figure 3.4, 3.5 and 3.6, the temperature of JET chamber was kept within 16°C and 34°C and the pressure was kept within 975g/cm<sup>2</sup> and 1044g/cm<sup>2</sup> in 1995.

Table 3.1: Flight summary of BESS experiment.

	BESS '93	BESS '94	BESS '95
Launching date	July 26, 1993	July 31, 1994	July 25, 1995
Launch site	Lynn Lake, Manitoba, Canada 56°48'N, 101°25'W		
Floating altitude		> 36 km	
Floating time	17 hours	20 hours	20 hours
Landing site	57°52'N, 117°30'W	55°89'N, 114°06'W	55°32'N, 115°06'W
Detector weight	2060 kg	2060 kg	2190 kg
Ballast weight	330 kg	330 kg	200 kg
Observation time	13 hours	12 hours	14 hours
Recorded events	$3.6 \times 10^6$	$4.7 \times 10^6$	$4.6 \times 10^6$



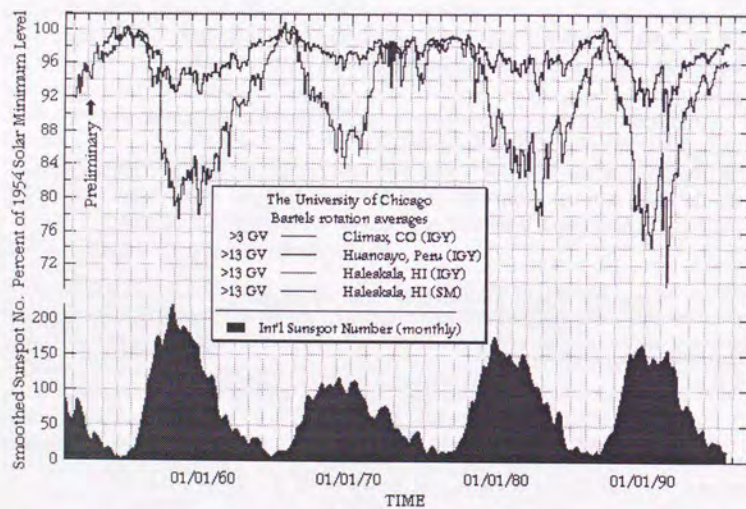
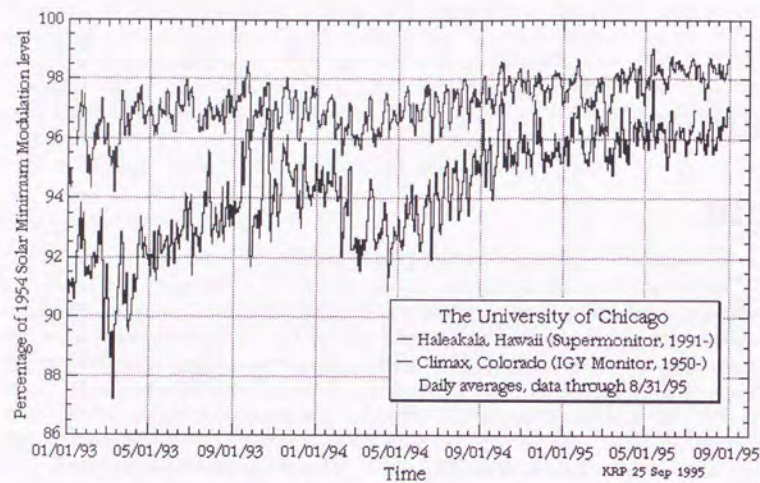


Figure 3.1: The data of neutron monitors provided by the University of Chicago.

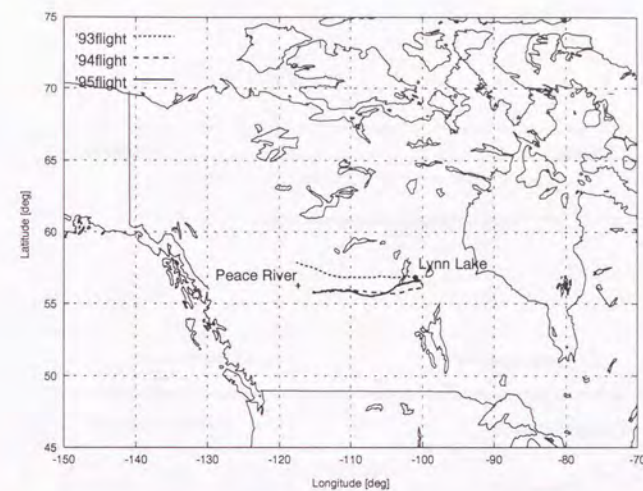


Figure 3.2: Flight trajectories for BESS '93, '94 and '95.

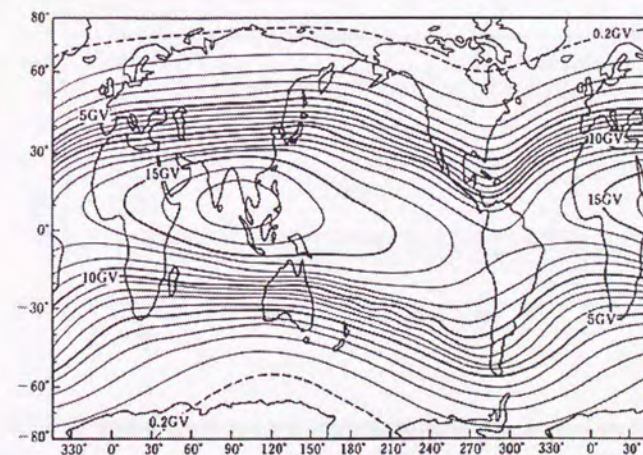


Figure 3.3: The contour map for geomagnetic cutoff rigidity.



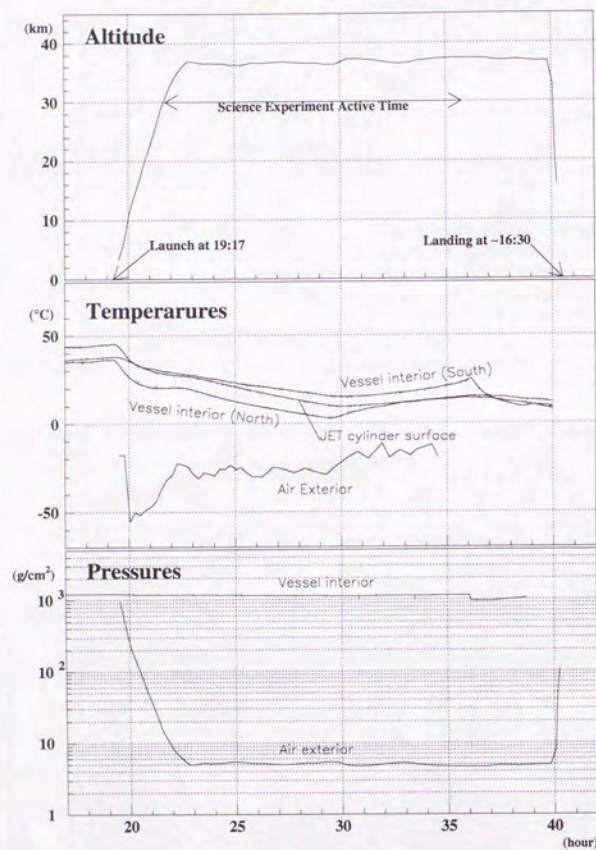


Figure 3.4: House-keeping data on altitude, temperatures and pressures in BESS '93 flight.

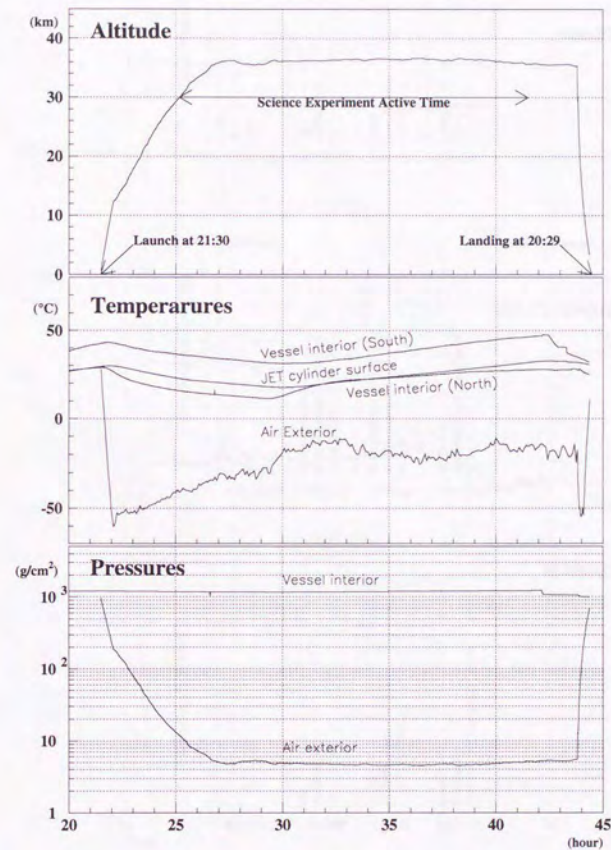


Figure 3.5: House-keeping data on altitude, temperatures and pressures in BESS '94 flight.



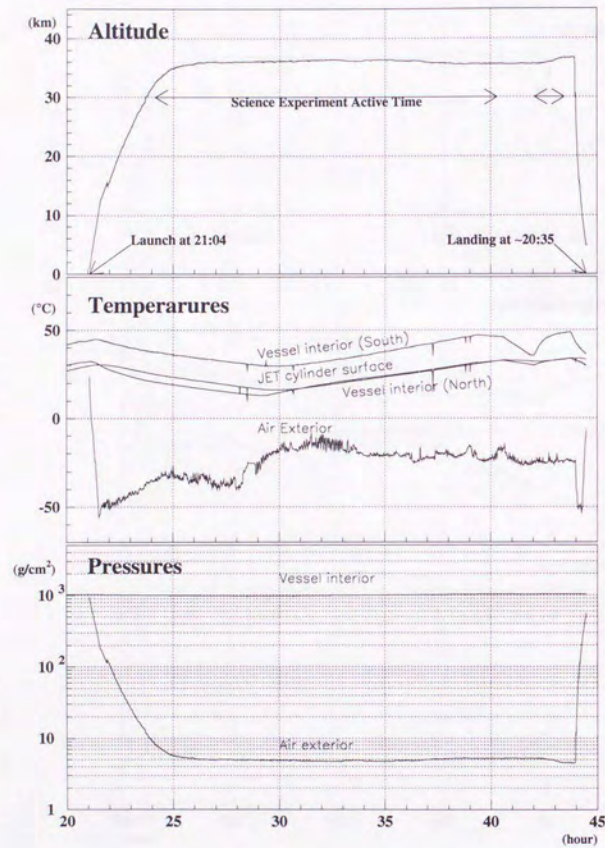
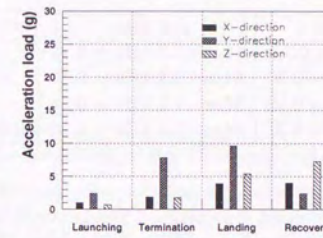
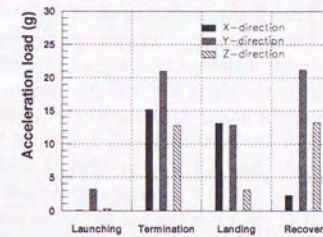


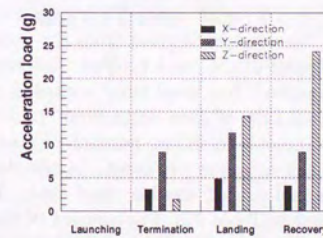
Figure 3.6: House-keeping data on altitude, temperatures and pressures in BESS '95 flight.



(a) '93 flight



(b) '94 flight



(c) '95 flight

Figure 3.7: Acceleration loads in (a) '93, (b) '94 and (c) '95 flights.



Table 3.2: Summary of the dead time.

flight year	data process	fast clear	error	dead time
'93	1.5 ms $\times$ 87 Hz = 0.13	84 $\mu$ s $\times$ 1.7 kHz = 0.14	—	0.27
'94 first half	1.9 ms $\times$ 140 Hz = 0.27	84 $\mu$ s $\times$ 1.3 kHz = 0.11	—	0.38
'94 last half	1.8 ms $\times$ 100 Hz = 0.18	84 $\mu$ s $\times$ 1.5 kHz = 0.13	—	0.31
'95	2.1 ms $\times$ 100 Hz = 0.21	84 $\mu$ s $\times$ 1.2 kHz = 0.10	0.08	0.39

Though the instrument experienced gravitational accelerations over 20  $g$  at the moment of launching, termination, landing and during recovery (Figure 3.7), the detectors inside the pressure vessel were completely safe and no significant damage was observed.

The BESS instrument was activated for 14 hours in 1993 flight, for 16 hours in 1994 flight and for 17.5 hours in 1995 flight, including short run for trigger tuning, actual data acquisition run, and calibration run. Trigger parameters (T0 sampling rate and TT thresholds) were carefully adjusted to achieve the desired trigger rate, based on the trigger rate obtained in the short test run just before the level flight. The actual trigger rate derived from the scaler data was 87 Hz in 1993 flight, 140 Hz in the first half of 1994 flight, 100 Hz in the second half, and 100 Hz in 1995 flight, while the T0 coincidence rate was 2.4 kHz in 1993, 2.3 kHz in 1994 and 2.1 kHz in 1995. A calibration run of 5 to 10 minutes was carried out every hour to re-adjust the thresholds for FADC data suppression as low as possible, while the pedestal value of FADC outputs varied depending on temperature. During the data acquisition run of 11.8 hours (1993 flight), 11.1 hours (1994 flight) and 12.3 hours (1995 flight),  $3.6 \times 10^6$  events,  $4.7 \times 10^6$  events and  $4.6 \times 10^6$  events were recorded, while  $1.01 \times 10^8$ ,  $9.35 \times 10^7$  and  $9.35 \times 10^7$  of cosmic rays made coincidence at the T0 level, and of which  $7.34 \times 10^7$ ,  $6.14 \times 10^7$  and  $5.73 \times 10^7$  made T0 trigger, respectively. The 'live time' or effective exposure time can be derived from the ratio of T0 trigger to T0 coincidence, 73.0%, 65.7% and 61.4%, as  $3.1 \times 10^4$  sec (8.6 hours),  $2.6 \times 10^4$  sec (7.3 hours) and  $2.7 \times 10^4$  sec (7.6 hours). The 'dead time' consisted of decision time before fast clear (80  $\mu$ s) and process time of data acquisition (1.5 – 2.0 ms). These depend on the status of the instrument, including number of read-out channel of electronics, the trigger rate and the data size per event. In addition, in '95 flight, error due to one bad FADC channel caused another dead time. The 'dead time' of the three flights are summarized in Table 3.2. The amount of the data recorded during the experiments were 4.8 Gbytes in '93 flight, 7.0 Gbytes in '94 flight and 7.8 Gbytes in '95 flight.

Table 3.3 summarizes the T0 trigger, and Table 3.4 and 3.4 summarize the Master trigger (MT).

Table 3.3: The conditions of the T0 trigger and the trigger rates.

Mode	Top		Bottom		Ext	Sample Rate	Accept Rate	T0 Trigger
	Low	High	Low	High				
'93 Flight								
T0-Low	1	x	1	x	x	1/1	2.3 kHz	2.3 kHz
T0-High	x	1	x	1	x	1/1	660 Hz	660 Hz
T0-gamma	0	0	1	x	x	1/256	19 kHz	73 Hz
T0-external	x	x	x	x	1	1/1	0 Hz	0 Hz
'94 Flight First Half								
T0-Low	1	x	1	x	x	1/1	2.3 kHz	2.3 kHz
T0-High	x	1	x	1	x	1/1	340 Hz	340 Hz
T0-gamma	0	0	1	x	x	1/256	18 kHz	70 Hz
T0-external	x	x	x	x	1	1/1	0 Hz	0 Hz
'94 Flight Second Half								
T0-Low	1	x	1	x	x	1/1	2.3 kHz	2.3 kHz
T0-High	x	1	x	1	x	1/1	320 Hz	320 Hz
T0-gamma	0	0	1	x	x	1/256	18 kHz	70 Hz
T0-external	x	x	x	x	1	1/1	0 Hz	0 Hz
'95 Flight								
T0-Low	1	x	1	x	x	1/1	2.0 kHz	2.0 kHz
T0-High	x	1	x	1	x	1/1	250 Hz	250 Hz
T0-gamma	0	0	1	x	x	1/256	19 kHz	72 Hz
T0-external	x	x	x	x	1	1/1	0 Hz	0 Hz

- 1 : Signal should be asserted.  
 0 : Signal should not be asserted.  
 x : Signal is not concerned.



Table 3.4: The settings of the Master Trigger and the trigger rate ('93 and '94-1).

MT Mode		T0 Mode Mask	Sampling	Accepted	Triggered
'93 Flight					
Biased	$\bar{p}$ -clear	1 0 0 0	1/1	17 Hz	12 Hz
	$\bar{p}$ -dirty	1 0 0 0	1/1	25 Hz	18 Hz
	$\bar{H}e$ -clear	0 1 0 0	1/1	3.6 Hz	2.6 Hz
	$\bar{H}e$ -dirty	0 1 0 0	1/1	8.0 Hz	5.9 Hz
	Missing-a-hit	1 1 0 0	1/1	3.9 Hz	2.8 Hz
	Multi-clear	1 1 0 0	1/1	22 Hz	16 Hz
	Multi-dirty	1 1 0 0	1/1	11 Hz	8 Hz
	Gamma	0 0 1 0	1/1	0.8 Hz	0.6 Hz
Unbiased	T0-Low	1 0 0 0	1/140	2.3 kHz	12 Hz
	T0-High	0 1 0 0	1/40	660 Hz	12 Hz
	T0-Gamma	0 0 1 0	1/100	73 Hz	0.5 Hz
	T0-External	0 0 0 1	1/1	—	—
Total				2.4 kHz	87 Hz
'94 Flight First Half					
Biased	$\bar{p}$ -clear	1 0 0 0	1/1	61 Hz	38 Hz
	$\bar{p}$ -dirty	1 0 0 0	1/1	26 Hz	16 Hz
	$\bar{H}e$ -clear	0 1 0 0	1/1	22 Hz	14 Hz
	$\bar{H}e$ -dirty	0 1 0 0	1/1	17 Hz	10 Hz
	Missing-a-hit	1 1 0 0	1/1	19 Hz	12 Hz
	Multi-clear	1 1 0 0	1/1	62 Hz	39 Hz
	Undefined	1 1 0 0	1/1	—	—
	Gamma	0 0 1 0	1/1	1.4 Hz	0.9 Hz
Unbiased	T0-Low	1 0 0 0	1/60	2.3 kHz	23 Hz
	T0-High	0 1 0 0	1/15	340 Hz	14 Hz
	T0-Gamma	0 0 1 0	1/100	70 Hz	0.4 Hz
	T0-External	0 0 0 1	1/1	—	—
Total				2.3 kHz	140 Hz

Table 3.5: The settings of the Master Trigger and the trigger rate ('94-2 and '95).

MT Mode		T0 Mode Mask	Sampling	Accepted	Triggered
'94 Flight Second Half					
Biased	$\bar{p}$ -clear	1 0 0 0	1/1	51 Hz	35 Hz
	$\bar{p}$ -dirty	1 0 0 0	1/1	23 Hz	16 Hz
	$\bar{H}e$ -clear	0 1 0 0	1/1	23 Hz	16 Hz
	$\bar{H}e$ -dirty	0 1 0 0	1/1	16 Hz	11 Hz
	Missing-a-hit	1 1 0 0	1/1	25 Hz	17 Hz
	Multi-clear	1 1 0 0	1/2	55 Hz	19 Hz
	Undefined	1 1 0 0	—	—	—
	Gamma	0 0 1 0	1/1	1.5 Hz	1.0 Hz
Unbiased	T0-Low	1 0 0 0	1/120	2.3 kHz	13 Hz
	T0-High	0 1 0 0	1/30	320 Hz	7 Hz
	T0-Gamma	0 0 1 0	1/100	70 Hz	0.5 Hz
	T0-External	0 0 0 1	1/1	—	—
Total				2.3 kHz	100 Hz
'95 Flight					
Biased	$\bar{p}$ -clear	1 0 0 0	1/1	57 Hz	35 Hz
	$\bar{p}$ -dirty	1 0 0 0	1/1	42 Hz	26 Hz
	$\bar{H}e$ -clear	0 1 0 0	1/1	18 Hz	11 Hz
	$\bar{H}e$ -dirty	0 1 0 0	1/1	17 Hz	10 Hz
	Missing-a-hit	1 1 0 0	1/100	14 Hz	0.08 Hz
	Multi-clear	1 1 0 0	1/3	69 Hz	14 Hz
	Undefined	1 1 0 0	—	—	—
	Gamma	0 0 1 0	1/10	1.4 Hz	0.09 Hz
Unbiased	T0-Low	1 0 0 0	1/90	2.0 kHz	14 Hz
	T0-High	0 1 0 0	1/20	250 Hz	7.5 Hz
	T0-Gamma	0 0 1 0	1/256	72 Hz	0.2 Hz
	T0-External	0 0 0 1	1/1	—	—
Total				2.1 kHz	100 Hz



## Chapter 4

### Data Analysis

#### 4.1 Flight Data Sample

As already mentioned in Chapter 3, the data acquisition was stopped every hour to take some calibration data, yielding 12 data acquisition runs in each flight of 1993 and 1994 and 15 runs in 1995 flight, respectively.

In Table 4.1 and 4.1 are summarized the number of events in each run, where T0 is the number of the T0 triggers at the first level, Master is the number of the MT trigger, *i.e.*, the number of the events the data acquisition system collected. The right half of the table shows the trigger modes of the recorded data, each of which corresponds to the Master Trigger mode (see also Table 3.4 and 3.5).

The first step of the data processing was to decompress the raw flight data which contain event data, house-keeping data, command and message data. To analyze the data, we extract properties of hits in detector components and trigger conditions from event data. The event frames had different sizes varying from several hundred to three kilo bytes depending on the number of hits in detectors, and then variable length data format is needed. The ZEBRA [56] system of CERN program library was employed to store the properties extracted from the raw flight data, because it has dynamic data structuring capability with tree structures of data storage units (called 'bank') and linkage of these structures. The HEPDB [57] database management package of CERN program library, which is available in the ZEBRA system, was employed to store the geometries of the detector components, the read-out channel assignment tables and the calibration parameters.

The off-line calibrations were made on each run to derive temperature-dependent or pressure-dependent parameters, for instance, timing offsets in TOF measurement and drift velocity in the drift chambers.

Primary calibrations were performed to obtain pedestals and gain factors. After initial calibrations, pattern recognition was performed using the hits of JET chamber to find tracks of the incident particles and track information banks are formed. The hits of IDC, ODC and TOF (and Čerenkov) made by the particle were acquired by extrapolating the fitted trajectory of the track and then linked to the track information bank. Thus, all informations of the hits which an incident particle induced on the detectors were to be retrieved by accessing the track information



Table 4.1: Summary of BESS flight data ('93 and '94).

run #	time ( $\times 10^3$ s)	T0 ( $\times 10^6$ )	Master ( $\times 10^5$ )	Record ( $\times 10^5$ )	T0 Low ( $\times 10^4$ )	T0 High ( $\times 10^4$ )	MT $\bar{p}$ ( $\times 10^4$ )	MT He ( $\times 10^4$ )
93-13	3.29	5.82	2.89	2.84	4.09	4.19	10.14	2.87
14	2.80	4.95	2.45	2.41	3.49	3.57	8.74	2.49
15	3.80	6.70	3.31	3.25	4.71	4.81	11.75	3.29
16	2.90	5.11	2.51	2.48	3.60	3.66	8.88	2.46
17	3.54	6.25	2.98	2.94	4.40	4.46	10.45	2.83
18	4.21	7.38	3.50	3.44	5.22	5.24	12.12	3.21
19	4.06	6.93	3.44	3.39	4.89	4.90	11.21	2.77
20	4.58	7.73	3.90	3.83	5.47	5.48	13.65	3.65
21	3.46	5.89	3.09	3.04	4.15	4.14	10.83	3.02
22	2.16	3.67	1.93	1.90	2.59	2.55	6.73	1.93
23	3.53	6.04	3.20	3.15	4.24	4.18	11.15	3.22
24	4.06	6.89	3.74	3.68	4.85	4.74	13.54	3.95
93-total	42.39	73.35	36.95	36.35	51.71	51.92	129.19	35.68
94-6	3.81	5.51	5.37	5.26	9.29	5.41	21.05	8.94
7	3.21	4.66	4.54	4.45	7.85	4.64	17.57	7.68
8	3.04	4.42	4.31	4.22	7.46	4.38	16.57	7.24
9	3.32	4.72	4.62	4.52	7.95	4.70	17.63	7.84
10	3.74	5.41	5.23	5.11	9.12	5.39	19.52	8.93
13	2.16	3.16	3.01	2.93	5.31	3.13	10.82	5.26
15	3.11	4.98	3.24	3.18	4.12	2.37	16.11	8.17
16	5.44	8.76	5.54	5.45	7.24	4.09	27.28	14.27
17	3.14	5.00	3.14	3.08	4.12	2.30	15.32	8.16
18	2.34	3.80	2.36	2.32	3.13	1.71	11.55	6.12
19	3.50	5.67	3.52	3.45	4.70	2.53	17.15	9.17
20	3.27	5.33	3.30	3.24	4.41	2.35	16.11	8.57
94-total	40.08	61.43	48.17	47.21	74.72	43.01	206.68	100.36

Table 4.2: Summary of BESS flight data ('95).

run #	time ( $\times 10^3$ s)	T0 ( $\times 10^6$ )	Master ( $\times 10^5$ )	Record ( $\times 10^5$ )	T0 L ( $\times 10^4$ )	T0 H ( $\times 10^4$ )	MT $\bar{p}$ ( $\times 10^4$ )	MT He ( $\times 10^4$ )
95-7	3.19	4.41	3.59	3.57	4.87	2.62	21.15	7.12
8	3.41	4.52	3.68	3.66	4.99	2.73	21.67	7.39
9	2.56	3.12	2.55	2.53	3.43	1.92	14.91	5.15
10	2.56	3.10	2.50	2.47	3.41	1.92	14.47	5.01
11	3.66	4.82	3.89	3.87	5.33	3.02	22.56	7.91
12	3.41	4.15	3.35	3.33	4.57	2.59	19.41	6.90
13	3.11	3.82	3.07	3.05	4.20	2.36	17.75	6.31
14	0.47	0.61	0.49	0.49	0.68	0.37	2.85	0.99
15	3.60	4.77	3.81	3.79	5.26	2.86	22.13	7.76
16	3.20	4.39	3.49	3.47	4.85	2.60	20.25	7.07
17	3.32	4.42	3.53	3.51	4.88	2.57	20.48	7.14
18	3.34	3.94	3.13	3.08	4.35	2.24	17.96	6.22
19	3.21	3.89	3.07	3.00	4.29	2.15	17.50	6.00
20	2.88	4.08	3.21	3.17	4.49	2.21	18.57	6.31
21	2.35	3.31	2.60	2.56	3.63	1.78	15.07	5.13
95-total	44.28	57.34	45.97	45.56	63.24	33.96	266.74	92.41



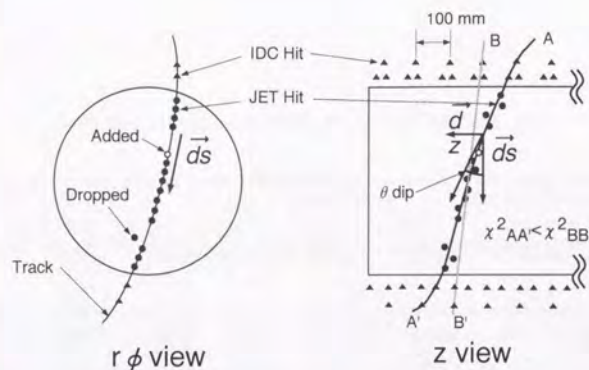


Figure 4.1: Method of the rigidity measurement.

bank, and the properties of the particle were to be obtained.

Detailed calibrations were performed using the track information retrieved as above. In order to reduce the time consumption or the process, the information of the track and associated hits were stored into data summary files, which are flat files consisting of fixed length records. The results of the calibrations were put into the database, and pattern recognition and track fitting were performed in the ZEBRA-based system again. The final data summary files were obtained from the re-created track information banks and were used for the further analysis.

In the following, we analyze and obtain results using only '95 flight data.

## 4.2 Event Reconstruction

### 4.2.1 Track Reconstruction

The rigidity of a particle was determined by the JET and IDC drift chambers. First the transverse rigidity ( $R_t$ ), *i.e.* the rigidity component perpendicular to the magnetic field direction, was determined by circular fitting in the  $r\phi$ -plane (Fig. 4.1).

In order to select the hits induced by the particle in the trajectory fitting, the following algorithm was employed.

1. Select 'good' hits, which are defined as hits with enough charge and width.
2. Find trajectories by connecting the 'good' hits in JET chamber and perform circular fitting.

### 4.2. EVENT RECONSTRUCTION

3. Extrapolate each of the trajectories to IDCs to find 'good' IDC hits near the trajectory, they are associated to the track.
4. Perform trajectory fitting again using all hit points in the JET and IDCs which are associated to the track. We used "Karimäki method" [58] for the fitting algorithm at this stage.
5. Scan all of 'good' hits in JET chamber and check if they are well close to the track, *i.e.*, within the distance 5 times of the position resolution,  $5\sigma$ . Only the hits checked here are used in the following processes.
6. Repeat step 4) and 5) twice.

The resultant  $R_t$  should be then corrected for non-uniformity of the magnetic field, which varies up to 10%. Monte Carlo calculations with the computed magnetic field indicates that the correction factor to the rigidity of various trajectories, expressed as a function of the track position, path length, and mean strength of  $B$  field, is able to obtain the corrected rigidity which is within an relative accuracy of 0.2 % from the actual one.

To obtain the total rigidity ( $R$ ) from  $R_t$ , we find the dip angle  $\theta_{\text{dip}}$ , which is defined as an angle between the  $r\phi$ -component ( $\vec{ds}$ ) and the  $z$ -component ( $\vec{dz}$ ) of  $R$ , by fitting in the  $yz$ -plane (Fig. 4.1). We use a similar iterative procedure as used in the  $r\phi$  fitting to eliminate irrelevant hits. The selected hits are fitted to a sine-curve. Since the IDCs provide the only  $z$  positions modulo 100 mm, all possible combinations of the IDC hits are examined. The resultant  $\theta_{\text{dip}}$  are obtained from the combination having minimum  $\chi^2$  value in the fitting.

Finally rigidity  $R$  are derived from  $R_t$  and  $\theta_{\text{dip}}$  as;

$$R = \frac{R_t}{\cos \theta_{\text{dip}}}.$$

### 4.2.2 Time-of-Flight Measurement

Figure 4.2 illustrates the measurement scheme of time-of-flight (TOF). The TOF between top and bottom TOF hodoscopes is calculated for each track by the following procedure. We use here the suffix 'elec' for the PMT on the side of the electronics and the suffix 'tank' for the PMT on the side of the helium reservoir tank.

1. Correct a timing walk using the charge information for each PMT. We use following formulae:

$$\hat{t}_{\text{elec}} = t_{\text{elec}} - a_i / \sqrt{q_{\text{elec}}},$$

and

$$\hat{t}_{\text{tank}} = t_{\text{tank}} - a_i / \sqrt{q_{\text{tank}}},$$

where  $t_{\text{elec,tank}}$  is the measured timing,  $\hat{t}_{\text{elec,tank}}$  the timing after the correction,  $q$  the measured charge of the PMT, and  $a_i$  is the correction parameter of the  $i$ th PMT. Parameter  $a_i$  was determined by the beam test.



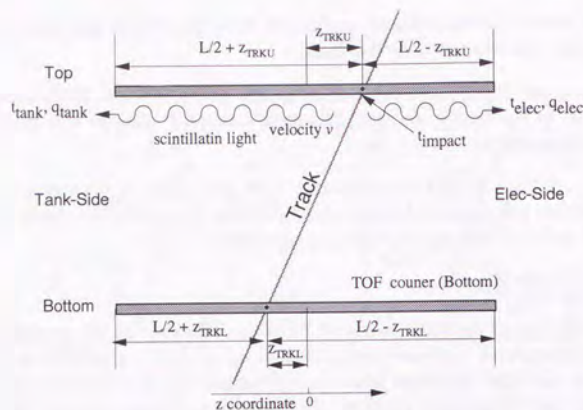


Figure 4.2: Method of the TOF measurement.

2. Derive the timing that the particle passed through the counter ( $t_{\text{impact}}$ ) from the corrected timing of each PMT. Using the  $z$ -impact point ( $z_{\text{trku}}, z_{\text{trkl}}$ ) of the particle which is calculated by extrapolating the combined track,  $t_{\text{impact}}$  is obtained for elec-side as;

$$t_{\text{impact.elec}} = \hat{t}_{\text{elec}} - \frac{\frac{L}{2} - z_{\text{TRKU,TRKL}}}{v_{\text{eff}}} - t_{\text{offset}}(z_{\text{TRKU,TRKL}}),$$

and for tank-side as,

$$t_{\text{impact.tank}} = \hat{t}_{\text{tank}} - \frac{\frac{L}{2} + z_{\text{TRKU,TRKL}}}{v_{\text{eff}}} - t_{\text{offset}}(z_{\text{TRKU,TRKL}}),$$

where  $v_{\text{eff}}$  is the effective light velocity in the counter and  $L$  is the length of the counter including light guides. The second term is the propagation time for the scintillation light to reach to each PMT. The last term  $t_{\text{offset}}(z)$  is the timing offset as a function of the  $z$  position. This is introduced to correct the effective velocity variation depending on the  $z$  position and is determined by calibration for each counter. The averaged impact time of the counter is then obtained as;

$$t_{\text{impact}} = \left( \frac{t_{\text{impact.elec}}}{\sigma_{\text{elec}}(z)^2} + \frac{t_{\text{impact.tank}}}{\sigma_{\text{tank}}(z)^2} \right) / \left( \frac{1}{\sigma_{\text{elec}}(z)^2} + \frac{1}{\sigma_{\text{tank}}(z)^2} \right),$$

where  $\sigma(z)$  is the timing resolution of the each PMT as a function of  $z$ .

3. The value  $t_{\text{impact}}$  is individually calculated for both top and bottom counters, and then the TOF is obtained as the time difference between them.

The  $\beta \equiv v/c$  of the particle can be determined from the TOF and the path length derived from the trajectory.

### 4.2.3 $dE/dx$ Measurement

The energy deposit of a particle,  $dE/dx$ , in a scintillator is derived from the pulse size of the PMT output, which is measured by ADC as a charge, by following steps:

1. Subtract the pedestal value from the ADC count and correct it for the gain of PMT and ADC.

$$q = (\text{count} - \text{pedestal}) / \text{gain}$$

The gain is determined by the calibration to normalize the energy deposit  $dE/dx$  of minimum ionizing particle to be 1.

2. Correct the  $z$  dependence of the signal amplitude due to the attenuation of scintillation light in the scintillator using the  $z$ -impact position of the extrapolated track. The detailed study shows that the measured charge  $q_{\text{measured}}$  has the  $z$  dependence as follows:

$$q_{\text{measured}} \simeq (a + be^{cz})dE,$$

where  $a, b$  and  $c$  are parameters that should be determined by the calibration, and  $dE$  is the deposited energy.

3. Average the energy deposit  $dE$  derived from the PMT signals of two ends both at top and bottom counters.
4. Divide the average energy deposit by the path length in the scintillator through which the particle passed. This gives  $dE/dx$  in the TOF counters.

In '95 flight data,  $dE/dx$  in the JET chamber is also calibrated and utilized following analysis. Because the JET chamber is filled with the slow gas, it was found that space charge effect degrades the  $dE/dx$  resolution, particularly in the high charge region. After an exhaustive study of the effect, the correction method for saturated charge is obtained as follows:

1. Subtract the pedestal value from the FADC charge and normalize it in each channel.
2. The degree of saturation greatly depends on the inclination of the track towards the  $z$ -direction ( $\theta_z$ ) and also slightly depends on the inclination of the track in the  $r\phi$ -plane ( $\theta_{r\phi}$ ). Using pure helium and proton samples, charge is corrected for ( $\theta_z$ ) by fitting to the data as a two-dimensional function, and then corrected for ( $\theta_{r\phi}$ ), in each wire.
3. The correction for drift length is applied to obtain  $dE$  because of loss of charge by the diffusion during the drift.



4. Divide the  $dE$  by the path length for the wire in the gas through which the particle passed. This gives  $dE/dx$  for one wire.
5. In order to remove Landau tail or  $\delta$  ray effects, truncated mean method is applied in which lower 10 % and higher 50 % of measured  $dE/dx$  values are removed and the rest are used to calculate the mean  $dE/dx$ .

### 4.3 Simulation

Monte Carlo (M.C.) simulations were performed in the analysis for the following purposes:

- The behavior of antiprotons in the matter is different from those of protons primarily due to annihilation process. Some portion of antiprotons will be lost through annihilation both in the atmosphere and in the instrument. We use the Monte Carlo simulation to know this effect for protons and antiprotons both in the atmosphere and in the instrument.
- In identifying antiprotons, we rely mainly upon three key properties of the event; rigidity,  $\beta(\equiv v/c)$ ,  $dE/dx$ . Due to interactions or accidental hits, some of them might be far from the expected value. In such cases, other particle species such as electrons might mimic antiprotons. These faking processes and their probability should be investigated by the Monte Carlo simulation as well as by the real data.
- Although the solenoid coil produced an almost uniform magnetic field, we should take account of the slight non-uniformity in order to make a precise rigidity measurement. Simulating the magnetic field and tracing the path of the incident particles by small steps, we can find the difference between the true rigidity and the measured rigidity determined by the curvature of the circular fit.

We have built a simulation model of the BESS instrument based on the GEANT/GHEISHA [59] code, assembling the detector components, support frames and others which are defined with the actual dimensions and materials. The material distribution in the instrument have been well reproduced in the model. Figure 4.3 shows the view of the simulated BESS instrument.

Before performing Monte Carlo simulation, we checked the cross sections for proton to nucleus and for antiproton to nucleus in GHEISHA code and found that the former is almost consistent with the experimental data, but the latter is not. Figure 4.4 shows the inelastic and elastic cross sections for antiproton to Carbon and Aluminum. The histograms which are given from GHEISHA and FLUKA codes, have different values from the experimental data [60, 61, 62, 63, 64, 65, 66]. We fitted these data by energy dependent functions and put them in our Monte Carlo simulation code.

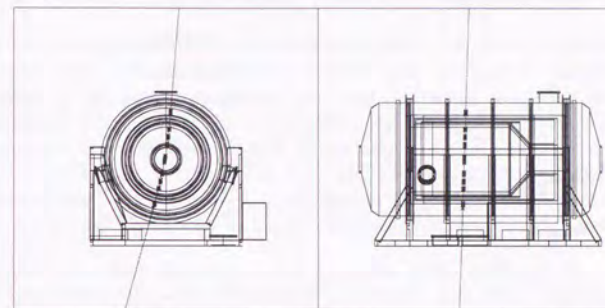


Figure 4.3: Simulated BESS detector.

In the analysis using the simulated events, we extracted the physics informations from the simulated detectors. Since the signals generated by the detector components include no measurement errors and statistical fluctuations, we smeared those signals with the detector resolutions to reproduce the measured detector performance. We adjusted following parameters to reproduce the detector responses:

- Resolution of the position measurement in JET chamber and IDC.
- Efficiency of detecting hits by JET chamber.
- Number of photo-electrons in each PMT for minimum ionizing particles.
- TOF counter resolution.

Although the major features of the detector responses could be well reproduced by tuning these parameters, some differences still remained and could affected the various selections as follows. The effects of them should be considered in the use of the efficiencies.



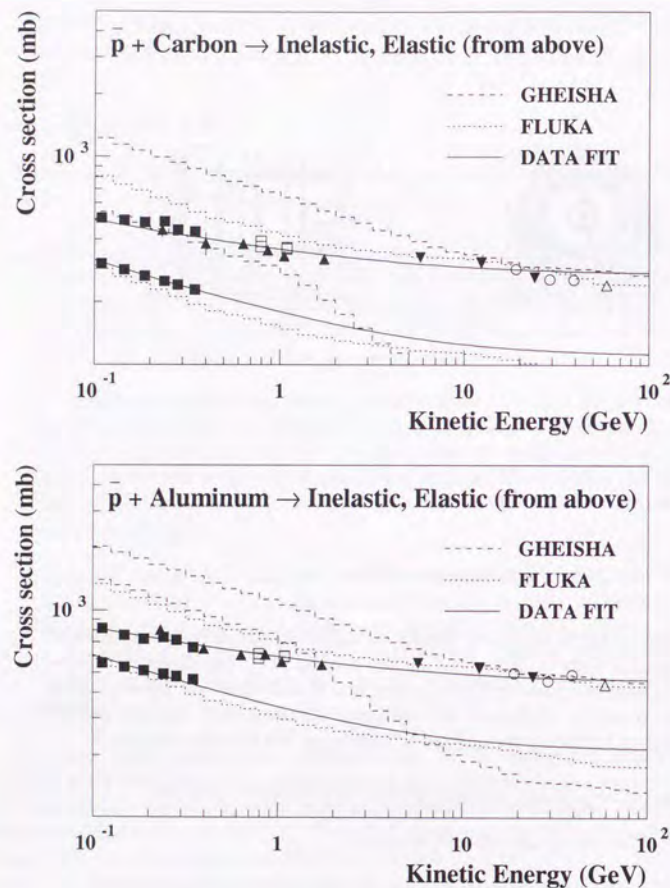


Figure 4.4: Inelastic and Elastic cross sections for antiproton to carbon and aluminum. The histograms are from GHEISHA and FLUKA code and the data points are from Nakamura *et al.*[60] (filled squares); Kuzichev *et al.*[61] (filled triangles); Gorin *et al.*[62] (inverted triangles); Allaby *et al.*[63] (open circles); Afonas'ev *et al.*[64, 65] (open squares) and Carroll *et al.*[66] (open triangles). The curves are fitted with these data points.

- In finding tracks in the JET chamber, the analysis program for the Monte Carlo simulation used the information provided by the GEANT code. This means that the efficiency of track finding was 100% in the Monte Carlo simulation. On the other hand, the analysis program for the real data searched for tracks testing the possible combinations of hits in JET chamber. Some tracks may have not been recognized, causing a lower track finding efficiency.
- There were extra hits in the real JET chamber that did not associate to any track. Most likely such hits were "noise hits" induced by electro-magnetic noises or by electron emissions from the HV wires near the cylinder wall. Some of them were "after pulses" following signal pulses, which could have been produced by the diffusion of the electrons. Others could be the hits produced by the particle whose track was not recognized. Such the extra hits from these origins cannot be produced in the Monte Carlo simulation and hence caused a difference in the selection efficiency.
- There were some electric-induced crosstalks in the IDC and ODC read-out, which affected the cell hit pattern of the IDC and ODC, causing some inefficiency of the TT hit pattern selection. This effect was not taken in the simulation.
- We used the primary kinematics with only one particle in the simulation, while, in the observed data, there were multi-track events, which contained two ( or more ) unrelated tracks, the extrapolation of which did not intersect each other. The efficiency of the single track selection must have been affected by multi-track events.

## 4.4 Event Selections

The event selections were applied in order to obtain fiducial events with 'good' measurements, excluding the events with multi-track, large scatterings or accidental hits, which probably do not provide correct particle properties. The selection criteria are described in the following sections.

### 4.4.1 Selections for Good Single Track

The T0 trigger requires only the coincidence of the hits at the top and the bottom scintillation counters, and the MT trigger requires the hits in IDCs and ODCs. Thus, there are events in which the incident particle did not pass through JET chamber, or left too few hits in it to reconstruct the track with a desired accuracy. We exclude such events and use events with a long enough track in the analysis, which corresponds to a reduction of the geometrical acceptance of the instrument.

There also events which contain multi-tracks or too many hits in the detectors. A shower-like event with too many hits makes it difficult to reconstruct the tracks, and a multi-track event is not fiducial in the TOF measurement, for more than one



track might have passed through the same scintillator, or the incident particle might have been scattered and changed its direction and energy.

Following cuts were applied to obtain reconstructible events with a good single track which passed through the fiducial region of JET chamber.

1.  $N_{\text{TOFU}} = 1$   $N_{\text{TOFL}} = 1$   
There should be one and only one hit in the scintillation counters both at the top and at the bottom.
2.  $N_{\text{longtrack}} = 1$   
The number of tracks with 10 or more hits found in JET chamber should be one and only one.
3.  $N_{\text{expect}} \geq 16$   
The number of hits in JET chamber expected from the trajectory  $N_{\text{expect}}$  is 16 or more. This cut defines the fiducial region of the JET chamber and eliminates the track which scratches the outermost region, where the position measurement is less accurate than the central region due to the distortion of the electric field.
4.  $R_{\text{TOF}}\Delta\phi_{\text{TOFU}} < W_{\text{TOF}}/2 + 10.0\text{mm}$ ,  $R_{\text{TOF}}\Delta\phi_{\text{TOFL}} < W_{\text{TOF}}/2 + 10.0\text{mm}$   
where  $R_{\text{TOF}}$  is the distance from the center of the instrument to the center of a TOF counter,  $R_{\text{TOF}}\Delta\phi$  is the distance in  $\phi$ -direction from the trajectory to the center of the nearest hit TOF counter, and  $W_{\text{TOF}}$  is the width of a TOF counter. In the  $r\phi$ -plane, the extrapolated trajectory should pass through a hit TOF counter with an accuracy of 10mm.

In total 2,636,964 events passed these cuts.

At this stage, we select events by hit-pattern mode of the track-trigger. Events with mode-1 ( $\bar{p}$ -clear), mode-2 ( $\bar{p}$ -dirty) and mode-6 (Multi-clear) are selected, because events with other modes and unbiased events which were rejected by hit-pattern selection might have rather worse qualities of measurements or include too few protons/antiprotons to obtain accurate efficiencies.

In total 2,042,843 events passed this selection.

#### 4.4.2 Track Quality Cut

Following cuts were applied to ensure a quality of the single track.

1.  $N_{\text{cenhit}} \geq 10$   
The number of hits in the central region of JET chamber is 12 or more. This cut eliminates the track which scratches the outermost region, where the position measurement is less accurate than the central region due to the distortion of the electric field.
2.  $N_{\text{extrahit}} \leq 50$   
To exclude multi-track events and noisy events, the number of JET hits not concerned with the track  $N_{\text{extrahit}} \equiv N_{\text{totalhit}} - N_{\text{trackhit}}$  is to be limited.

3.  $N_{\text{trackhit}} - N_{r\phi\text{-fit}} \leq 8$   
As mentioned in Section 4.2.1, not all the JET hits are used in trajectory fitting. If the number of hits used in trajectory fitting  $N_{r\phi\text{-fit}}$  is too small comparing to that of track-associated hits  $N_{\text{trackhit}}$ , the quality of the track information are possibly not good.
4.  $N_{r\phi\text{-fit}} \geq 10$   
The accuracy of the track information depends on the number of hits used in the trajectory fitting.
5.  $N_{z\text{-fit}} \geq 6$   
Since the number of wires to determine  $z$ -position is less than that for  $r\phi$ -position determination, the limit on the number of utilized hits in  $z$ -trajectory fitting is lowered than in  $r\phi$ -fitting.
6.  $\chi_{r\phi}^2 < 5$
7.  $\chi_z^2 < 5$

The goodness of fits can be checked using the reduced chi-square parameters:

$$\chi_{r\phi}^2 \equiv \frac{1}{\sqrt{N_{r\phi\text{-fit}} - 3}} \sqrt{\sum \frac{(\Delta(r\phi)_i)^2}{\sigma_{r\phi,i}^2}},$$

$$\chi_z^2 \equiv \frac{1}{\sqrt{N_{z\text{-fit}} - 2}} \sqrt{\sum \frac{(\Delta(z)_i)^2}{\sigma_{z,i}^2}}.$$

8.  $\min(\Delta(r\phi)_{\text{IDC1i}}, \Delta(r\phi)_{\text{IDC1o}}) < 2.0\text{mm}$ ,  
 $\min(\Delta(r\phi)_{\text{IDC2i}}, \Delta(r\phi)_{\text{IDC2o}}) < 2.0\text{mm}$
9.  $\min(\Delta z_{\text{IDC1i}}/3, \Delta z_{\text{IDC1o}}) < 2.0\text{mm}$ ,  
 $\min(\Delta z_{\text{IDC2i}}/3, \Delta z_{\text{IDC2o}}) < 2.0\text{mm}$

The IDC hits are outermost hits used in trajectory fitting and provide information independent of JET hits. Especially desired precision of the information in  $z$ -fit are obtained only by using IDC hits. We required that at least one good hit in each IDC is close enough to the trajectory. In the data summary files are stored the information of one hit in each layer of IDCs (IDC1i for the inner layer of the upper IDC, or IDC1; IDC2o for the outer layer of the lower IDC, or IDC2, and so on), and at least one hit of the two layers of each IDC is required to be consistent with the trajectory.

Figures 4.5 to 4.9 show the histograms of these track-quality variables together with the cut boundaries. Open histograms are for the events that pass the single-track selection, and the shadowed histograms are for the events that remain after applying the track-quality cut.

In total 1,770,346 events passed these cuts.



### 4.4.3 TOF Quality Cut

The identification of antiprotons is performed by resolving their mass. The accuracy of the mass measurement mainly depends on the accuracy of the TOF measurement, that of rigidity measurement being much higher. The TOF measurement of an incident particle might be disrupted by a coincident hit of another cosmic ray particle or of a radiation from local radio-activated materials.

There is a time difference between the signals from the two ends of a TOF counter due to the propagation time of the scintillation light from impact points to PMTs, which depends on  $z$ -position. The size of the signals are also different due to the attenuation and the loss in reflections, which is also  $z$ -dependent. The timing difference reaches about 6 ns and the amplitude ratio about 3. These features can be used to check consistency with the fitted trajectory obtained from the hits in drift chambers.

1.  $|z_{\text{TRKU}}| < 465 \text{ mm}, |z_{\text{TRKL}}| < 465 \text{ mm}.$

The measurements show odd behavior in small regions at the ends of the TOF counters. This is because some of the incident particles do not pass through the scintillator but through the light guide while the position calculated from the extrapolation of the fitted trajectories are within the scintillator. The conservative fiducial region of the TOF counters are defined as  $|z| < 465 \text{ mm}$ , while the scintillators occupied the region  $|z| < 475 \text{ mm}$ .

2.  $0 \text{ ns} < T_{\text{trig}} < 8 \text{ ns}$

The T0 trigger was generated using the signals of the TOF counters. The trigger timing depended on the signals of the bottom TOF counters and is deducible from the timing and the amplitude of the signals of the bottom TOF counters. Thus, the consistency of the signals of the bottom TOF counters with the actual trigger timing can be examined using the derived trigger timing  $T_{\text{trig}}$ .

3.  $(\Delta z_{\text{TOFU}})^2 + (\Delta z_{\text{TOFL}})^2 < (38 \text{ mm})^2$

The  $z$ -coordinate of a hit in a TOF counter is determined using the time difference;

$$z_{\text{TOF}} = v_{\text{eff}} \cdot \Delta t / 2.$$

where  $v_{\text{eff}}$  is the effective light velocity in the scintillator. If this value is not consistent with the fitted trajectory within the resolution of time measurement, the TOF measurement is wrong due to some accidental hit or the trajectory is wrong.

4.  $(\Delta R_{\text{TOFU}})^2 + (\Delta R_{\text{TOFL}})^2 < (0.3)^2$

The ratio of the amplitude of the signals from the two ends of a counter will be a monotone function of  $z$ . Since the  $z$ -dependence is due to attenuation and loss, the amplitude of a signal read out from an end of a TOF counter will be expressed as:

$$A \simeq \exp(a + bz),$$

where  $a$  and  $b$  are constant peculiar to the read out channel. The ratio of the amplitude from two sides,  $A_L/A_R$ , will then be proportional to  $z$ .

$$R \equiv \log(A_L/A_R) \simeq cz,$$

where  $c$  is constant peculiar to the counter. Actually, the values  $A$  deviate from the exponential function of  $z$ , and so do  $R$  from the linear function:

$$R = f(z) \equiv cz + \varepsilon(z).$$

Even so, the value  $\Delta R \equiv R - f(z)$  will offer a good parameter of consistency between the hit and the trajectory.

Figures 4.10 to 4.12 show the histograms of these variables together with the cut boundaries. Open histograms show the distribution of the events which passed the single track selection, and shadowed are for those after the subsequent track quality cut. Hatched histograms are for the events that passed the TOF quality cut.

In total 1,510,970 events passed these cuts.

The selection criteria are summarized in Table 4.3.

## 4.5 General Data Quality

The quality of the detector performance was checked using the events that passed the event selection. The estimated errors of the rigidity measurement were obtained in the final combined  $r\phi$ -fitting process. Figure 4.13 shows the estimated error of the  $1/R_t$ . The plane histogram is for all the events that passed the selection and the shadowed histogram is for the events with  $N_{r\phi\text{-fit}} > 20$ . Both histograms have a clear peak around  $\Delta(1/R_t) \sim 0.05$ .

According to the following relation,

$$\Delta\left(\frac{1}{R_t}\right) = \frac{\Delta(R_t)}{R_t^2} = \frac{\Delta(R_t)}{R_t} \frac{1}{R_t},$$

the  $\Delta(1/R_t)$  is decomposed into fractional errors of rigidity ( $\Delta(R_t)/R_t$ ) and inverse rigidity ( $1/R_t$ ). The value of 0.005 thus indicates the particles with the transverse rigidity of up to 200 GV are at least  $1\sigma$  away from the particles with the opposite charge. It is noted that no event with  $\Delta(1/R_t)$  of more than 0.031 were observed and therefore all events with rigidity below 1 GV are more than  $30\sigma$  away from the negative rigidity region. Figure 4.14 shows the mean of the  $\Delta(1/R_t)$  distribution as a function of the absolute rigidity for the case that  $N_{r\phi\text{-fit}} > 20$ . Almost constant values are obtained in the entire rigidity range.

The quality of the TOF or  $\beta$  measurement can be checked by utilizing the unbiased trigger sample. In Figure 4.15 the scatter-plots of  $\beta^{-1}$  vs rigidity shows the clear separation of protons, heliums, their isotopes, and pions/muons/electrons.

It is clear that the down-going particles in the positive  $\beta^{-1}$  region are unambiguously separated from the up-going albedo particles in the negative  $\beta^{-1}$  region. Various particles can be clearly identified up to a few GV of the rigidity.



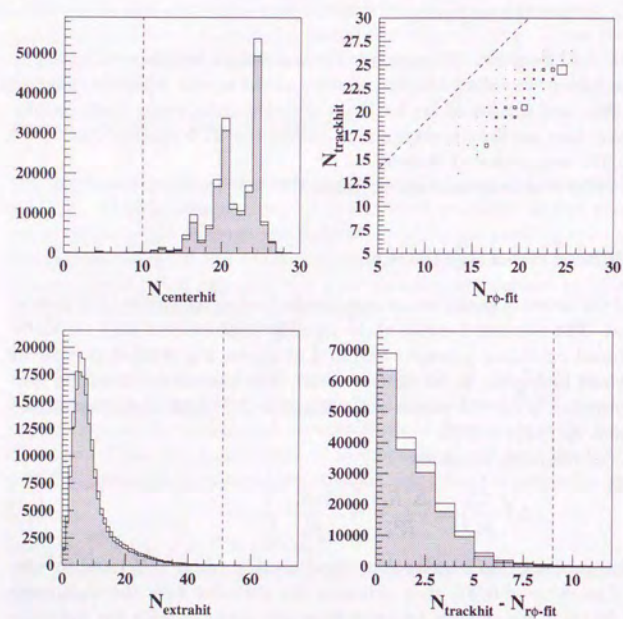


Figure 4.5: Track Quality Cut 1,2,3.

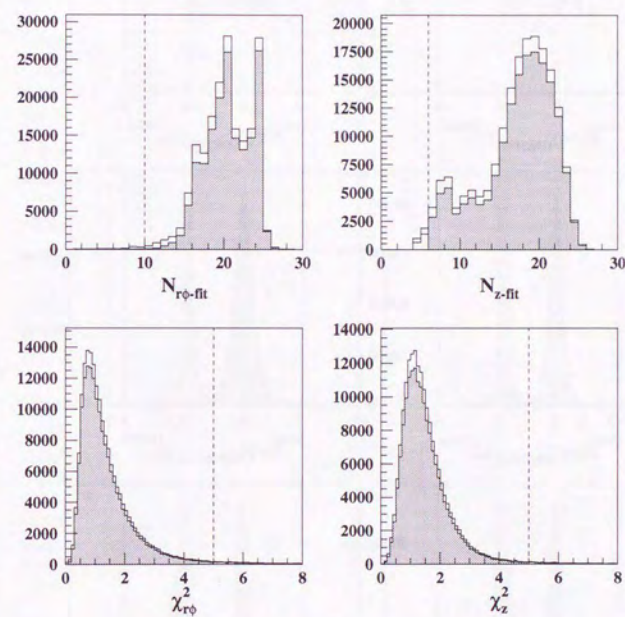


Figure 4.6: Track Quality Cut 4,5,6,7.



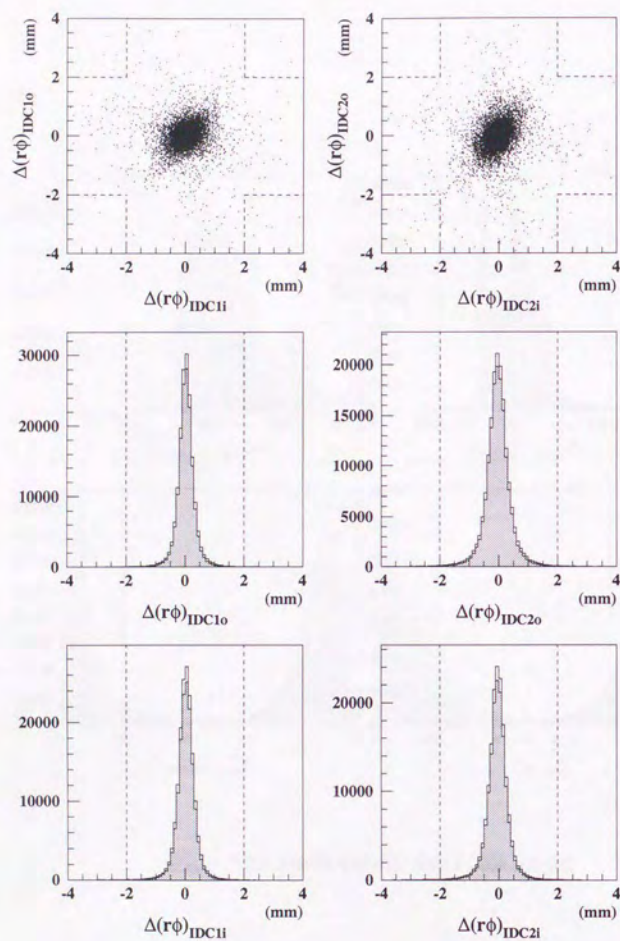


Figure 4.7: Track Quality Cut 8.

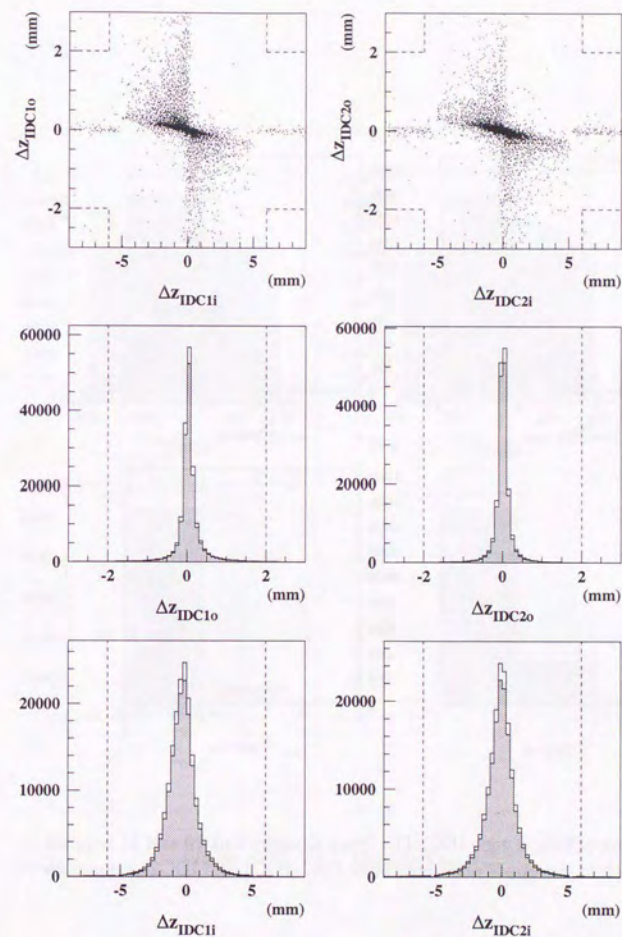


Figure 4.8: Track Quality Cut 9.



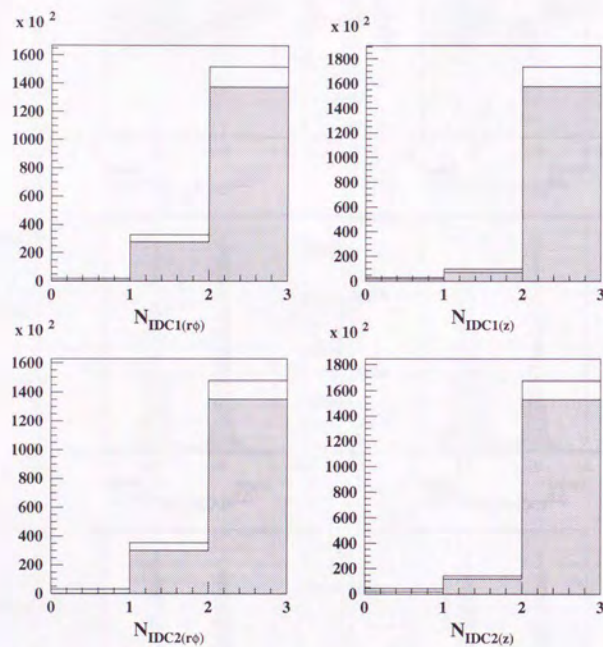


Figure 4.9: Number of hits in each IDC. The Track Quality Cut 10 and 11 requires at least one hit in each of the upper and lower layer IDC (IDC1 and IDC2), respectively.

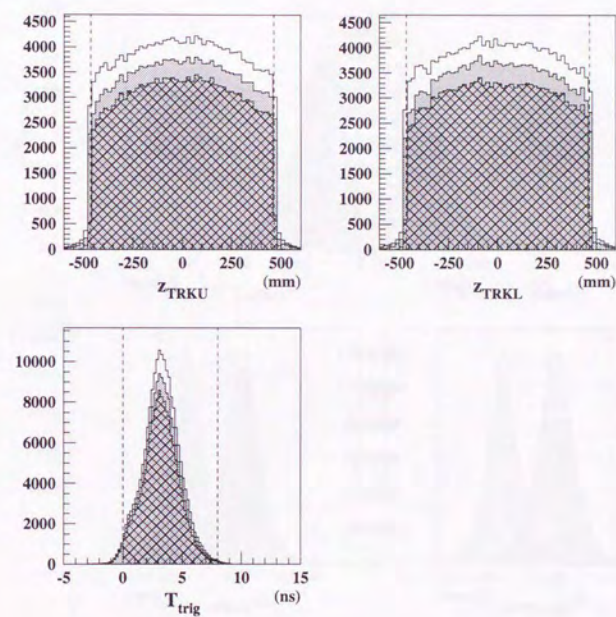


Figure 4.10: TOF Quality Cut 1,2.



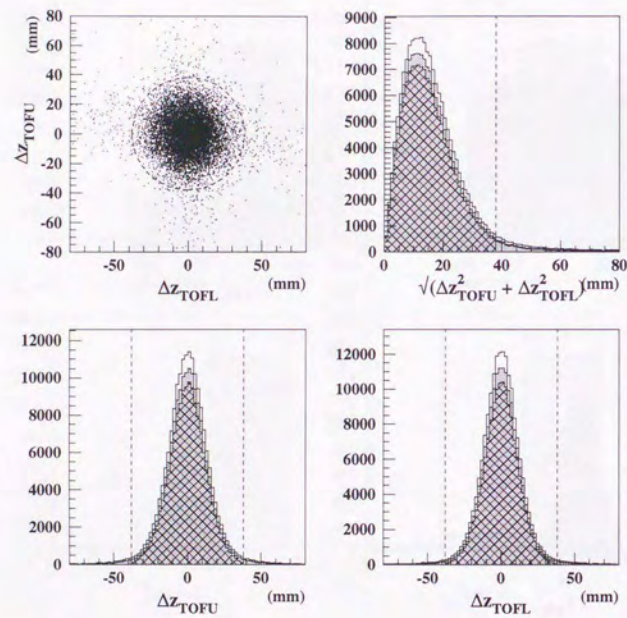


Figure 4.11: TOF Quality Cut 3.

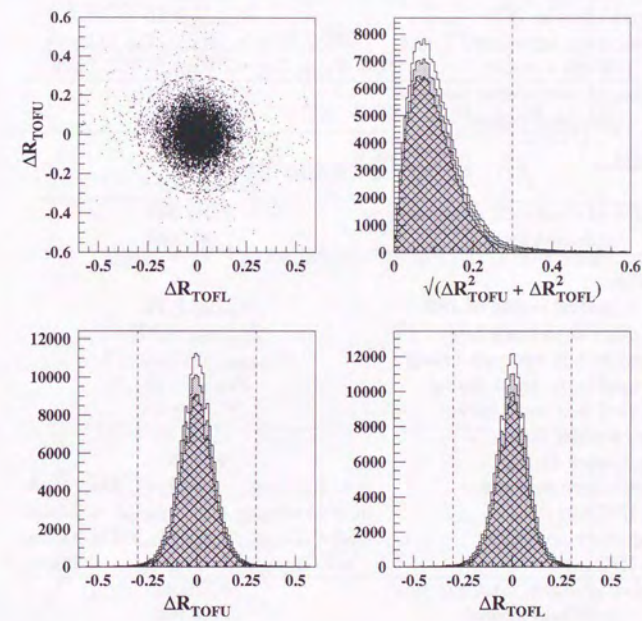
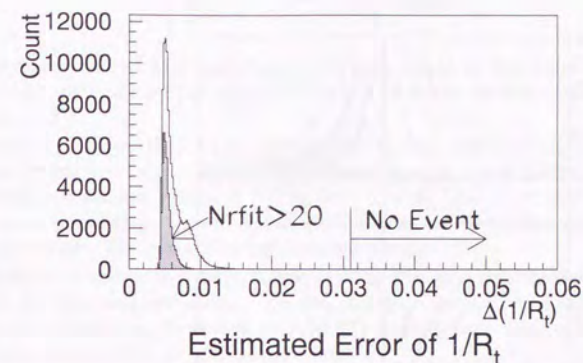
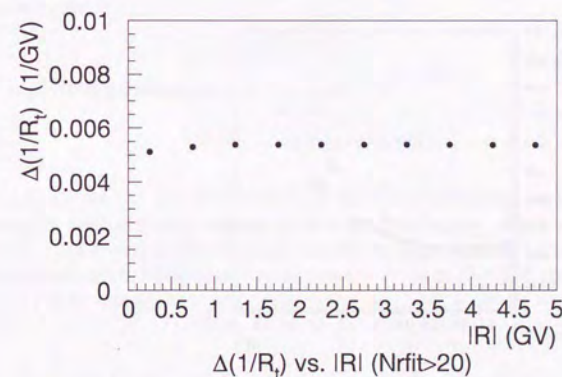


Figure 4.12: TOF Quality Cut 4.

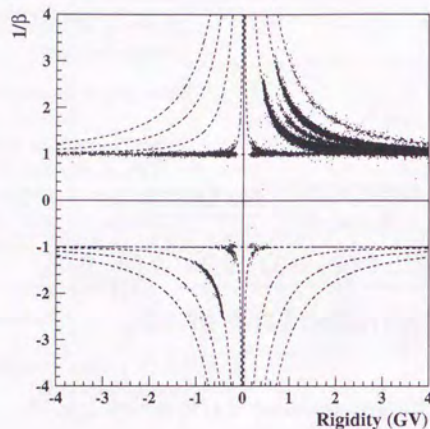
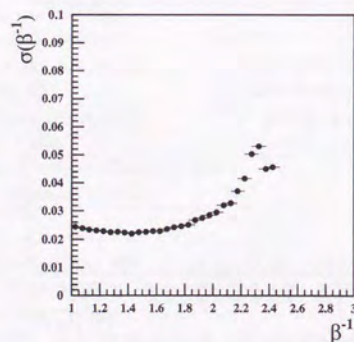


Table 4.3: Summary of the event selection cuts.

Cut No.	Description	BESS '95
	Total Number of events (unbiased events)	4,555,857 (632,376)
Event Reconstruction Requirement		
1.....	Hits in TOF	$N_{\text{TOFU}} = N_{\text{TOFL}} = 1$
2.....	Single and long track	$N_{\text{longtrack}} = 1$
3.....	Expected hits in JET	$N_{\text{expect}} \geq 16$
4.....	$r\phi$ -trajectory agreement with TOF hit counter	$R_{\text{TOFU}}\Delta\phi_U < W_{\text{TOF}}/2 + 10.0\text{mm}$ $R_{\text{TOFL}}\Delta\phi_L < W_{\text{TOF}}/2 + 10.0\text{mm}$
	Number of events after the cuts (unbiased events)	2,636,964 (263,471)
Hit-pattern selection		
1.....		mode = 1,2,6
	Number of events after the cuts (unbiased events)	2,042,843 (186,258)
Track Quality Cut		
1.....	Hits in central region of JET	$N_{\text{cenhit}} \geq 10$
2.....	Hits other than track hits	$N_{\text{extrahit}} \leq 50$
3.....	Unused hits in $r\phi$ -track fitting	$N_{\text{trackhit}} - N_{r\phi\text{-fit}} \leq 8$
4.....	Hits used in $r\phi$ -track fitting	$N_{r\phi\text{-fit}} \geq 10$
5.....	Hits used in $z$ -track fitting	$N_{z\text{-fit}} \geq 6$
6.....	$\chi^2$ in $r\phi$ -track fitting	$\chi^2_{r\phi} < 5$
7.....	$\chi^2$ in $z$ -track fitting	$\chi^2_z < 5$
8.....	$r\phi$ -trajectory agreement with IDC hits	$\min(\Delta(r\phi)_{\text{IDC1i}}, \Delta(r\phi)_{\text{IDC1o}}) < 2.0\text{mm}$ $\min(\Delta(r\phi)_{\text{IDC2i}}, \Delta(r\phi)_{\text{IDC2o}}) < 2.0\text{mm}$
9.....	$z$ -trajectory agreement with IDC hits	$\min(\Delta z_{\text{IDC1i}}/3, \Delta z_{\text{IDC1o}}) < 2.0\text{mm}$ $\min(\Delta z_{\text{IDC2i}}/3, \Delta z_{\text{IDC2o}}) < 2.0\text{mm}$
	Number of events after the cuts (unbiased events)	1,770,346 (164,971)
TOF Quality Cut		
1.....	$z$ -trajectory agreement with TOF counter	$ z_{\text{TRKU}}  < 465\text{mm}$ $ z_{\text{TRKL}}  < 465\text{mm}$
2.....	Trigger time	$0 \text{ ns} < T_{\text{trig}} < 8 \text{ ns}$
3.....	$z$ -trajectory agreement with TOF hits (timing)	$(\Delta z_{\text{TOFU}})^2 + (\Delta z_{\text{TOFL}})^2 < (38.0\text{mm})^2$
4.....	$z$ -trajectory agreement with TOF hits (amplitude)	$(\Delta R_{\text{TOFU}})^2 + (\Delta R_{\text{TOFL}})^2 < (0.3)^2$
	Number of events after the cuts (unbiased events)	1,510,970 (143,467)

Figure 4.13: The estimated error of  $1/R_t$  in  $r\phi$ -fitting.Figure 4.14:  $\Delta(1/R_t)$  as a function of the absolute rigidity.



Figure 4.15:  $\beta^{-1}$  vs Rigidity for unbiased data sample.Figure 4.16: Velocity resolution as a function of  $\beta^{-1}$ .

Two independent measurement errors contribute to the resolution of  $\beta^{-1}$  as follows:

$$\left(\frac{\Delta\beta^{-1}}{\beta^{-1}}\right)^2 = \left(\frac{\Delta t}{t}\right)^2 + \left(\frac{\Delta\ell_{\text{path}}}{\ell_{\text{path}}}\right)^2,$$

where  $t$  the measured TOF and  $\ell_{\text{path}}$  is the path length of the trajectory between the top and the bottom TOF counter. Figure 4.16 shows the resolution of  $\beta^{-1}$  as a function of  $\beta^{-1}$ .

Figure 4.17 shows the  $dE/dx$  measured at the top and bottom TOF scintillators for the unbiased data. We can observe the clear bands of protons, deuterons, muons/pions/electrons,  $^3\text{He}$ , and  $^4\text{He}$  in both figures. It is noted that the top and the bottom scintillators show different  $dE/dx$  behavior in the low rigidity region, where the energy loss in the detector becomes significant.

Figure 4.18 shows the  $dE/dx$  measured at the top and bottom TOF scintillators for the unbiased data. We can clearly observe the bands of protons, muons/pions/electrons, deuterons, heliums. Truncated mean method effectively removes the higher tail of  $dE/dx$  distribution.

The mass of the incident particle is to be calculated from the velocity  $\beta$  and the rigidity  $R$  as:

$$\left(\frac{m}{z}\right)^2 = R^2 \left(\frac{1}{\beta^2} - 1\right).$$

Figure 4.19 shows the mass vs rigidity plots and figure 4.20 shows the mass distributions in certain rigidity regions.

The mass of the observed particles ( $m$ ) also has a relation with momentum  $P$  and the velocity  $\beta$ ;

$$P = m\beta\gamma,$$

$(\beta\gamma)^{-1}$  is obviously proportional to the deflection

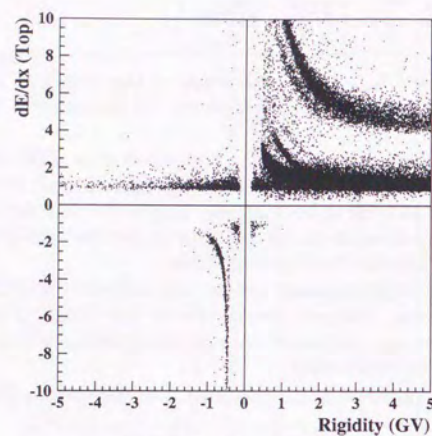
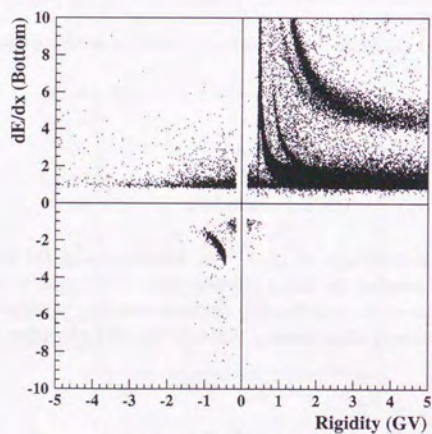
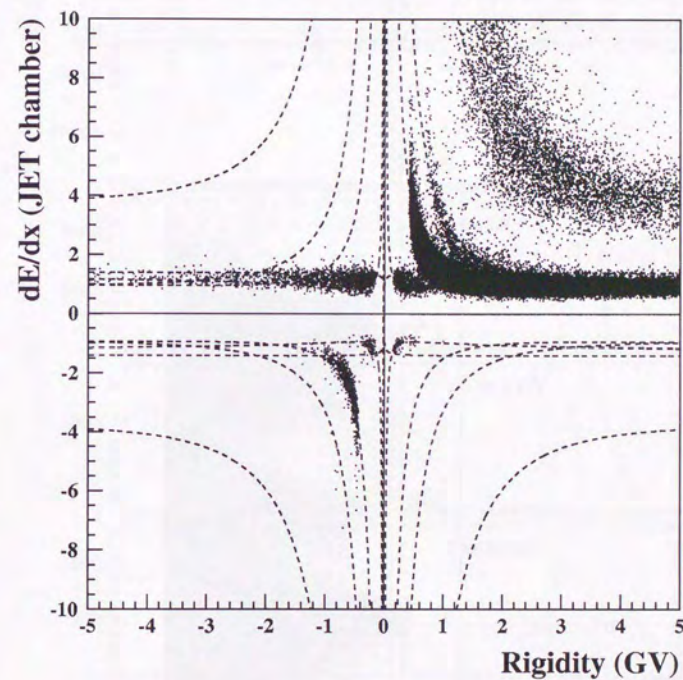
$$(\beta\gamma)^{-1} = (m/ze) \cdot \text{deflection}.$$

Figure 4.21 shows (a) the distribution of  $(\beta\gamma)^{-1}$  vs deflection and (b) its profile histogram for proton events selected by  $dE/dx$  distribution. The mass is measured correctly by the detector without large deflection range, where the incident particle lost a large amount of their energy after passing through the JET chamber in which the rigidity is measured.

## 4.6 Selections of Proton and Antiproton Events

In Section 4.4 are described the selection criteria of fiducial events. Here we discuss the criteria to select proton/antiproton events. The particle identification is made using the mass determined by the rigidity, the velocity and the energy deposit.



(a)  $dE/dx$  (Top) vs Rigidity(b)  $dE/dx$  (Bottom) vs RigidityFigure 4.17:  $dE/dx$  (Scintillator) distribution of the unbiased data samples.Figure 4.18:  $dE/dx$  (JET chamber) vs Rigidity of unbiased data sample.



4.6.1  $dE/dx$  cut

We utilize the band structures in  $dE/dx$  – rigidity plot to extract only protons and antiprotons among other species. Figure 4.22 and 4.23 show  $dE/dx$ -versus-rigidity plots of the top and the bottom scintillators and of the JET chamber, for down-going particles ( $\beta > 0$ ). The dashed lines define the “proton  $dE/dx$ -band”. We require that antiprotons as well as protons must have the  $dE/dx$  in this “proton  $dE/dx$ -band”.

Figure 4.24 shows the distribution of  $dE/dx$  around the proton peak at various rigidities. The dashed lines in the figures represent the boundaries of the selection of protons/antiprotons by  $dE/dx$  cut.

Figure 4.25 shows  $\beta^{-1}$  vs rigidity distributions for the events which passed the

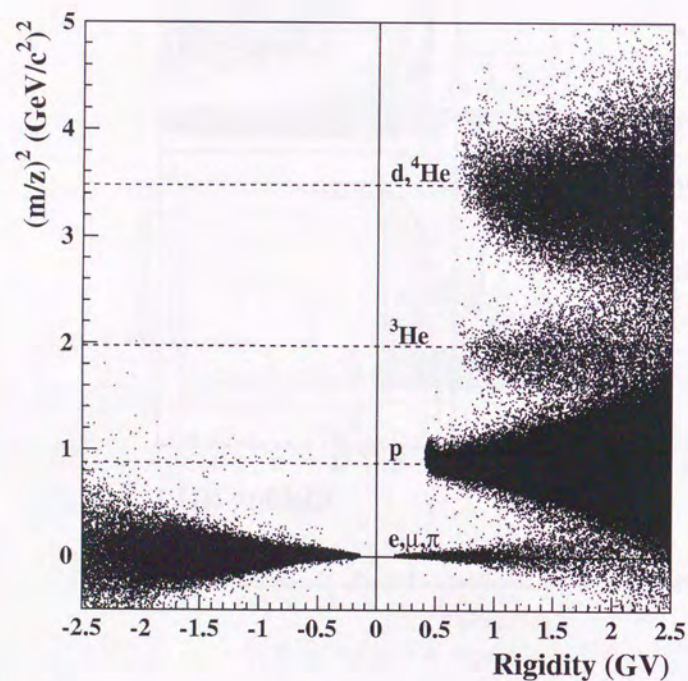


Figure 4.19:  $(m/z)^2$  distribution.

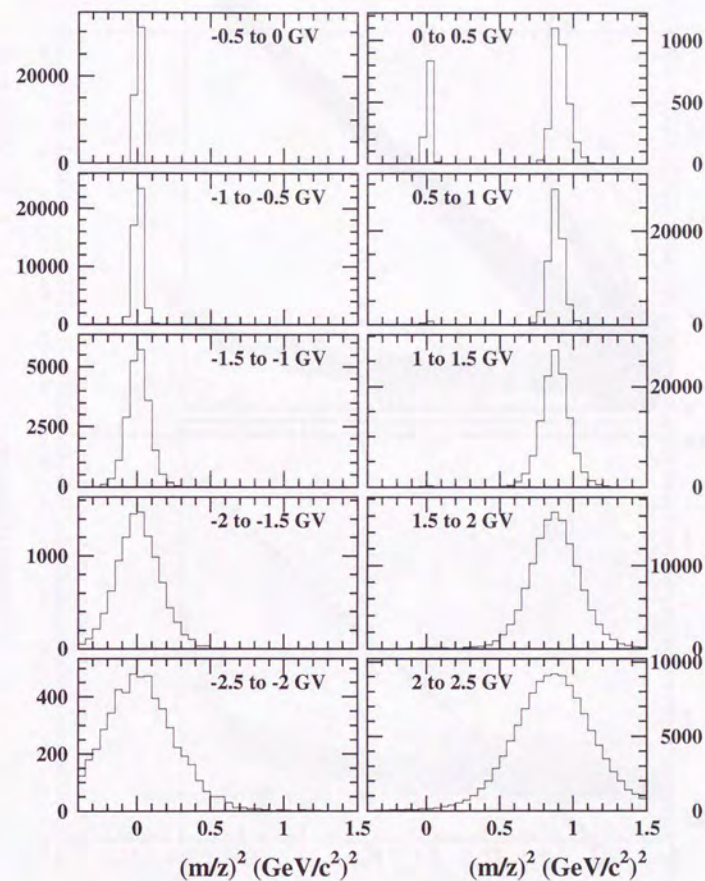


Figure 4.20:  $(m/z)^2$  distribution at various rigidities.



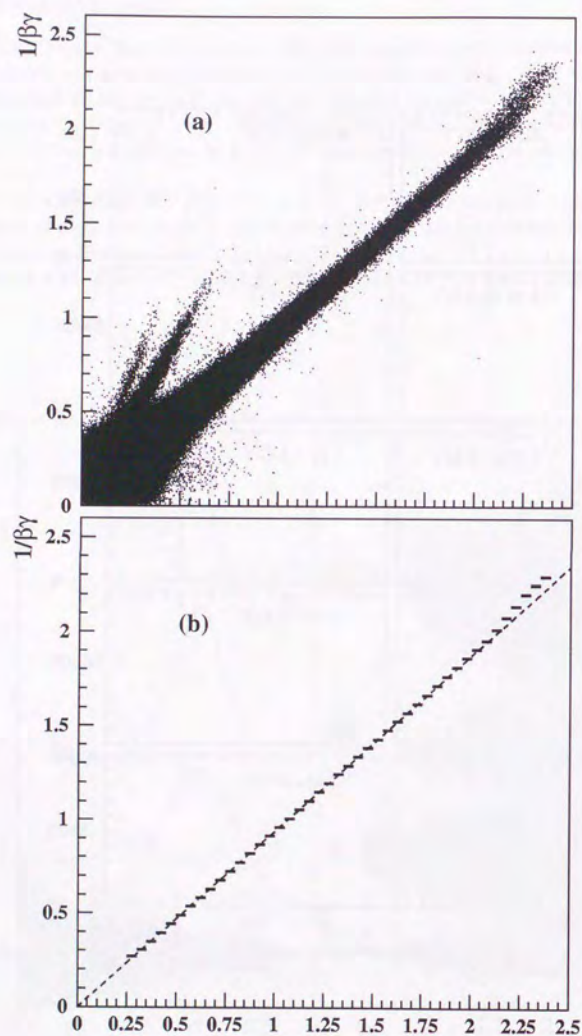


Figure 4.21: (a) Scatter plot of  $(\beta\gamma)^{-1}$  vs deflection and (b) its profile histogram. The line indicates the proton mass.

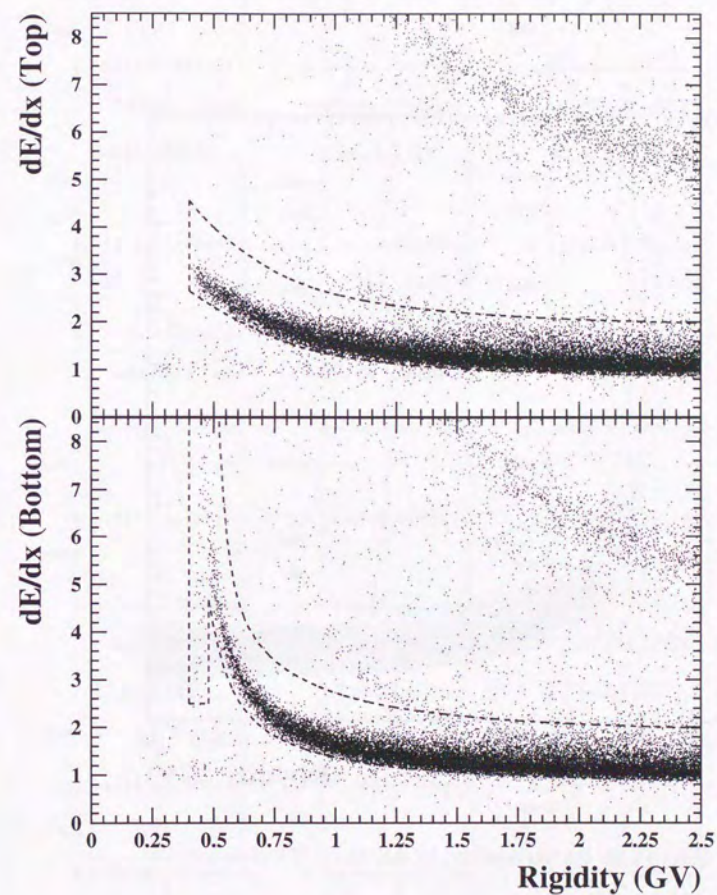
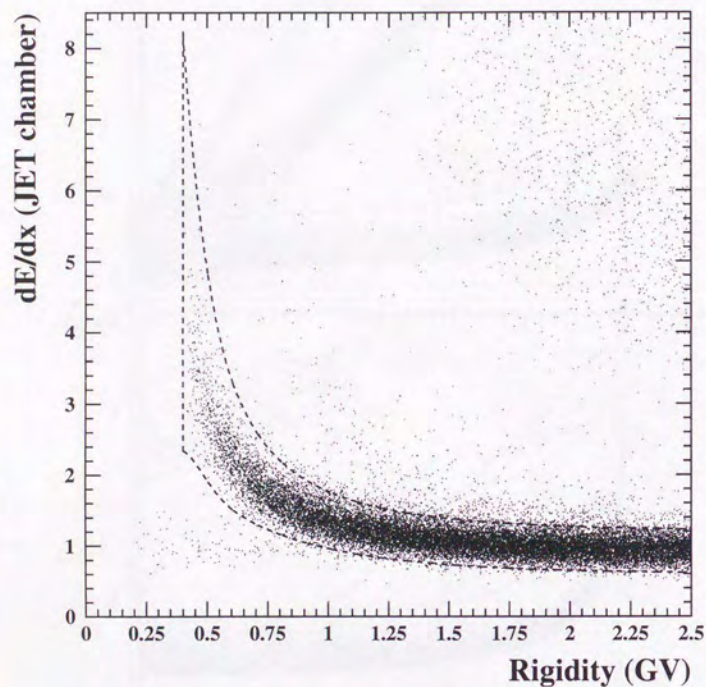
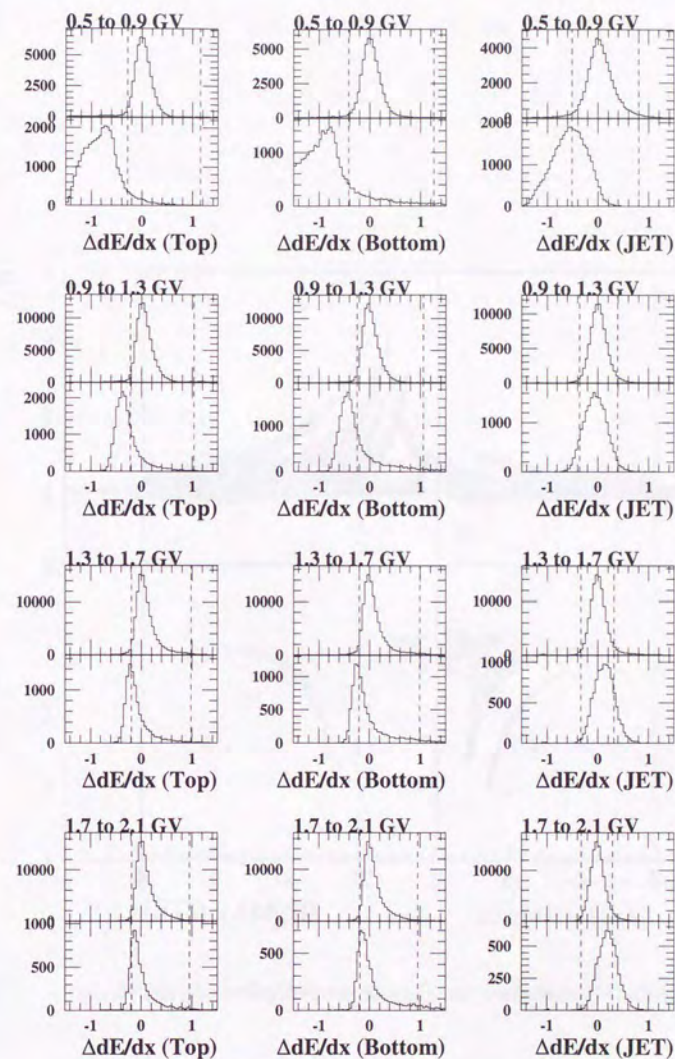
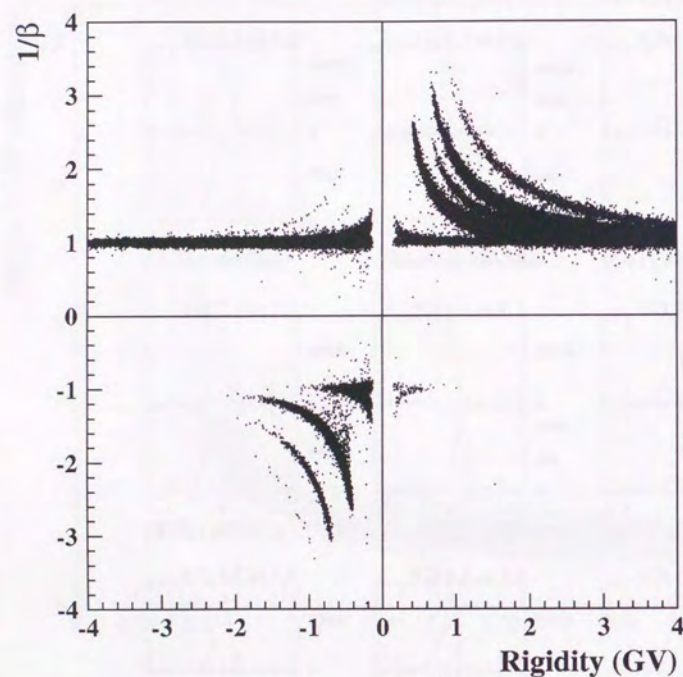
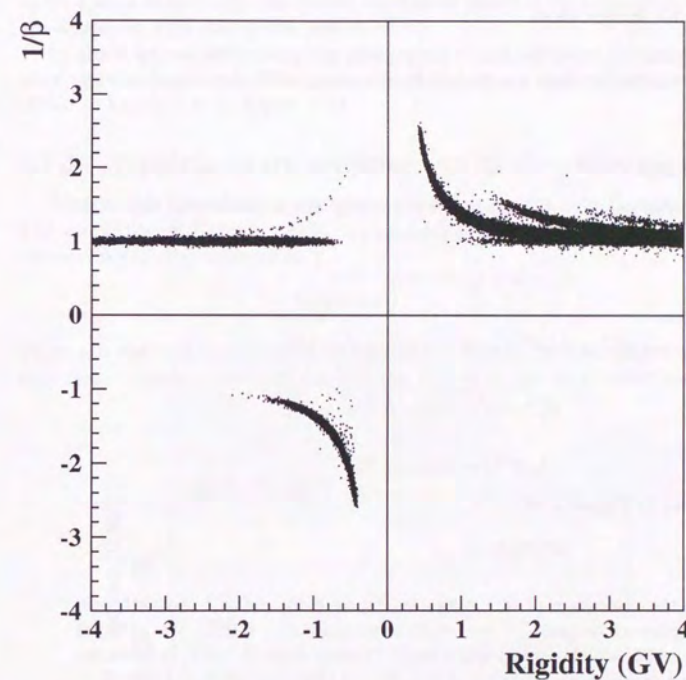


Figure 4.22: Proton selection by  $dE/dx$  in the scintillators.



Figure 4.23: Proton selection by  $dE/dx$  in JET chamberFigure 4.24:  $dE/dx$  distribution relative to the proton peak in the positive and negative rigidity regions. Dashed lines represent the boundaries of the  $dE/dx$  cut at the rigidities of 0.7, 1.1, 1.5 and 1.9 GV, respectively.



Figure 4.25:  $\beta^{-1}$  vs Rigidity for all event samples before  $dE/dx$  cut.Figure 4.26:  $\beta^{-1}$  vs Rigidity for all event samples after  $dE/dx$  cut.



event selection and Figure 4.25 shows for the events which then passed the  $dE/dx$  cut. The particles other than protons are largely reduced at rigidities below 1 GV. It is also worth to note that off-timing events distributed in the region  $-1 < \beta^{-1} < 1$  are clearly swept out by the  $dE/dx$  cut. As Monte Carlo simulations suggests, these are probably due to the events which interacted in the instrument and deposited large energies in the scintillation counter, thus disrupting the time measurement. It is known that our present time-walk corrections is too simple and is not applicable for a very large pulse heights in the scintillation counters.

### 4.6.2 Albedo Rejection

Since we are going to derive the flux of antiprotons and protons at the top of the atmosphere, the further analysis are limited to the events with downward moving particles.

### 4.6.3 Mass cut

The resolution of calculated mass is dominated by the resolution of the TOF measurement or  $\beta^{-1}$ . Thus, a mass-identifying cut

$$m_p - \Delta m < m < m_p + \Delta m$$

is equivalent to

$$\beta_p^{-1} - \Delta(\beta^{-1}) < \beta^{-1} < \beta_p^{-1} + \Delta(\beta^{-1}),$$

where

$$\beta_p^{-1} = \sqrt{1 + (m_p/R)^2}.$$

We adopted

$$\Delta(\beta^{-1}) = 2.58\sigma(\beta^{-1})$$

with  $\sigma(\beta^{-1})$  shown in Figure 4.16.

### 4.6.4 $\beta$ cut

According to the resolution of  $\beta^{-1}$  shown in Figure 4.16, the  $\beta^{-1}$  of relativistic particles are distributed around  $\beta^{-1} = 1$  with a variance  $\sigma \sim 0.025$ . We adopted the cut  $\beta_{\text{cut}}^{-1} = 1.095$ , which correspond  $3.8\sigma(\beta^{-1})$  away from  $\beta^{-1} = 1$ , because no events were found in the region ( $\beta^{-1} < 0.905, R < 0$  GV) nor ( $\beta^{-1} > 1.095, R < -4$  GV). The number of events with rigidities  $-4 \text{ GV} < R < 0$  GV is about  $1.03 \times 10^4$  after the  $dE/dx$  cut and albedo rejection, and supposing the distribution to be normal, or Gaussian, the expected number of events to be found with  $\beta^{-1} > \beta_{\text{cut}}^{-1}$  is less than 1. Figure 4.27 shows  $\beta^{-1}$  distribution of events with rigidities  $-4 \text{ GV} < R < 0$  GV, which has a clear Gaussian shape and its peak value is 1 within error of 0.002.

Furthermore, we restrict ourselves to the absolute rigidity range below 2.1 GV for further antiproton analysis, because the efficiency for this  $\beta$  cut is higher than 50 % in this range.

## 4.7 Selected Events and Background Estimation

After all the cuts had been applied, forty three antiproton events are observed, as shown in Figure 4.28 and 4.29. Close-up views of them near  $\beta^{-1} = 1$  (Figure 4.30 and 4.31) shows antiproton events and cut positions clearly.

Figure 4.32 shows  $m^2$  distributions for events before and after proton/antiproton selection. The antiproton candidates have the same distribution as that of protons, and are well separated from the cluster of muons/pions/electrons.

The  $dE/dx$  values of the candidates are also compared with that of the proton in figure 4.33, 4.34 and 4.35. We can see the  $dE/dx$  values of the antiproton candidates are consistent with that of the proton.

In Table 4.4 are summarized the cuts used to select proton and antiproton events after the event selection. The properties of the proton and antiproton events are shown in Figure 4.36 to Figure 4.43.

### 4.7.1 Supplementary confirmation by Čerenkov signals

The particle identification was also made by using data from Čerenkov counters. The amplitude of Čerenkov light depends on the velocity of the particles which passed through the counters as:

$$\text{amplitude} \propto 1 - \frac{1}{n^2\beta^2},$$

where  $n$  is the refractive index of the counter. Since the Čerenkov lights are emitted at a limited angle relative to the incident direction, the light collection efficiency

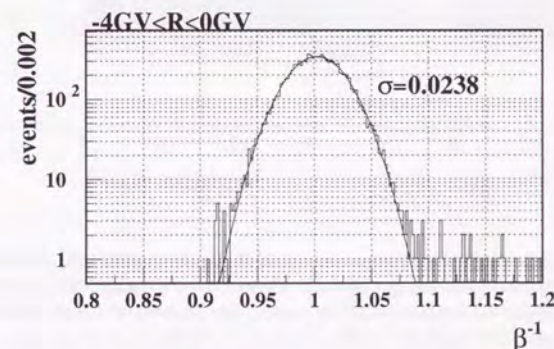


Figure 4.27:  $\beta^{-1}$  distribution of events with rigidities  $-4 \text{ GV} < R < 0$  GV after  $dE/dx$  cut. The curve represents the Gaussian fit which gives  $\sigma = 0.0238$ .



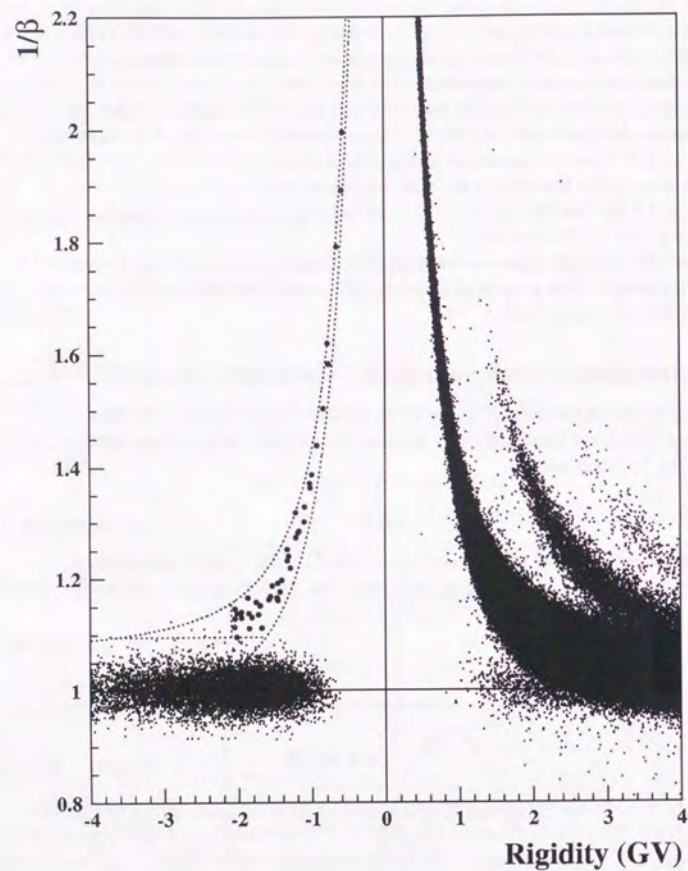


Figure 4.28: The identification of antiproton events (1). All the events that passed the event selection and the  $dE/dx$  cut are plotted. The dotted curves and the dotted lines are the boundaries for the mass cut and the  $\beta$  cut. The antiproton events which we utilize for the flux measurement are marked with filled circles.

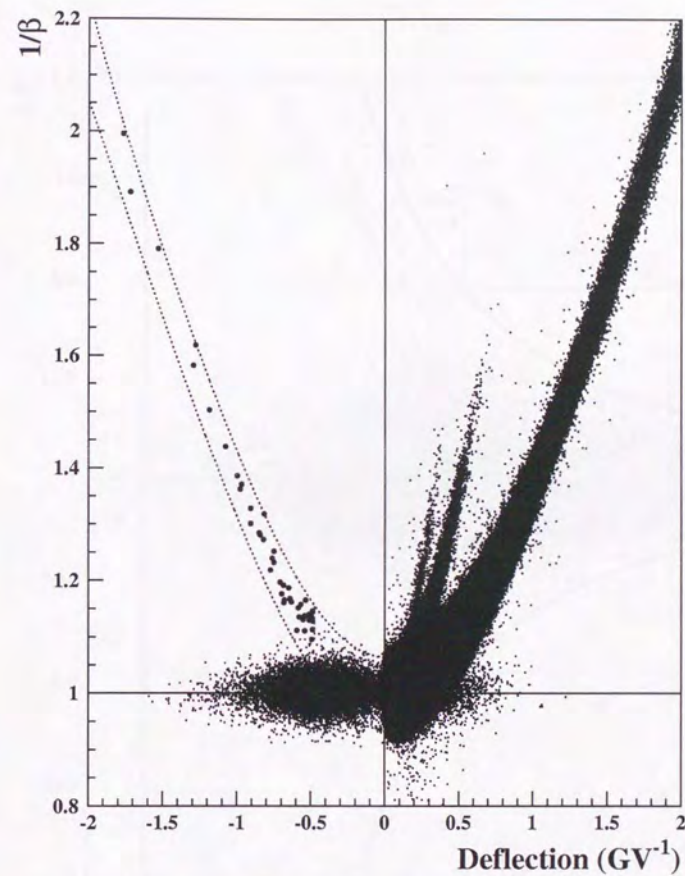


Figure 4.29: The identification of antiproton events (2). The same events as in (1) are plotted. The dotted curves and the dotted lines are the boundaries for the mass cut and the  $\beta$  cut. The antiproton events which we utilize for the flux measurement are marked with filled circles.



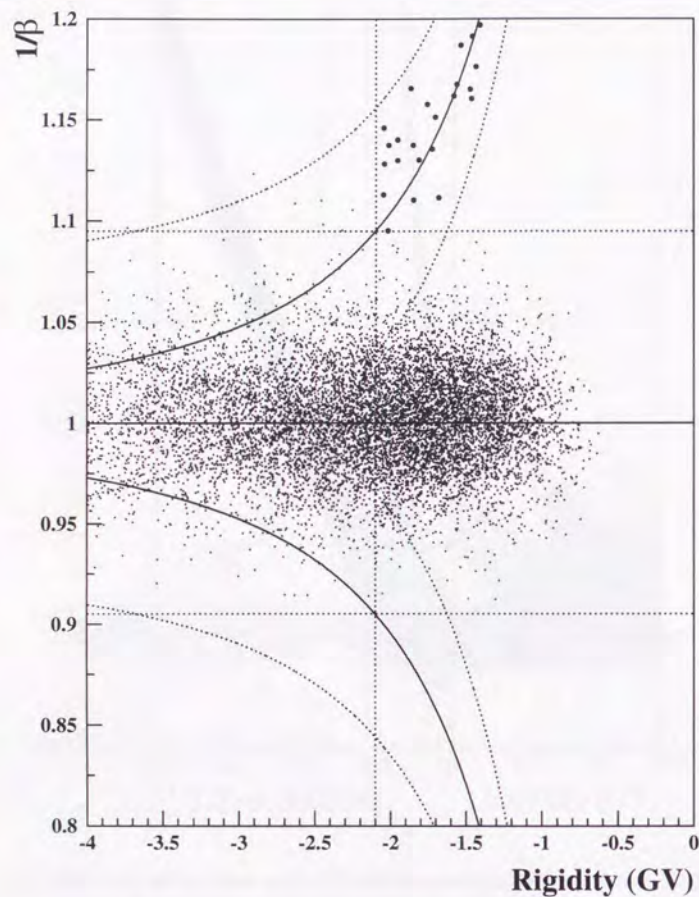


Figure 4.30: Close-up view of  $\beta^{-1}$  vs rigidity for negative-charged particles. The dotted curves and the dotted lines are the boundaries for the mass cut and the  $\beta$  cut, and those symmetrical ones with respect to  $\beta^{-1} = 1$  are also shown. The antiproton events which we utilize for the flux measurement are marked with filled circles.

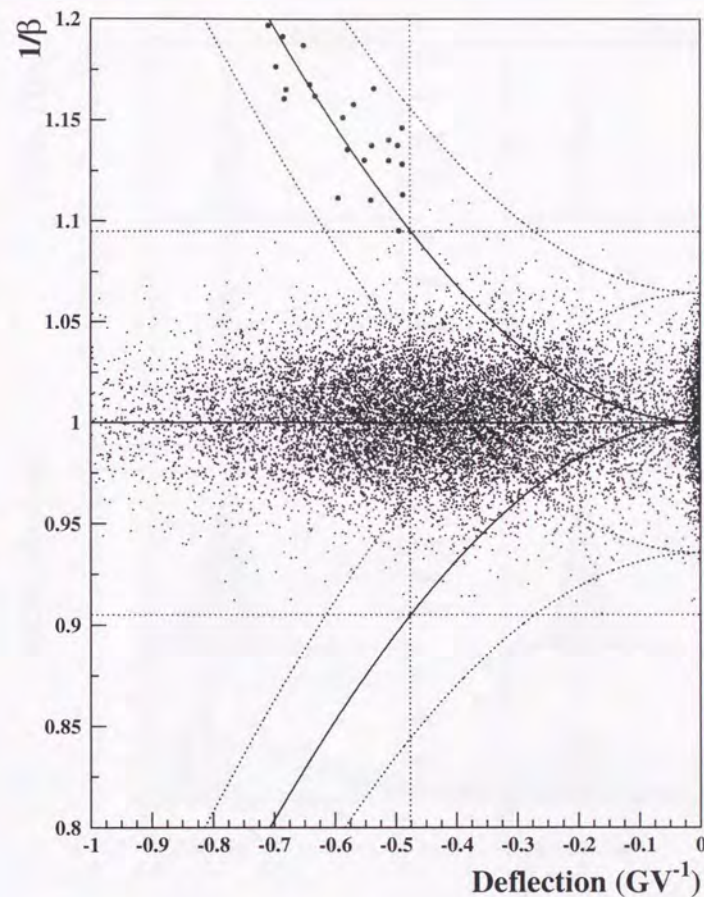


Figure 4.31: Close-up view of  $\beta^{-1}$  vs deflection for negative-charged particles. The dotted curves and the dotted lines are the boundaries for the mass cut and the  $\beta$  cut, and those symmetrical ones with respect to  $\beta^{-1} = 1$  are also shown. The antiproton events which we utilize for the flux measurement are marked with filled circles.



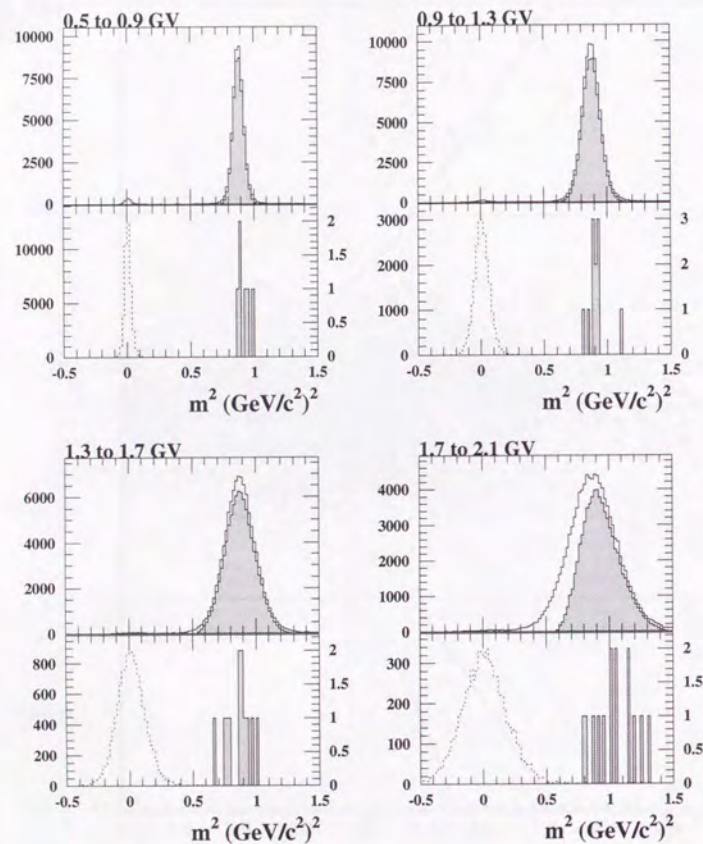


Figure 4.32: Mass of the proton/antiproton events. The shadowed histograms show the square of mass of the antiproton/proton events. The distributions before the proton/antiproton selection are also shown as the open and dotted histograms for a comparison.

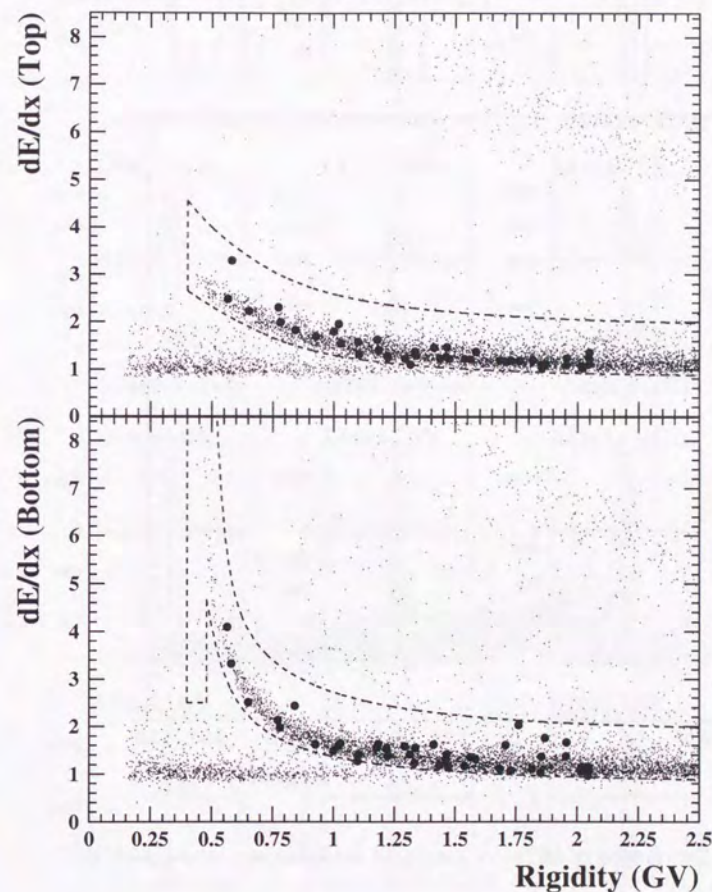


Figure 4.33: Distribution of  $dE/dx$  vs Rigidity of the antiproton events (filled circles). (1)



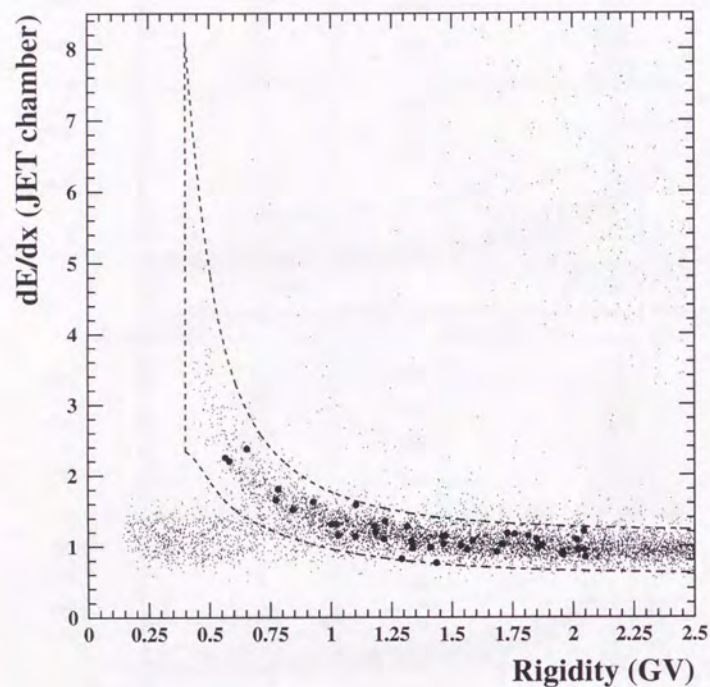


Figure 4.34: Distribution of  $dE/dx$  vs Rigidity of the antiproton events (filled circles). (2)

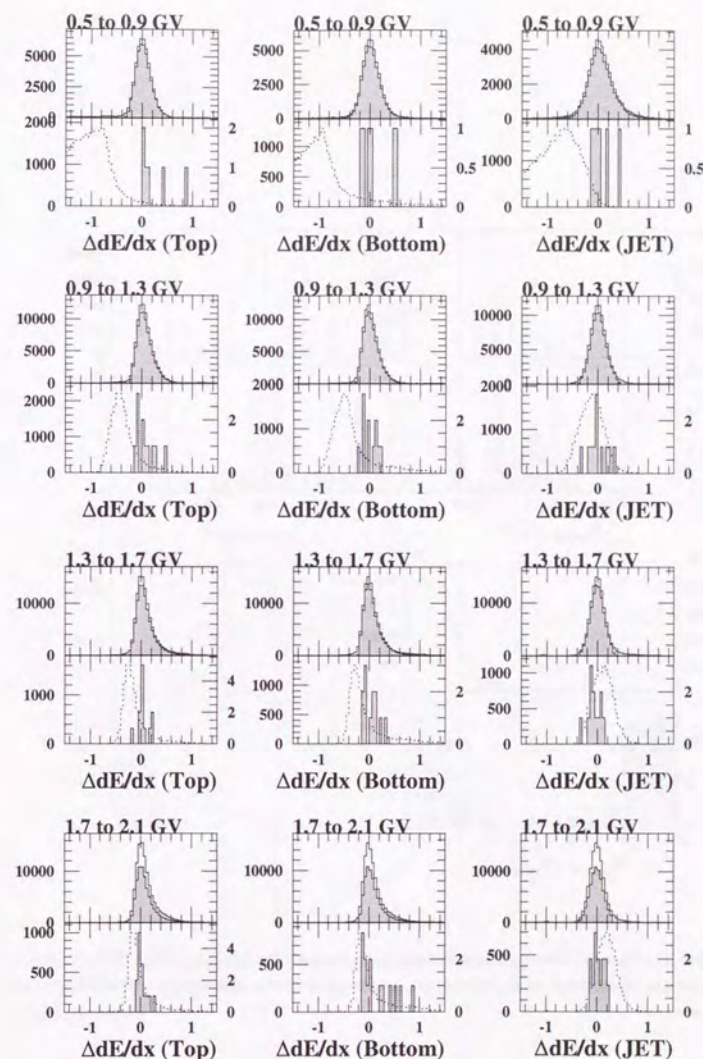


Figure 4.35:  $dE/dx$  distribution relative to the proton peak in the positive and negative rigidity regions. The shadowed histograms show the  $dE/dx$  of the proton/antiproton events. The distributions before the proton/antiproton selection are also shown as the open and dotted histograms for a comparison.



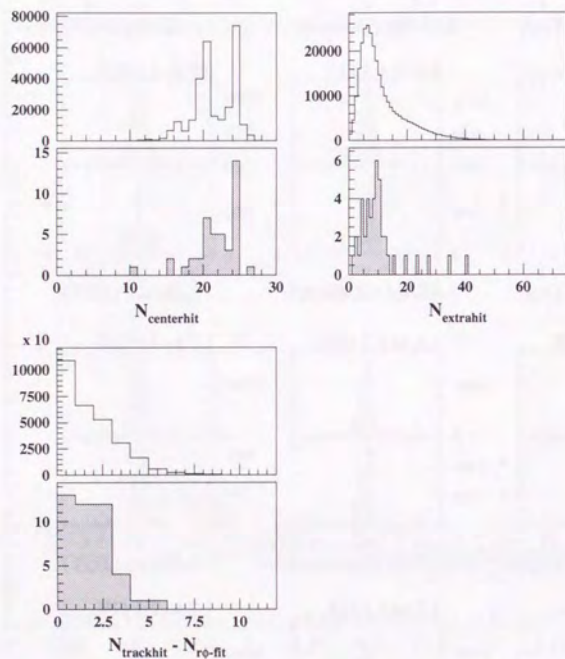


Figure 4.36: The properties of the proton/antiproton events (1). The open histogram shows the distribution for the proton events and the shadowed ones for the antiproton events.

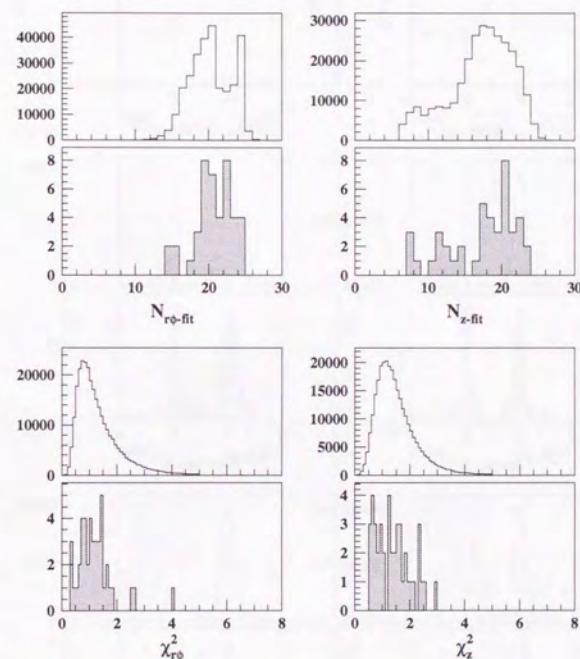


Figure 4.37: The properties of the proton/antiproton events (2). The open histogram shows the distribution for the proton events and the shadowed ones for the antiproton events.



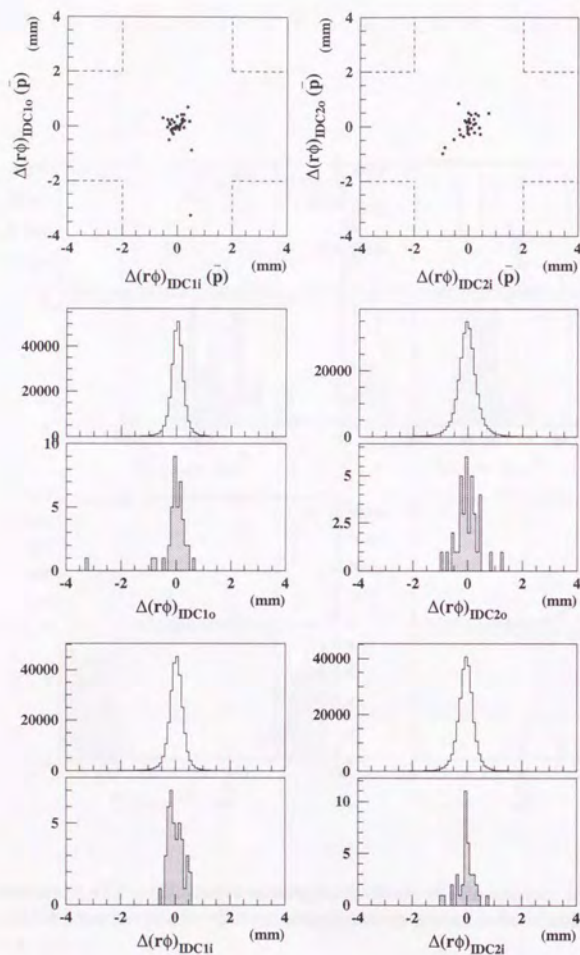


Figure 4.38: The properties of the proton/antiproton events (3). The open histogram shows the distribution for the proton events and the shadowed ones and the filled circles for the antiproton events.

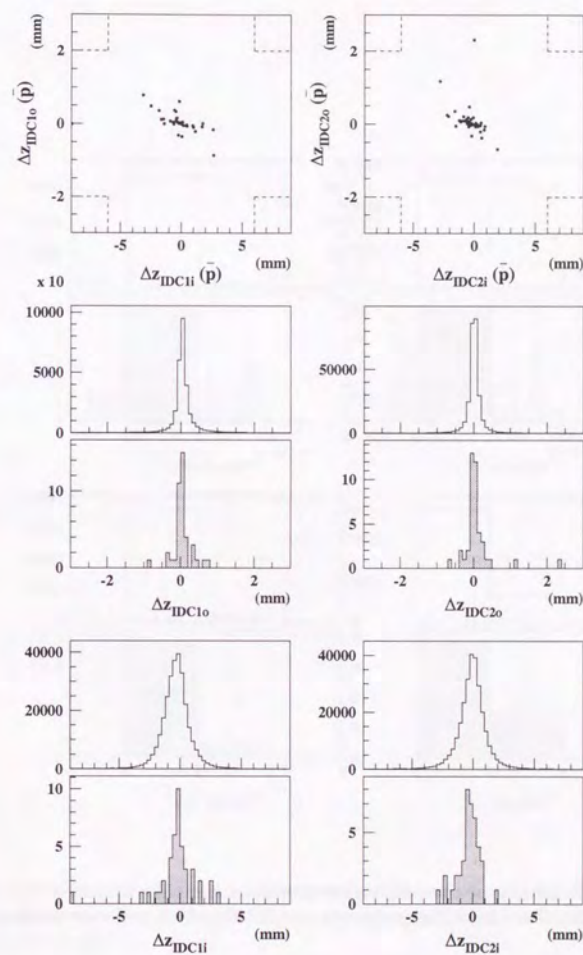


Figure 4.39: The properties of the proton/antiproton events (4). The open histogram shows the distribution for the proton events and the shadowed ones and the filled circles for the antiproton events.



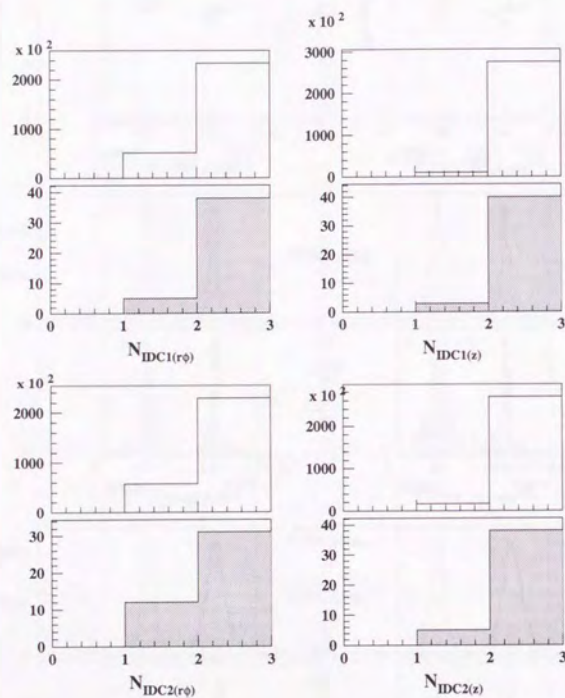


Figure 4.40: The properties of the proton/antiproton events (5). The open histogram shows the distribution for the proton events and the shadowed ones for the antiproton events.

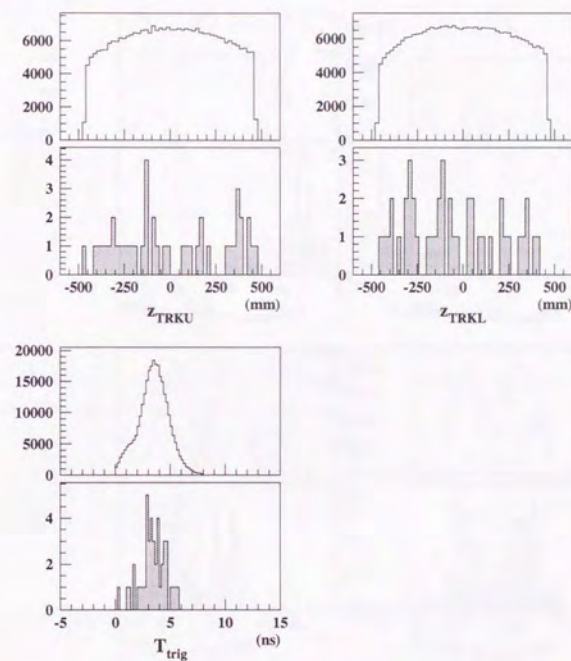


Figure 4.41: The properties of the proton/antiproton events (6). The open histogram shows the distribution for the proton events and the shadowed ones for the antiproton events.



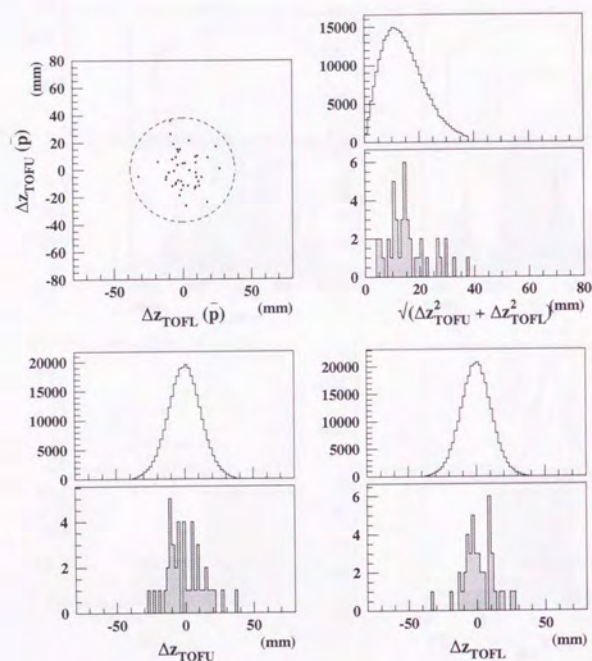


Figure 4.42: The properties of the proton/antiproton events (7). The open histogram shows the distribution for the proton events and the shadowed ones and the filled circles for the antiproton events.

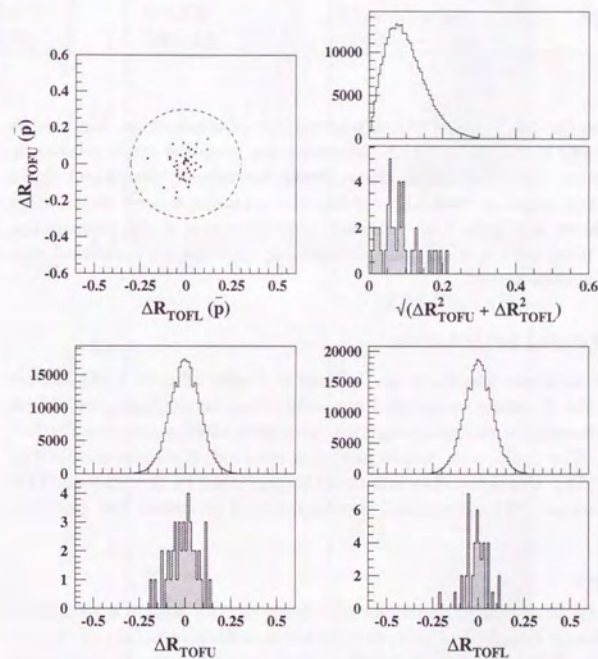


Figure 4.43: The properties of the proton/antiproton events (8). The open histogram shows the distribution for the proton events and the shadowed ones and the filled circles for the antiproton events.



Table 4.4: Summary of the proton/antiproton selection. The cuts were applied in the order as shown here.

Cut No.	Description	Value	Number of events	(unbiased events)
0	the event selection		1,510,970	(143,467)
1	$dE/dx$ cut	$dE/dx$ -band	1,067,223	(113,826)
2	Albedo rejection	$\beta > 0$	1,013,362	(113,158)
3	Mass cut	$m_p \pm 2.58\sigma_p(E)$	983,329	(110,733)
4	$\beta$ cut	$\beta^{-1} > 1.095$	313,603	(65,360)

depends not only on the  $z$ -position which is a parameter of attenuation, but also on the incident angle and the velocity which determine the emission angle relative to the counter dimension. After calibrating these effects, the velocity-dependent signal size was derived, and together with the rigidity the mass-dependent distribution were obtained as shown in Figure 4.44. Although the calibration is still preliminary, antiproton events (filled circles) which pass through the counters are consistent with the distribution of proton events.

#### 4.7.2 Background estimation

The clear band structure visible in the  $1/\beta - R$  plot (Figure 4.28) already demonstrates that the 43 events we selected are antiprotons almost background free. In this section, we investigate various background processes which could possibly fake antiproton events. The antiproton events are mass-resolved, the mass determined by velocity and rigidity. Background events could be produced by the errors in TOF or rigidity measurement. We categorized the background processes into following cases:

##### 1. Proton spillover

Some of the positive charged particles with high rigidity could be recognized as negative charged particles due to the worse resolution in the higher rigidity measurements. This kind of background would be dominated by protons which dominate in the cosmic rays.

##### 2. Albedo protons

Albedo particles which came into the instrument at the bottom, went up and exited at the top, have opposite-curvature to that of down-going particles. The main component of albedo particles, protons, could compose a kind of background when their TOF were wrong by more than ten nanosecond.

##### 3. Negative charged muons/pions/electrons

Since the TOF measurement is less confident than rigidity measurement, negative charged particles are the most likely to fake antiproton events, their

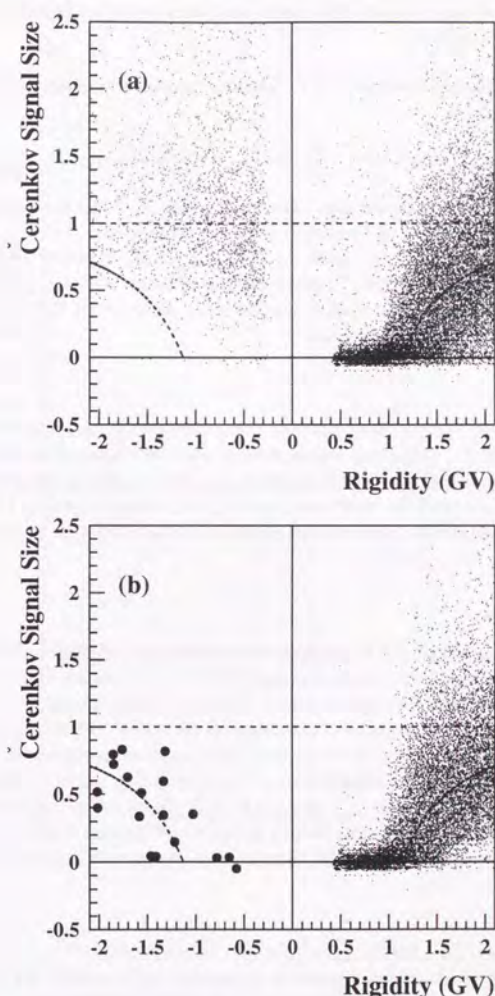


Figure 4.44: Distribution of Čerenkov signal size vs Rigidity of event samples (a) after the event selections and (b) after proton/antiproton selection. Signal size is normalized for energetic particles to have value 1. The dashed curves indicates calculated value for proton/antiproton supposing the refractive index  $n$  is 1.3. The antiproton events are marked with filled circles.



curvature of the trajectory being of the same signature as that of antiprotons. A few nanoseconds of the error in TOF could lead to a wrong recognition of the event as of an antiproton.

For above cases, we examined likelihood of background production using the real flight data.

### Proton spillover

For the case 1, we examined the relative accuracy in the  $R_t^{-1}$  determination, which was obtained in the process of the track fitting. We checked  $\Delta R_t/R_t$  for events with the rigidity between -2.1 GV and -0.5 GV, and found all events in this rigidity range are located more than  $20\sigma$  away from the protons with the infinite rigidity. Therefore the probability of a positive-curved particle (proton) faking any events in this rigidity range is negligibly small.

### Albedo particles

The chance of an albedo particle faking any of the candidates is also extremely small, for even the smallest  $\beta^{-1}$  in the candidates is more than  $40\sigma$  away from those for up-going particles. Figure 4.45 shows  $\beta^{-1}$  distribution which passed through the event selection and the proton  $dE/dx$  band cut in the rigidity range between -4 GV and 0 GV. There are no tail events between two peaks of down-going and up-going particles.

### Light negative particles

As already mentioned in section 4.6.4, the antiproton events are selected to locate  $3.8\sigma$  away from the center of the distribution of the relativistic particles. However, the possibility remains that they are mis-identified electrons/muons/pions.

Figure 4.46 shows  $\beta^{-1}$  distribution of light negative particles. First, we can clearly see in (a) the separation of antiprotons and light negative particles in low energy region. In addition, the  $\beta^{-1}$  distribution of light negative particles has a Gaussian shape with symmetrical tails. In figure 4.46 (b), where twice number of particles contained, around  $\beta^{-1} = 0.92$  the similar tail of the Gaussian distribution can be confirmed, therefore it is not expected that the tail in opposite (upper) side spill over the  $\beta$  cut.

Thus detailed check of the candidates revealed no sign of background. We conclude that the antiproton candidates we selected have negligible backgrounds.

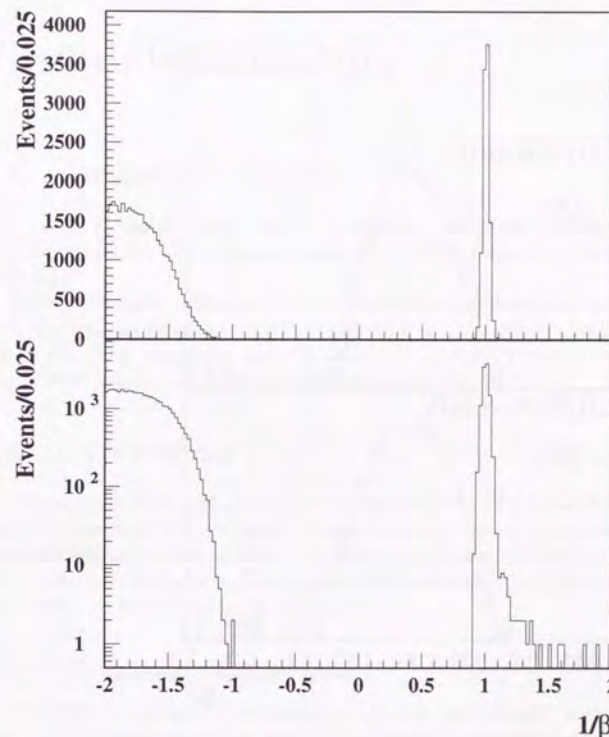


Figure 4.45:  $\beta^{-1}$  distribution of negative-charged particles at rigidities -4GV to 0GV after  $dE/dx$  cut. The two graphs are for the same histogram with linear and logarithmic scales.



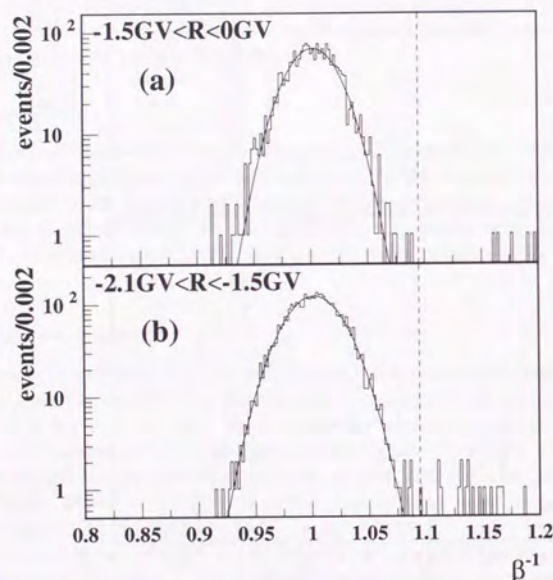


Figure 4.46:  $\beta^{-1}$  distribution of light negative particles at rigidities (a) -1.5 GV to 0 GV and (b) -2.1 GV to -1.5 GV after  $dE/dx$  cut. The dashed line indicates the  $\beta$  cut position.

## Chapter 5

### Flux determination

#### 5.1 Antiproton Events

As seen in the previous chapter, forty three antiprotons events are obtained after the selections. The principal properties of the antiproton events are listed in Table 5.1.

Typical examples of the antiproton candidates are shown in Figure 5.1 to 5.4. Each of the 43 antiprotons is closely investigated in the event display for the correctness of the track recognition and the fitting etc. All of the candidate events show clear tracks, and no particular problem has been detected.

#### 5.2 Corrections

The antiproton flux at the top of the atmosphere (TOA) was derived from the number of the mass-resolved antiprotons by applying several corrections. The corrections were made for the selectional efficiencies, the exposure factor of the experiment and the atmospheric effects. This section discusses such corrections using both real flight data and Monte Carlo simulation data.

##### 5.2.1 Ionization Energy Loss

The observed protons and antiprotons had lost their energies while they had traversed typically  $5 \text{ g/cm}^2$  of the atmosphere above the instrument and also  $9.0 \text{ g/cm}^2$  of the upper half material of the instrument before they were detected at JET chamber in the solenoidal magnetic field. The energy of a particle after traveling into a depth  $x$  is given as:

$$E(x) = E(0) - \int_0^x \frac{dE}{dx}(E) dx.$$

The energy at the top of the atmosphere  $E(0)$  is then derived by using  $E(x)$ , the energy measured at JET chamber,  $dE/dx$ , the ionization energy loss per unit depth, and  $x$ , the thickness of the materials. The actual thickness of the material for a particle to traverse depends on the inclination of the particle trajectory. The total



Table 5.1: The principal properties of the antiproton events.  $E^{\text{obs}}$  represents for the kinetic energy measured in JET chamber and  $E^{\text{TOA}}$  for the kinetic energy at the top of the atmosphere.

	Run	Event No.	Rigidity (GV)	$\beta$	$E^{\text{obs}}$ (MeV)	$E^{\text{TOA}}$ (MeV)	$(\text{Mass})^2 (\text{GeV}/c^2)^2$
1	7	185505	-1.707	0.869	1009	1040	0.949
2	7	208865	-1.956	0.885	1231	1259	1.060
3	7	279113	-0.581	0.529	165	229	0.870
4	7	418502	-1.436	0.850	777	809	0.792
5	8	594519	-1.315	0.807	677	711	0.927
6	8	638799	-1.466	0.862	802	832	0.746
7	8	693906	-1.815	0.885	1105	1134	0.914
8	8	791373	-1.869	0.858	1153	1184	1.253
9	9	891297	-1.219	0.786	600	634	0.919
10	10	1201104	-2.015	0.879	1285	1312	1.193
11	10	1276735	-1.102	0.768	509	545	0.843
12	10	1342616	-1.957	0.877	1232	1262	1.149
13	12	1837440	-1.021	0.734	448	487	0.892
14	12	2054818	-1.001	0.722	434	472	0.922
15	13	2262192	-1.683	0.900	989	1018	0.667
16	14	2408620	-1.850	0.901	1136	1164	0.796
17	15	2455506	-1.473	0.858	808	839	0.776
18	15	2492106	-2.049	0.899	1316	1343	1.002
19	15	2630469	-0.652	0.558	204	267	0.938
20	15	2639355	-1.854	0.879	1140	1169	1.011
21	15	2666564	-2.044	0.886	1311	1339	1.140
22	15	2701910	-1.292	0.821	659	690	0.809
23	15	2828264	-1.727	0.881	1028	1059	0.863
24	16	3142047	-1.184	0.781	573	610	0.898
25	16	3156318	-0.781	0.618	283	330	0.989
26	17	3465653	-2.046	0.872	1313	1343	1.314
27	17	3487752	-1.584	0.861	903	935	0.879
28	18	3541252	-2.020	0.913	1289	1319	0.815
29	18	3553926	-1.178	0.779	568	605	0.899
30	18	3847422	-1.759	0.864	1056	1084	1.053
31	19	4015537	-1.336	0.799	694	727	1.011
32	19	4094573	-1.332	0.812	691	725	0.918
33	19	4118693	-1.537	0.842	863	893	0.966
34	19	4119545	-1.461	0.839	798	831	0.896
35	19	4142171	-0.842	0.665	322	366	0.893
36	20	4229034	-1.562	0.856	884	922	0.887
37	20	4325262	-1.223	0.759	603	636	1.102
38	20	4448409	-1.411	0.835	756	788	0.862
39	22	60807	-0.772	0.632	277	325	0.896
40	22	68365	-1.030	0.730	455	499	0.931
41	22	71318	-1.100	0.753	508	547	0.924
42	22	239332	-0.926	0.696	380	420	0.915
43	22	266711	-0.565	0.501	157	223	0.952

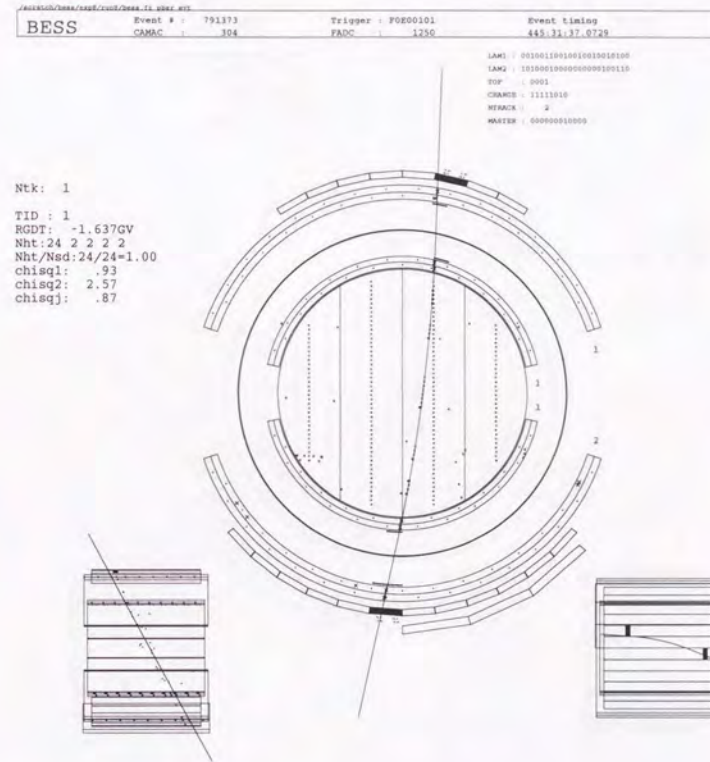


Figure 5.1: Event display of an antiproton candidate (1).



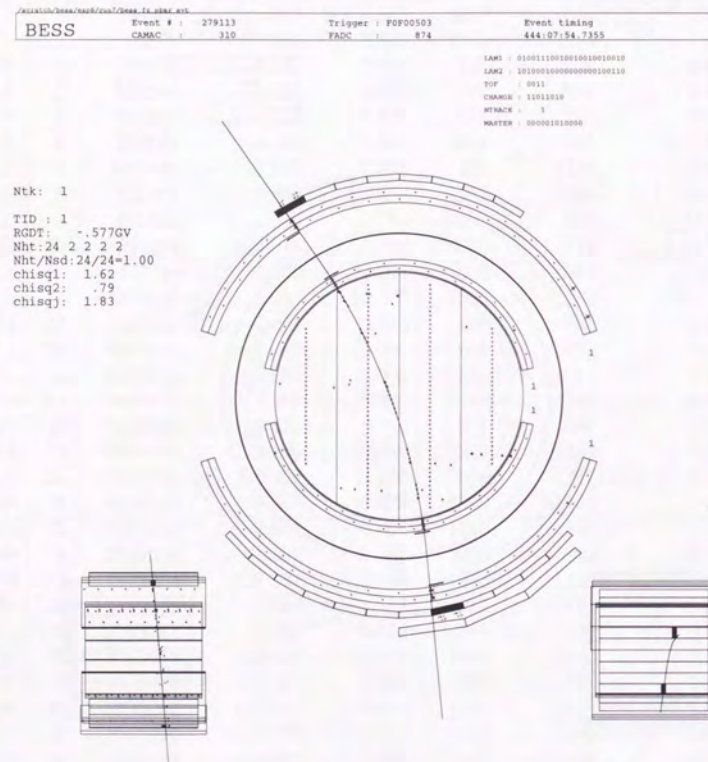


Figure 5.2: Event display of an antiproton candidate (2).

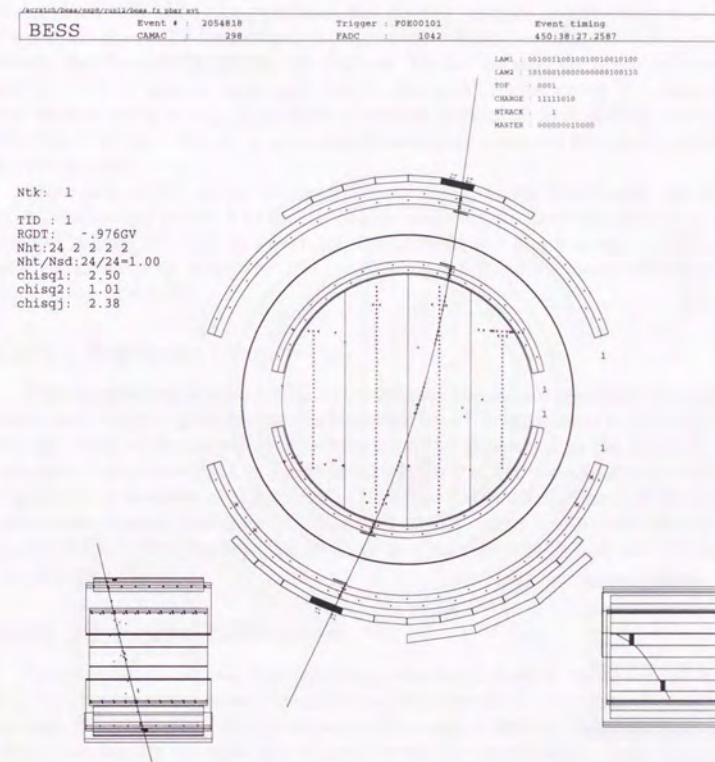


Figure 5.3: Event display of an antiproton candidate (3).



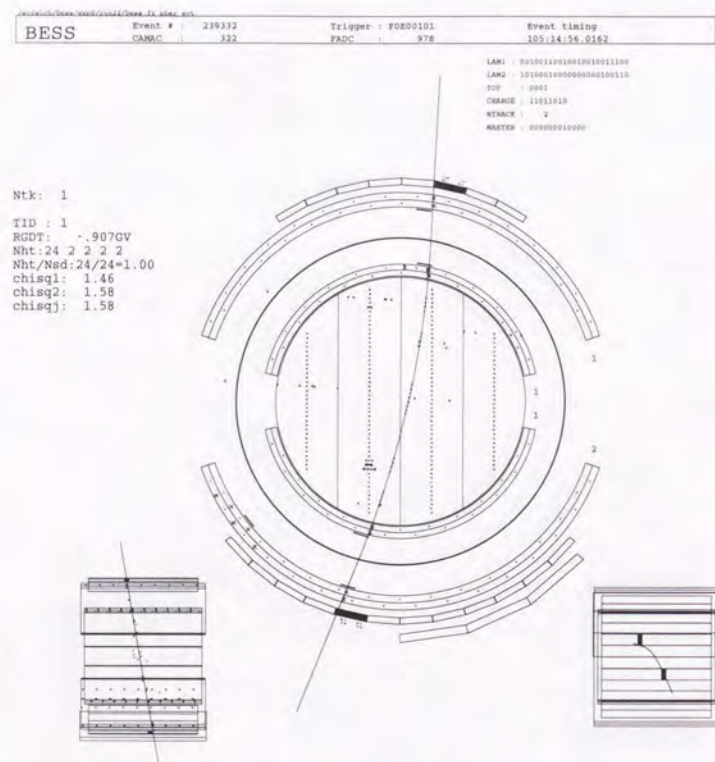


Figure 5.4: Event display of an antiproton candidate (4).

energy loss is calculated for each event by summing up the energy losses at every steps in the detector components and in the atmosphere.

Since low energy particles lose large amount of their energies, the fluctuations of the energy losses seem to be large. We then estimate the accuracy of the derived energy at the top of the atmosphere for two antiprotons with the lowest energies. To do this, using GEANT simulation, antiprotons were injected from the top of the atmosphere with the same directions and derived energies as the observed events. Figure 5.5 shows the initial(open histograms) and measured(hatched histograms) energy distributions for the two antiprotons. We can see that the measured energies are expected to have an accuracies within a few MeV. As the result, it is natural for the derived energies calculated from measured energies to have similar accuracies. We thus concluded that the fluctuations of the energy losses are too small to consider for corrections.

From now on, we use the estimated kinetic energy at the TOA in the calculation of efficiencies and fluxes. The kinetic energy range for the determination of antiproton flux is from 175 MeV to 1400 MeV, the lower limit comes from the cutoff for the protons/antiprotons to stop in the bottom scintillator and the latter corresponds to the rigidity of 2.1 GV.

### 5.2.2 Exposure Factor

The geometrical acceptance is determined by the simple geometry and can be calculated reliably by the Monte Carlo simulation. The acceptance is defined by the fiducial region of the detector by switching off the interaction in the detector. The calculated acceptance,  $S\Omega$ , is identical for antiproton and proton, and is shown in Figure 5.6 as function of the energy. The  $S\Omega$  is 0.32 m<sup>2</sup>sr for most of the energy region, and slightly decreases at the lowest energy region due to the effect of the track bending. The 'live time' in '95 flight is measured to be  $2.7 \times 10^4$  sec (7.6 hours) (see Chapter 3).

### 5.2.3 Selection Efficiencies

As described in Section 4.4, the event selection is done in rigidity-symmetrical way, *i.e.*, in identical manner to protons and to antiprotons. Therefore, the approach we take in determining the antiproton efficiencies is first to measure the proton efficiencies directly by utilizing the proton events in the unbiased trigger samples of the actual flight data. We then multiply by the ratio of the simulated antiproton efficiencies to the simulated proton efficiencies, for the part to which there is no other way at moment than to reply on the simulations, such as the interaction losses. In this way, we try to minimize the ambiguity due to the simulations.

The proton samples utilized to derive the selection efficiencies were obtained from the unbiased trigger events by applying following very loose selections on the single track events:

- $z=1$

Very loose cuts on  $dE/dx$  at TOF counters just to rejecting events with  $z \geq 2$ .



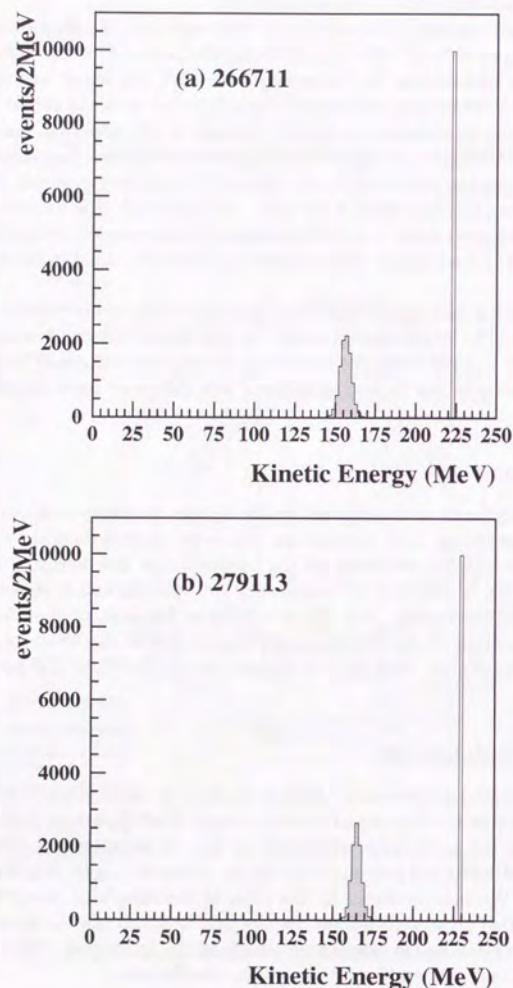


Figure 5.5: Estimation of the fluctuations of the energy losses using Monte Carlo simulation. (a) shows for the lowest energy antiproton (event number of 266711) and (b) for the second lowest energy antiproton (event number of 279113). Open histograms represents the initial energies at TOA and hatched histograms the expected energies to be measured in JET chamber.

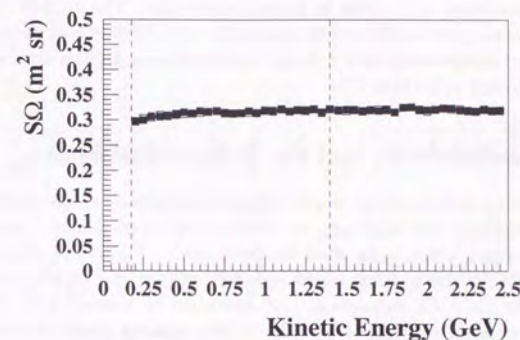


Figure 5.6: The geometrical acceptance ( $S\Omega$ ) as function of the energy. Filled and open squares are calculated by Monte Carlo simulation for protons and antiprotons, respectively

$$\bullet \left| \frac{1}{\beta} - \sqrt{\left(\frac{m_p}{R}\right)^2 + 1} \right| < 3.89\sigma(\beta^{-1})$$

A loose  $\beta$  cut.  $\sigma(\beta^{-1})$  is provided in Figure 4.16.

Since events with positive rigidities are dominated by protons and heliums, these loose selections extract pure proton samples with essentially no background.

The off-line selection efficiencies can be decomposed into the following efficiencies to better understand the effects of the selection, although only the over-all selection efficiency is needed to obtain the antiproton flux.

1. Efficiency of the track quality cut ( $\varepsilon_{\text{track}}$ ).
2. Efficiency of the selection for the good timing measurement ( $\varepsilon_{\text{TOF}}$ ).
3. Efficiency of the  $dE/dx$  cut ( $\varepsilon_{dE/dx}$ ).
4. Efficiency of the mass cut ( $\varepsilon_{\text{mass}}$ ).
5. Efficiency of the  $\beta$  cut ( $\varepsilon_{\beta}$ ).

Figure 5.7 shows these off-line selection efficiencies at each step and over-all selection efficiency as function of the kinetic energy at the top of the atmosphere. The filled circles in this figure represent the efficiencies directly obtained by the proton samples. The open triangles, almost indistinguishable from filled circles, are the



efficiencies for the antiproton, which is obtained by multiplying the proton efficiencies by the ratio of the simulated antiproton to proton efficiencies. The antiproton efficiencies are identical to the proton efficiencies, except for small differences at the lowest energies, where the antiprotons have a higher cross sections for the nuclear cross interactions as described in Section 4.3.

### 5.2.4 Single Track Efficiency and the Trigger Efficiencies

The single track efficiency is determined mainly by the interactions in the upper half of the detector. To estimate this efficiency, we need to rely on the Monte Carlo simulations until our planned beam tests shall be performed. Figure 5.8 shows the single track efficiencies for the protons (filled squares) and for the antiprotons (open squares) derived by GEANT simulation. As described in Section 4.3, the proton-nucleus cross sections in the GEANT code fit the existing data. As for the antiproton-nucleus cross sections, we have utilized the fitting function which precisely reproduces the existing data. In the simulation, we put in the three-dimensional detector configuration in detail.

The track trigger efficiencies can be decomposed into the “hit-pattern selection efficiency ( $\varepsilon_{\text{TT-pattern}}$ )” and the “deflection selection efficiency ( $\varepsilon_{\text{TT-def}}$ )”. Shown in Figure 5.9 is the  $\varepsilon_{\text{TT-pattern}}$  efficiency determined by the unbiased proton sample (filled circles). As shown by open triangles, almost indistinguishable, in this figure, the simulation predict that the  $\varepsilon_{\text{TT-pattern}}$  for the antiprotons must be almost identical to the one of the protons.

The “deflection selection efficiency ( $\varepsilon_{\text{TT-def}}$ )” can be determined by utilizing both the proton events and the negative electron/muon events in the unbiased sample. The resultant  $\varepsilon_{\text{TT-def}}$  is shown in Figure 5.10 as function of the deflection. The  $\varepsilon_{\text{TT-def}}$  thus determined for negative charged particles such as antiprotons is 95 % in the rigidity region below 1 GeV/c and decrease to 80 % at 1.5 GeV/c.

### 5.2.5 Atmospheric Secondary Production

Antiprotons can be produced above the instrument by collisions of the cosmic rays with the nuclei in the atmosphere. The observed number of the antiprotons may include the atmospheric secondaries and these portions should be subtracted in order to obtain the primary flux at the top of the atmosphere. Figure 5.11 shows the secondary antiproton flux calculated by various authors [1, 67, 68]. We note that the calculated secondary antiproton fluxes agree reasonably well despite of very different nuclear models used in the calculations. We adopted the flux by Mitsui [1], since it is based on the most detailed calculations, performed three-dimensionally, including detailed effects of nuclear interactions and the inelastic collisions of produced antiprotons. Mitsui also uses the incident proton flux measured by the LEAP experiment [70] which agree with the preliminary data from BESS experiment. The dependence on the solar modulation is negligibly small for the secondary antiproton flux.

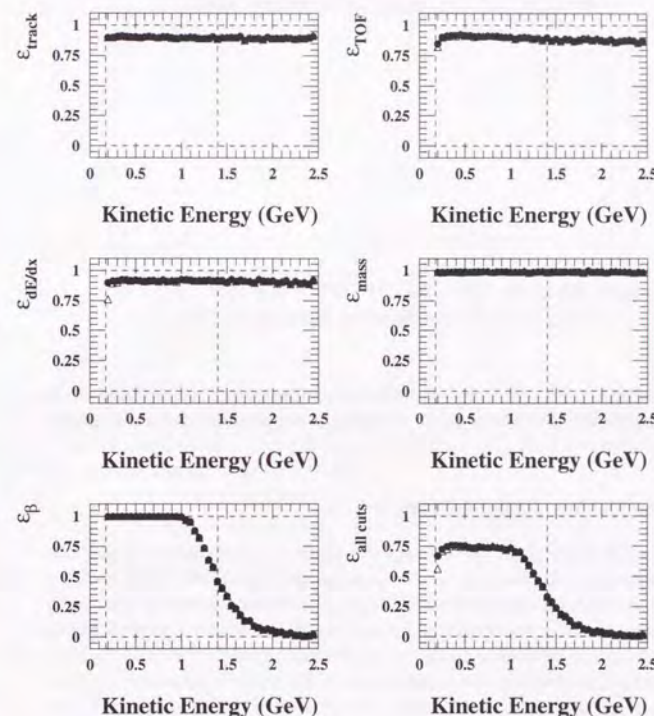


Figure 5.7: Off-line Selection efficiencies for protons and antiprotons. Filled circles are obtained from flight data for protons; open triangles are for antiprotons, derived by combining the flight data for protons and the efficiency ratio of antiprotons to protons.



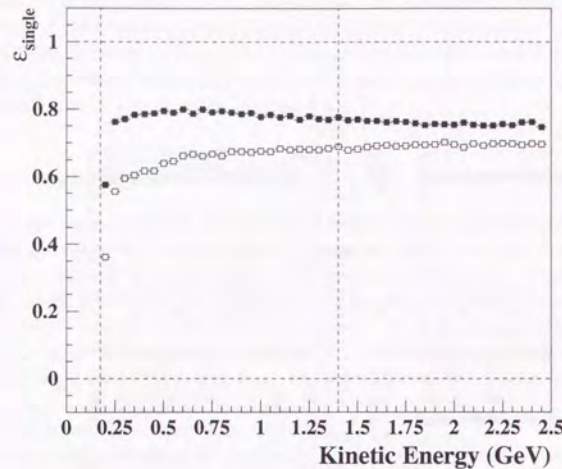


Figure 5.8: The single track efficiency as function of the energy. Filled and open squares are calculated by the Monte Carlo simulation for protons and antiprotons, respectively.

### 5.2.6 Losses in the Atmosphere

Interactions in the  $5 \text{ g/cm}^2$  of the atmosphere above the instrument reduce the number of antiprotons to be observed in the experiment. This process is simulated by the GEANT code with the standard model atmosphere. For this study, the zenith angle of the incident particles are distributed according to the observed proton zenith angle which we assume to be similar to the one of the antiproton. Figure 5.12 shows the estimated survival probability for protons and antiprotons to penetrate  $5 \text{ g/cm}^2$  of the atmosphere for various initial energies at the top of the atmosphere. The survival probability for antiprotons declines at low energies due to the annihilations, while that for protons is almost constant over the entire energy range.

### 5.2.7 Interactions in the Atmosphere

The ionization energy loss and the decrease of the flux due to the interactions in the atmosphere are considered in Section 5.2.1 and Section 5.2.6. In this section, we consider the possible deformation of the antiproton spectrum due to elastic and inelastic interactions with the nuclei in the atmosphere.

A fraction of the antiprotons incident onto the atmosphere will suffer elastic or inelastic interactions in traveling through the  $5 \text{ g/cm}^2$  of the air, producing secondary

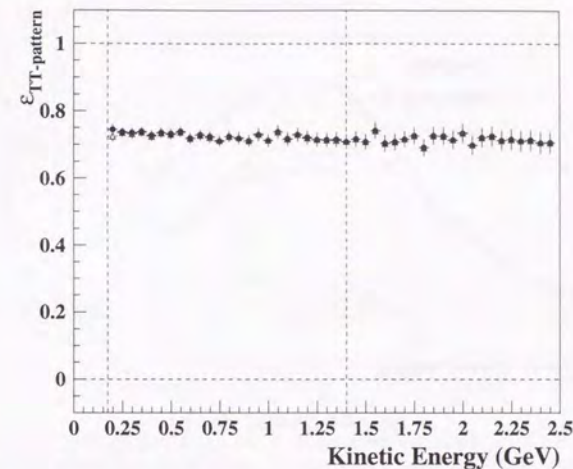


Figure 5.9: Track Trigger hit-pattern selection efficiency. Filled circles are obtained from flight data for protons; open triangles, almost indistinguishable from filled circles, are for antiprotons, derived combining the flight data for protons and the efficiency ratio of antiprotons to protons.

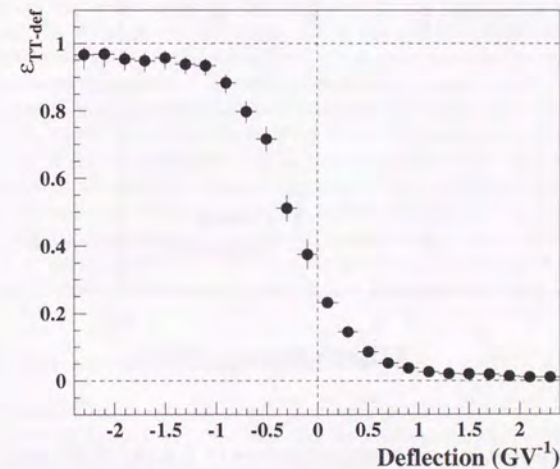


Figure 5.10: Track Trigger deflection selection efficiency.



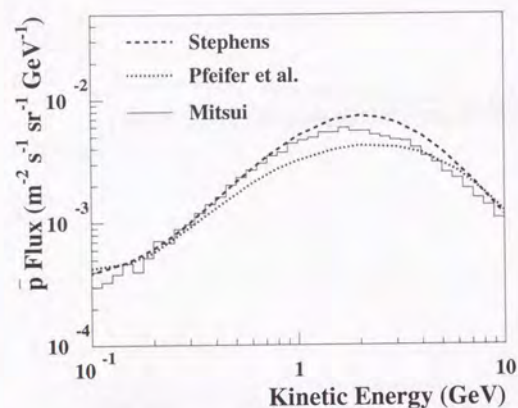


Figure 5.11: Secondary antiproton flux at an atmospheric depth 5 g/cm<sup>2</sup>. The dashed curve is calculated by Stephens [67] and the dotted curve by Pfeifer *et al.* [68]. The histogram is calculated by Mitsui [1].

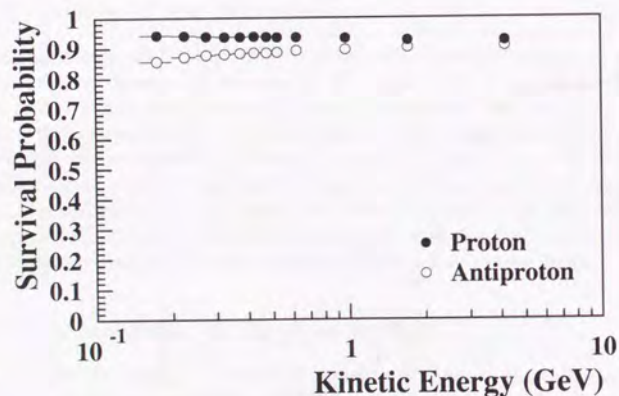


Figure 5.12: Survival probability of protons/antiprotons for 5 g/cm<sup>2</sup> of the atmosphere. The losses are due to interactions.

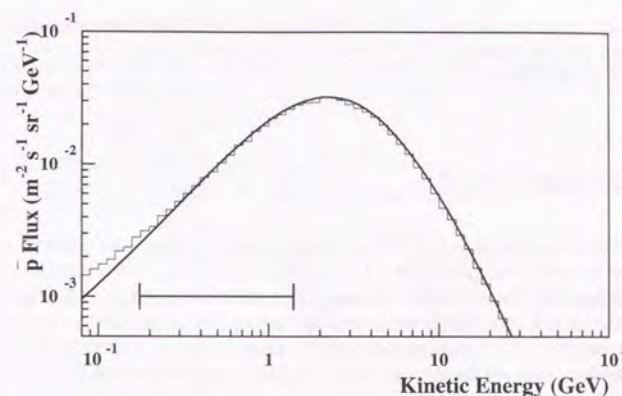


Figure 5.13: Deformation of the antiprotons spectrum due to 5 g/cm<sup>2</sup> of the residual atmosphere above the instrument, calculated by a Monte Carlo simulation. The predicted antiproton flux at the top of the atmosphere based on the standard leaky box model (the curve) is assumed as the incident spectrum. The energy losses by strong interactions produce low energy antiprotons and deform the spectrum (the histogram, made by the Monte Carlo simulation). The deformation is negligibly small at the energies covered by this experiment (the horizontal bar).

antiprotons with lower energies. This might result in a deformation of the measured spectrum. In order to see the magnitude of the effect, a Monte Carlo simulation was performed, in which the energy and the angular distribution of the secondary antiprotons was simulated at all incident antiproton energies. The antiprotons from the antiproton-nucleus interaction are produced according to the parameterization of Mistui [1], which reproduces well existing data. The resultant antiproton spectrum at 5 g/cm<sup>2</sup> of the atmospheric depth is shown in Figure 5.13 as the histogram and is compared to the assumed incident spectrum of the leaky box model (solid curve). As seen in the figure, the spectrum deformation is negligibly small even for a steep initial antiproton spectrum at least in the energy range covered by this experiment. We thus neglect this effect in deducing the spectrum at the top of the atmosphere from the obtained spectrum at 5 g/cm<sup>2</sup> of the atmospheric depth.

### 5.2.8 Re-entrant Albedo Particle

There could be 're-entrant albedo' particles which produced in the atmosphere below, moving upward at first, deflected by the geomagnetic field and enter the instrument moving downward. To check against this possibility, the trajectory of every candidate events are traced back numerically [69] through the geomagnetic



field. All of the forty three events can be traced back to the outside of the geomagnetic sphere. From this we conclude that there is no contamination of re-entrant albedo antiprotons in our events.

### 5.2.9 Geomagnetic Cutoff

Charged particles in cosmic rays suffer from the geomagnetic effect and some of them are forbidden to reach the earth. For a given direction, particle with a rigidity below a certain value is deflected by the geomagnetic field and the trajectory is inaccessible to the earth. This effect could change the shape of the cosmic ray spectrum at low energies. We examine this effect using proton events from the unbiased data samples. The geomagnetic cutoff rigidity varies from  $\sim 0.4$  GV to  $\sim 0.6$  GV during the scientific flight from Lynn Lake to Peace River. We compare the observed number of protons per unit exposure time between the first several run and the last run, because the geomagnetic cutoff rigidity is much smaller than the cutoff for protons to stop in the detector at the beginning of the flight and increases to the comparable level toward the end of the flight. As seen in the Figure 5.14, there is no distinct decrease at low energies due to the geomagnetic effect even in the last run. Thus we conclude the geomagnetic effect is negligibly small.

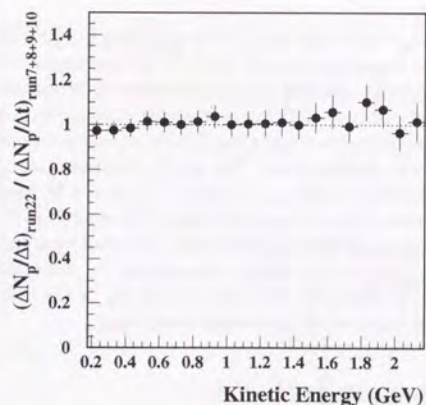


Figure 5.14: Ratio of the observed number of proton per unit time in the last run to one in the first four runs.

### 5.2.10 Summary of Corrections

The number of events observed in the instrument is converted into the expected number of incident particles  $N_{in}$  using the efficiencies:

$$\begin{aligned} N_{in}(E) &= N_{obs}(E) / \varepsilon(E) \\ \varepsilon(E) &= \varepsilon_{single}(E) \cdot \varepsilon_{trig}(E) \cdot \varepsilon_{sel}(E) \\ \varepsilon_{trig} &= \varepsilon_{TT-pattern} \cdot \varepsilon_{TT-def} \\ \varepsilon_{sel} &= \varepsilon_{track} \cdot \varepsilon_{TOF} \cdot \varepsilon_{dE/dx} \cdot \varepsilon_{mass} \cdot \varepsilon_{\beta}, \end{aligned}$$

where  $E$  is the energy at the top of the atmosphere,  $\varepsilon_{trig}$  the trigger efficiency,  $\varepsilon_{sel}$  the overall selectional efficiency. The reduced differential flux at the top of the instrument (TOI), which is a function of the energy at the top of the atmosphere, not at the top of the instrument, is then derived using the exposure factor  $S\Omega t$ :

$$F_{TOI}(E) = N_{in}(E) / S\Omega(E) t \Delta E.$$

This flux includes the atmospheric secondary component, and the primary component of the flux is derived as:

$$F'_{TOI}(E) = F_{TOI}(E) - F_{air}(E)$$

where  $F_{air}(E)$  is the atmospheric secondary flux. The flux at the top of the atmosphere is then obtained applying the correction factor for the atmospheric loss  $1/\eta$ :

$$F_{TOA}(E) = F'_{TOI}(E) / \eta(E)$$

Summarizing the above steps, one can obtain a formula for antiproton differential flux:

$$F_{TOA}(E) = \left( \frac{N_{obs}(E)}{\varepsilon(E)} \cdot \frac{1}{S\Omega(E) \cdot t \cdot \Delta E} - F_{air}(E) \right) \cdot \frac{1}{\eta(E)} \quad (5.1)$$

## 5.3 Antiproton Flux

The flux of antiprotons at the top of the atmosphere was also derived using the formula (5.1) in Section 5.2.10:

$$\begin{aligned} F_{\bar{p}} &= \left( \frac{N_{\bar{p}}^{obs}}{\varepsilon_{\bar{p}} S\Omega t} \cdot \frac{1}{\Delta E} - F_{\bar{p}}^{air} \right) \cdot \frac{1}{\eta_{\bar{p}}} \\ &= \frac{N_{\bar{p}}^{obs} - N_{\bar{p}}^{air}}{\varepsilon_{\bar{p}} S\Omega t \eta_{\bar{p}} \Delta E} \end{aligned} \quad (5.2)$$



Table 5.2: Summary of the number of antiprotons and the correction values to derive the  $\bar{p}$  flux (1).  $N_{\bar{p}}^{obs}$  is the number of observed antiprotons,  $N_{\bar{p}}^{air}$  the expected number of background antiprotons produced in the atmosphere,  $\varepsilon_{\bar{p}}S\Omega t$  the effective exposure factor, and  $\eta_{\bar{p}}$  the probability for an antiproton to penetrate 5 g/cm<sup>2</sup> of the atmosphere.

Energy (MeV)	$N_{\bar{p}}^{obs}$	$N_{\bar{p}}^{air}$	$\varepsilon_{\bar{p}}S\Omega t$ ( $\times 10^3 \text{m}^2 \text{sr} \cdot \text{sec}$ )	$\eta_{\bar{p}}$
175 - 200	0	0.008	0.694	0.861
200 - 225	1	0.025	1.818	0.865
225 - 250	1	0.037	2.236	0.869
250 - 275	1	0.046	2.353	0.872
275 - 300	0	0.055	2.432	0.875
300 - 325	1	0.064	2.488	0.877
325 - 350	1	0.074	2.529	0.879
350 - 375	1	0.083	2.561	0.880
375 - 400	0	0.093	2.587	0.882
400 - 425	1	0.102	2.609	0.883
425 - 450	0	0.112	2.627	0.884
450 - 475	1	0.121	2.641	0.885
475 - 500	2	0.131	2.649	0.886
500 - 525	0	0.140	2.653	0.887
525 - 550	2	0.149	2.650	0.887
550 - 575	0	0.158	2.643	0.888
575 - 600	0	0.166	2.631	0.889
600 - 625	2	0.174	2.614	0.889
625 - 650	2	0.181	2.595	0.890
650 - 675	0	0.189	2.574	0.890
675 - 700	1	0.195	2.553	0.891

where

$$N_{\bar{p}}^{air} = F_{\bar{p}}^{air} \varepsilon_{\bar{p}} S \Omega t \cdot \Delta E$$

is the expected number of secondary antiprotons to be observed. Table 5.2 and 5.3 summarizes the number of antiprotons and the correction factors at small intervals (bins) of kinetic energies.

For a better statistics, we cumulated these values in the energy ranges (ER); (ER1) 175 to 300 MeV, (ER2) 300 to 500 MeV, (ER3) 500 to 700 MeV, (ER4) 700 to 1000 MeV and (ER5) 1000 to 1400 MeV:

Table 5.3: Summary of the number of antiprotons and the correction values to derive the  $\bar{p}$  flux (2).  $N_{\bar{p}}^{obs}$  is the number of observed antiprotons,  $N_{\bar{p}}^{air}$  the expected number of background antiprotons produced in the atmosphere,  $\varepsilon_{\bar{p}}S\Omega t$  the effective exposure factor, and  $\eta_{\bar{p}}$  the probability for an antiproton to penetrate 5 g/cm<sup>2</sup> of the atmosphere.

Energy (MeV)	$N_{\bar{p}}^{obs}$	$N_{\bar{p}}^{air}$	$\varepsilon_{\bar{p}}S\Omega t$ ( $\times 10^3 \text{m}^2 \text{sr} \cdot \text{sec}$ )	$\eta_{\bar{p}}$
700 - 725	2	0.202	2.532	0.891
725 - 750	1	0.208	2.512	0.892
750 - 775	0	0.214	2.495	0.892
775 - 800	1	0.221	2.479	0.892
800 - 825	1	0.227	2.466	0.893
825 - 850	3	0.233	2.455	0.893
850 - 875	0	0.239	2.445	0.893
875 - 900	1	0.244	2.434	0.893
900 - 925	1	0.249	2.422	0.894
925 - 950	1	0.254	2.407	0.894
950 - 975	0	0.258	2.388	0.894
975 - 1000	0	0.261	2.363	0.894
1000 - 1025	1	0.263	2.331	0.895
1025 - 1050	1	0.263	2.291	0.895
1050 - 1075	1	0.262	2.242	0.895
1075 - 1100	1	0.260	2.183	0.895
1100 - 1125	0	0.255	2.114	0.895
1125 - 1150	1	0.250	2.035	0.896
1150 - 1175	2	0.242	1.949	0.896
1175 - 1200	1	0.233	1.851	0.896
1200 - 1225	0	0.223	1.748	0.896
1225 - 1250	0	0.212	1.642	0.896
1250 - 1275	2	0.199	1.529	0.896
1275 - 1300	0	0.186	1.414	0.896
1300 - 1325	2	0.173	1.303	0.897
1325 - 1350	3	0.160	1.193	0.897
1350 - 1375	0	0.147	1.088	0.897
1375 - 1400	0	0.134	0.987	0.897



$$F'_p(ER) \equiv \frac{\sum_{i \in ER} (N_p^{obs}(E_i) - N_p^{air}(E_i))}{\sum_{i \in ER} (\varepsilon_p(E_i) S \Omega(E_i) t \eta_p(E_i) \Delta E_i)} \quad (5.3)$$

where  $i$  is the bin number and  $E_i$  represents the energy of the  $i$ -th bin.

This time the expected value of  $F_p = F_p(E)$  in the individual elements of cumulation are obviously not the same, hence:

$$\overline{F_p}(ER) \equiv \frac{\int_{ER} F_p(E) dE}{\int_{ER} dE} \neq \frac{\int_{ER} F_p(E) \varepsilon_p S \Omega(E) t \eta_p(E) dE}{\int_{ER} \varepsilon_p S \Omega(E) t \eta_p(E) dE} \simeq F'_p(ER)$$

where  $\overline{F_p}(ER)$  is the average flux in a energy range  $ER$ . Yet

the error of the  $F'_p(ER)$  is rather smaller than the statistical errors, and we don't take that errors into account. (Actually, we will find the spectrum is flat to neglect it.) The cumulated number of antiprotons and correction factors are summarized in Table 5.4.

Table 5.4: The cumulated values and the  $\bar{p}$  flux.

ER	Energy (MeV)	$N_p^{obs}$	$N_p^{air}$	$\varepsilon_p S \Omega t \eta_p$ ( $\text{m}^2 \text{sr} \cdot \text{sec}$ )	$F_p(ER)$ ( $\text{m}^{-2} \text{sr}^{-1} \text{sec}^{-1} \text{GeV}^{-1}$ )
ER1	175 - 300	3	0.172	$1.66 \times 10^3$	$1.36 \times 10^{-2}$
ER2	300 - 500	7	0.780	$2.28 \times 10^3$	$1.36 \times 10^{-2}$
ER3	500 - 700	7	1.353	$2.32 \times 10^3$	$1.22 \times 10^{-2}$
ER4	700 - 1000	11	2.810	$2.19 \times 10^3$	$1.25 \times 10^{-2}$
ER5	1000 - 1400	15	3.461	$1.56 \times 10^3$	$1.85 \times 10^{-2}$

#### Statistical error

The statistical error of the flux was derived as the 84.13 % C.L. upper and lower limits, which correspond to  $1\sigma$  for a Gaussian distribution. The upper and lower limits  $N^U$  and  $N^L$ , were defined by the equations for a Poisson process with background [71]:

$$CL = \left( \sum_{n=0}^{n_0} e^{-(\mu_B + N^U)} \frac{(\mu_B + N^U)^n}{n!} \right) / \left( \sum_{n=0}^{n_0} e^{-\mu_B} \frac{\mu_B^n}{n!} \right) \quad (5.4)$$

$$CL = \left( \sum_{n=n_0}^{\infty} e^{-(\mu_B + N^L)} \frac{(\mu_B + N^L)^n}{n!} \right) / \left( \sum_{n=n_0}^{\infty} e^{-\mu_B} \frac{\mu_B^n}{n!} \right) \quad (5.5)$$

where  $CL$  is the confidence level,  $n_0$  the observed number and  $\mu_B$  the mean of the background. The statistical errors of the antiproton flux are summarized in Table 5.5.

Table 5.5: Statistical errors of the  $\bar{p}$  flux.

ER	Energy (MeV)	$N_p^{obs}$	$N_p^{air}$	Confidence Limits (84.13% C.L.)	$F_p(ER)$ ( $\text{m}^{-2} \text{sr}^{-1} \text{sec}^{-1} \text{GeV}^{-1}$ )	Error
ER1	175 - 300	3	0.172	$\leq 5.746$ $\geq 1.198$	$1.36 \times 10^{-2}$	$+1.41 \times 10^{-2}$ $-0.79 \times 10^{-2}$
ER2	300 - 500	7	0.780	$\leq 9.990$ $\geq 3.639$	$1.36 \times 10^{-2}$	$+0.83 \times 10^{-2}$ $-0.57 \times 10^{-2}$
ER3	500 - 700	7	1.353	$\leq 9.417$ $\geq 3.069$	$1.212 \times 10^{-2}$	$+0.81 \times 10^{-2}$ $-0.55 \times 10^{-2}$
ER4	700 - 1000	11	2.810	$\leq 12.61$ $\geq 4.927$	$1.245 \times 10^{-3}$	$+0.67 \times 10^{-2}$ $-0.550 \times 10^{-2}$
ER5	1000 - 1400	15	3.461	$\leq 16.50$ $\geq 7.710$	$1.85 \times 10^{-2}$	$+0.79 \times 10^{-2}$ $-0.61 \times 10^{-2}$

#### Systematic error

The expression of the error of the antiproton flux will be derived from equation(5.2), assuming the variables are independent:

$$\left( \frac{\Delta F_p}{F_p} \right)^2 = \left( \frac{\Delta N_p^{obs}}{N_p^{obs} - N_p^{air}} \right)^2 + \left( \frac{\Delta N_p^{air}}{N_p^{obs} - N_p^{air}} \right)^2 + \left( \frac{\Delta \varepsilon_p}{\varepsilon_p} \right)^2 + \left( \frac{\Delta(S\Omega)}{S\Omega} \right)^2 + \left( \frac{\Delta t}{t} \right)^2 + \left( \frac{\Delta \eta_p}{\eta_p} \right)^2 \quad (5.6)$$

The first term is the statistical error discussed above, and the others are systematic errors. The systematic errors are evaluated as follows:

##### 1. The geometrical acceptance $S\Omega$

The geometrical acceptance is determined by the simple geometry of the detector, and the possible systematic error in the calculated acceptance is estimated to be very much smaller than 5 %.

$$\left( \frac{\Delta(S\Omega)}{S\Omega} \right) \simeq \pm 5\%$$

##### 2. Error of the 'live time' $t$

The 'live time'  $t$  was derived by multiplying the total exposure time with the ratio of the live time to the exposure time, which is measured exactly by the ratio of the issued number of T0 trigger (gated by the "ready" status) to the number of ungated T0 triggers. The error in the live time thus is negligibly small.



$$\left(\frac{\Delta t}{t}\right) \simeq 0$$

### 3. Error of the efficiencies

The efficiencies used in deriving antiproton flux were composed of the actual selection efficiencies for protons and the ratio of efficiencies of antiproton selection to proton selection in the Monte Carlo simulations. The resultant error of the antiproton efficiency is dominated by the errors in simulation of the nuclear interactions.

We estimate the typical error in the interaction cross section to be 10 %. Hard to estimate is the error in the single track efficiency because that depends on secondary multiplicity distribution etc. We assume that the simulated inefficiency due to the nuclear interaction has a relative error of 30 %. This results in:

$$\frac{\Delta \varepsilon_{\bar{p}}}{\varepsilon_{\bar{p}}} \simeq \begin{cases} \pm 15\% & (ER1 : 175 \text{ MeV} \leq E < 300 \text{ MeV}) \\ \pm 12\% & (ER2 : 300 \text{ MeV} \leq E < 500 \text{ MeV}) \\ \pm 10\% & (ER3 : 500 \text{ MeV} \leq E < 700 \text{ MeV}) \\ \pm 10\% & (ER4 : 700 \text{ MeV} \leq E < 1000 \text{ MeV}) \\ \pm 10\% & (ER5 : 1000 \text{ MeV} \leq E < 1400 \text{ MeV}) \end{cases}$$

### 4. Atmospheric secondary antiprotons

The calculation of the atmospheric secondary antiproton flux includes uncertainties of cross section of antiproton production, the interactions of produced antiprotons in the atmosphere, and the primary proton flux. A main uncertainty comes from the primary proton flux, since proton flux at 20 ~ 100 GeV by previous experiments differ by a factor of up to 1.5. Assuming that the total uncertainty of  $N_{\bar{p}}^{air}$  is a factor 2 including other uncertainties, the corresponding systematic error will be:

$$\frac{\Delta N_{\bar{p}}^{air}}{N_{\bar{p}}^{obs} - N_{\bar{p}}^{air}} \simeq \begin{cases} +6\%/-3\% & (ER1 : 175 \text{ MeV} \leq E < 300 \text{ MeV}) \\ +13\%/-6\% & (ER2 : 300 \text{ MeV} \leq E < 500 \text{ MeV}) \\ +24\%/-12\% & (ER3 : 500 \text{ MeV} \leq E < 700 \text{ MeV}) \\ +34\%/-17\% & (ER4 : 700 \text{ MeV} \leq E < 1000 \text{ MeV}) \\ +30\%/-15\% & (ER5 : 1000 \text{ MeV} \leq E < 1400 \text{ MeV}) \end{cases}$$

### 5. Atmospheric losses of antiprotons

The losses of antiprotons due to the annihilations and the inelastic collisions in the atmosphere were estimated by Monte Carlo simulations. The errors are due mainly to the cross sections used in the simulation, which we estimate to be:

$$\frac{\Delta \eta_{\bar{p}}}{\eta_{\bar{p}}} \simeq \begin{cases} \pm 4\% & (ER1 : 175 \text{ MeV} \leq E < 300 \text{ MeV}) \\ \pm 4\% & (ER2 : 300 \text{ MeV} \leq E < 500 \text{ MeV}) \\ \pm 3\% & (ER3 : 500 \text{ MeV} \leq E < 700 \text{ MeV}) \\ \pm 3\% & (ER4 : 700 \text{ MeV} \leq E < 1000 \text{ MeV}) \\ \pm 3\% & (ER5 : 1000 \text{ MeV} \leq E < 1400 \text{ MeV}) \end{cases},$$

Table 5.6 summarizes the systematic uncertainties.

Table 5.6: Summary of systematic errors of  $\bar{p}$  flux.

Sources	ER1 (%)	ER2 (%)	ER3 (%)	ER4 (%)	ER5 (%)
Geometrical acceptance	$\pm 5$	$\pm 5$	$\pm 5$	$\pm 5$	$\pm 5$
Effective exposure time	$\pm 0$	$\pm 0$	$\pm 0$	$\pm 0$	$\pm 0$
Efficiencies .....	$\pm 15$	$\pm 12$	$\pm 10$	$\pm 10$	$\pm 10$
Atmospheric secondary $\bar{p}$	+6/-3	+13/-6	+24/-12	+34/-17	+30/-15
Atmospheric losses .....	$\pm 4$	$\pm 4$	$\pm 3$	$\pm 3$	$\pm 3$
Total .....	+17/-17	+19/-15	+27/-17	+36/-21	+32/-19

## Result

The antiproton flux obtained in the present analysis is:

$$F_{\bar{p}} = \begin{cases} (1.36^{+1.41}_{-0.79} + 0.24_{-0.23}) \times 10^{-2} \text{ m}^{-2} \text{ sr}^{-1} \text{ sec}^{-1} \text{ GeV}^{-1} & (ER1) \\ (1.36^{+0.83}_{-0.57} + 0.26_{-0.20}) \times 10^{-2} \text{ m}^{-2} \text{ sr}^{-1} \text{ sec}^{-1} \text{ GeV}^{-1} & (ER2) \\ (1.22^{+0.81}_{-0.55} + 0.32_{-0.20}) \times 10^{-2} \text{ m}^{-2} \text{ sr}^{-1} \text{ sec}^{-1} \text{ GeV}^{-1} & (ER3) \\ (1.25^{+0.67}_{-0.50} + 0.45_{-0.26}) \times 10^{-2} \text{ m}^{-2} \text{ sr}^{-1} \text{ sec}^{-1} \text{ GeV}^{-1} & (ER4) \\ (1.85^{+0.79}_{-0.61} + 0.59_{-0.35}) \times 10^{-2} \text{ m}^{-2} \text{ sr}^{-1} \text{ sec}^{-1} \text{ GeV}^{-1} & (ER5) \end{cases}$$

where the first errors are statistical and the second systematic. Figure 5.15 shows the result compared with the predicted spectra and the results of the other experiments.



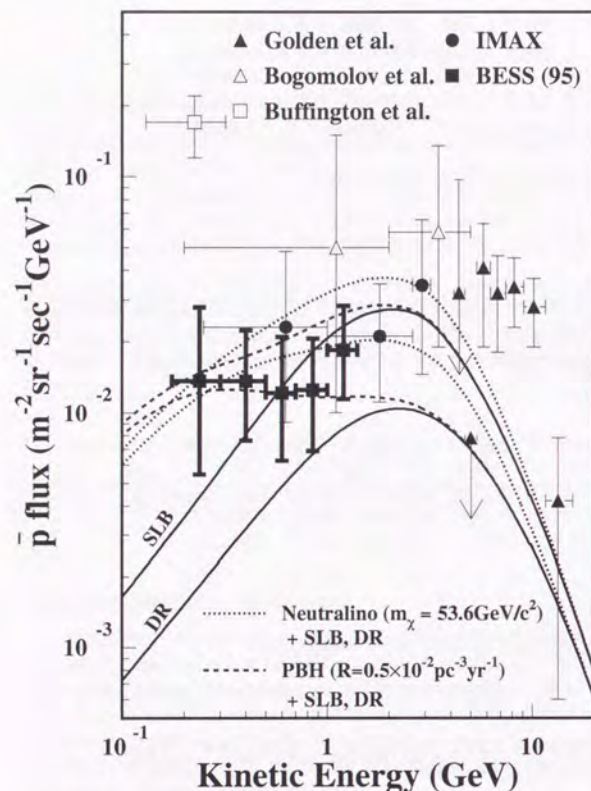


Figure 5.15: Measured  $\bar{p}$  flux in comparison with the results of the other experiments and calculations. Filled squares, the present result; filled triangles, Golden *et al.* [23, 24]; open triangles, Bogomolov *et al.* [26, 27, 24]; open squares, Buffington *et al.* [25]; filled circles, the IMAX experiment [32]. The curves labeled “SLB” and “DR” are recently calculated by Mitsui [1] based on Standard Leaky Box Model and Diffusive Reacceleration Model, respectively. The dashed curves are the calculations by Maki *et al.* [15] on the  $\bar{p}$  production by Primordial Black Holes, which are added to “SLB” or “DR” spectrum. The dotted curves are the calculations by Mitsui *et al.* [16] based on the  $\bar{p}$  production by annihilations of dark matter neutralinos, which are added to “SLB” or “DR” spectrum. All calculations are modulated to 1995 levels.

## Chapter 6

### Discussions

Our result provides the first measurement of the antiproton energy spectrum at the low energies, where the signals of primary antiprotons could be searched for.

In comparing our result with previous data and with the predictions, it should be noted that the low energy antiproton flux and the spectrum shape might change with the solar modulation. Large solar modulation of the antiproton fluxes from the primary sources are actually predicted by Mitsui *et al.* [16], while the secondary antiproton spectrum is relatively unaffected by the solar activity.

Our result is very inconsistent with the data by Buffington *et al.* [25], which flew near solar maximum. Our result is consistent with IMAX data ('92 flight), and the two experiment together exclude the large flux measured by Buffington *et al.*

The spectrum we have obtained is consistent to be flat within the present statistical accuracy, and contradicts with the pure secondary spectrum [1] from the Diffusive Reacceleration (DR) model. Our spectrum is marginally consistent with the secondary spectrum [1] from the Standard Leaky Box model.

As shown in Figure 5.15, our spectrum is consistent with the spectrum shape predicted [15] for the primary antiprotons from the Primordial Black Holes (PBH) plus the secondary antiprotons from the DR model. If fitted by this assumption, the best fit is obtained with the local PBH explosion rate of

$$R = 6.2 \times 10^{-3} \text{pc}^{-3} \text{yr}^{-1}. \quad (6.1)$$

The fit also provides the upper limit at 90 % confidence limit of  $R < 1.1 \times 10^{-2} \text{pc}^{-3} \text{yr}^{-1}$ .

We note that  $R$  value of  $6.2 \times 10^{-3}$  is 8 orders of magnitude lower than the upper limit obtained by the searches for TeV  $\gamma$ -ray bursts [72], and is hundred times lower than the upper limit derived from arguments on the anisotropy of the diffuse  $\gamma$ -ray flux [73]. The  $R$  parameter represents the local (within 2 kpc) explosion rate of PBH with the initial mass of  $5 \times 10^{14}$  g, which were created in the early Universe and exhausted their life time recently. Assuming the globally uniform PBH distribution in the Universe and the standard PBH initial mass spectrum,  $R$  value of  $6.2 \times 10^{-3}$  corresponds to an average PBH density in the Universe of  $\Omega = 2 \times 10^{-9}$ , which is a factor of  $\sim 20$  below the upper limit deduced from the cosmological diffuse  $\gamma$ -ray background [74].



As shown in Figure 5.15, our spectrum is also consistent with the spectrum shape [16] predicted for the antiprotons from the annihilation of neutralino dark matter, although there exist large uncertainties [16] in the absolute flux prediction.

## Chapter 7

### Conclusions

In conclusion, BESS experiment has succeeded to provide the first measurement of cosmic antiproton spectrum below 1.4 GeV based on clearly identified forty three antiprotons. The observed spectrum is interestingly flat and is consistent with the existence of a small primary antiproton component at a level below the limits given by previous experiments. However, the present large statistical error does not allow us to draw a firm conclusion. Much better data from future flights are very much needed.

We do have plans to improve the detector. A factor 2 more data per flight are envisaged by improving the data taking and the trigger efficiencies. The improved time-of-flight measurements and the addition of an Aerogel Čerenkov counter will enable us to identify the antiprotons up to 3 GeV. These detector improvements, together with the expected enhancement [16] of the primary antiproton fluxes at the solar minimum period now approaching, will make it possible to perform a very sensitive search for antiprotons from novel primary sources such as PBH and the neutralino annihilation. We therefore envisage either to establish the existence of a primary antiproton component, or to place a strong upper limit on such component, and at the same time to measure the secondary antiproton flux in order to determine the propagation model of the cosmic rays.



## Acknowledgments

I wish to express my sincere thanks to Professor S. Orito who has led the BESS experiment, for his guidance throughout my research reported in this thesis. I also wish to gratefully appreciate Professor A. Yamamoto who has managed the campaign and lead it to a success. The analysis were done owing a lot to Prof. S. Orito, K. Yoshimura and I. Ueda. I would like to acknowledge them for their suggestions and helpful discussions and assistance at the various stages of the analysis.

I would like to thank all the BESS colleagues for their effort to make a success of the experiment, especially M. Nozaki, M. Imori and T. Yoshida for their overall contributions; K. Anraku, T. Saeki, M. Motoki, H. Matsumoto, T. Sanuki, N. Takimi, M. Ooba, M. Kobayashi, and K. Suzuki for their excellent works on the experiment. I also thank Y. Makida, K. Tanaka, N. Kimura, and the other staffs who have worked on the superconducting magnet; J. Suzuki, Y. Higashi, Y. Ajima, S. Koizumi, and all the other KEK staffs who contributed to the construction of the BESS instruments. I am grateful to D. Richter for his technical support. I wish to acknowledge the contributions to the analysis from K. Anraku, T. Saeki, M. Motoki, T. Sanuki and Y. Nishihara. I am also indebted to K. Shimamura, T. Haga, T. Tsunoda, H. Honda and all the other people who were once involved in the experiment. It is a pleasure to express my appreciation to J. Ormes, A. Moiseev, R. Streitmatter, J. Mitchell, N. Yajima, T. Yamagami, E. S. Seo, B. Kimbell, and S. Stochaj, and the late Prof. R. Golden, who are the collaborators of the experiment.

I greatly appreciate helpful suggestions from Prof. J. Nishimura, discussions with T. Mitsui and K. Maki about the theoretical calculations. I also thank the people in Lynn Lake for their kind hospitality during our stay there.

Furthermore, I am grateful to Dr. V. Jones and all other people at NASA who supported BESS, and to the balloon campaign team from the National Scientific Balloon Facility for their professional and skillful work in carrying out the BESS flights. I greatly acknowledge Prof. A. Nishida, Director General of ISAS, Prof. H. Sugawara, Director General of KEK, and Prof. S. Iwata of KEK for their support and encouragement. Sincere thanks go to International Center for Elementary Particle Physics (ICEPP) of University of Tokyo for kindly allowing me to use their workstations. The data of the CLIMAX neutron monitor were provided by Space Physics Data System of University of Chicago, supported by National Science Foundation Grant ATM-9420790. The BESS experiment has been supported by Monbusho International Scientific Research Grant and Scientific Research Grant, Kurata Research Grant, and Sumitomo Research Grant.



## References

- [1] Mitsui, T., Doctoral thesis, Univ. of Tokyo (1996).
- [2] Gaisser, T. K., and Maurer, R. H., Phys. Rev. Lett. **30**, 1264 (1973).
- [3] Gaisser, T. K., and Mauger, B. G., Ap. J. **252**, L57 (1982).
- [4] Simon, M. and Heinbach, U., in *"Cosmic Rays, Supernovae and the Interstellar Medium"*, edited by Shapiro, M. M., *et al.*, p.137. ( Kluwer Academic Publishers, Dordrecht/Boston/London, 1991).
- [5] Gaisser, T. K., and Schaefer, R. K., Ap. J. **394**, 174 (1992).
- [6] Heinbach, U. and Simon, M., Ap. J. **441**, 209 (1995).
- [7] Hawking, S., Mon. Not. R. astr. Soc. **152**, 75 (1971).
- [8] Carr, B. J., Hawking, S. W., Mon. Not. R. astr. Soc. **168**, 399 (1974).
- [9] Carr, B. J., in *"Observational and Theoretical Aspects of Relativistic Astrophysics and Cosmology"*, edited by Sanz, J. L. and Goicoechea, L. J., p.1. (World Scientific Publishing Co. Pte. Ltd., Singapore, 1985).
- [10] Hawking, S. W., Nature **248**, 30 (1974).
- [11] Hawking, S. W., Commun. math. Phys. **43**, 199 (1975).
- [12] Kiraly, P., Wdowczyk, J., and Wolfendale, A. W., Nature **293**, 120 (1981).
- [13] Turner, M.S., Nature **297**, 379 (1982).
- [14] MacGibbon, J. H. and Carr, B. J. Ap. J. **371**, 447 (1991).
- [15] Maki, K., Mitsui, T., and Orito, S., Phys. Rev. Lett. **76**, 3474 (1996).
- [16] Mitsui, T., Maki, K., and Orito, S., Phys. Lett. **B389**, 169 (1996).
- [17] Silk, J., and Srednicki, M., Phys. Rev. Lett. **53**, 624 (1984).
- [18] Aizu, H., *et al.*, Phys. Rev. **121**, 1206 (1961).
- [19] Apparao, M. V. K., Nature **215**, 727 (1967).



- [20] Apparao, K. M. V., *et al.*, Proc. 19th Intl. Cosmic Ray Conf. (La Jolla), **2**, 326 (1985).
- [21] Bogomolov, E. A., *et al.*, Proc. 16th Intl. Cosmic Ray Conf. (Kyoto), **1**, 330 (1979).
- [22] Golden, R. L., *et al.*, Phys. Rev. Lett. **43**, 1196 (1979).
- [23] Golden, R. L., *et al.*, Astrophysical Letters, **24**, 75 (1984).
- [24] Stephens, S. A. and Golden, R. L., Space Sci. Rev. **46**, 31 (1987).  
Stephens, S. A. and Golden, R. L., Astron. Astrophys. **202**, 1 (1988).
- [25] Buffington, A., *et al.*, Ap. J. **248**, 1179 (1981).
- [26] Bogomolov, E. A., *et al.*, Proc. 20th Intl. Cosmic Ray Conf. (Moscow), **2**, 72 (1987).
- [27] Bogomolov, E. A., *et al.*, Proc. 21st Intl. Cosmic Ray Conf. (Adelaide), **3**, 288 (1990).
- [28] Ahlen, S. P., *et al.*, Phys. Rev. Lett. **61**, 145 (1988).  
Barwick, S. W., *et al.*, Proc. 21st Intl. Cosmic Ray Conf. (Adelaide), **3**, 273 (1990).  
Salamon, M. H., *et al.*, Ap. J. **349**, 78 (1990).
- [29] Moats, A., *et al.*, Proc. 21st Intl. Cosmic Ray Conf. (Adelaide), **3**, 284 (1990).
- [30] Streitmatter, S. J., *et al.*, Proc. 21st Intl. Cosmic Ray Conf. (Adelaide), **3**, 277 (1990).  
Stochaj, S. J., Ph.D. thesis, Univ. of Maryland (1990).
- [31] Hof, M., *et al.*, Ap. J. **467**, L33 (1996). Also, Proc. 24th Intl. Cosmic Ray Conf. (Rome), **3**, 60 (1995).
- [32] Mitchell, J. W., *et al.*, Phys. Rev. Lett. **76**, 3057 (1996). Also, Proc. 24th Intl. Cosmic Ray Conf. (Rome), **3**, 72 (1995).
- [33] Yoshimura, K., *et al.*, Phys. Rev. Lett. **75**, 3792 (1995).  
Also, Yoshimura, K., Doctoral thesis, Univ. of Tokyo (1995).  
Orito, S., Nucl. Phys. B (Proc. Suppl.) **43**, 237 (1995).
- [34] Ueda, I., Doctoral thesis, Univ. of Tokyo (1995).
- [35] Orito, S., Proc. of the ASTROMAG Workshop, KEK Report 87-19, 111 (1987).
- [36] Yoshida, T., *et al.*, Proc. of the Second Workshop on Elementary-Particle Picture of the Universe, KEK, 142 (1988).

- [37] Yamamoto, A., editor, Proc. of the 3rd BESS Workshop, KEK Proceedings 92-2 (1992).
- [38] Yamamoto, A., *et al.*, Adv. Space Res. **14**(2), 75 (1994).
- [39] Nozaki, M., *et al.*, Proc. 24th Intl. Cosmic Ray Conf. (Rome), **3**, 579 (1995).
- [40] Yamamoto, A., *et al.*, Adv. Space Res. **17**(9), 101 (1996).
- [41] Yamamoto, A., editor, Proc. of the 5th BESS Workshop, KEK Proceedings 94-11 (1995).
- [42] Yoshida, T., *et al.*, in preparation.
- [43] Yamamoto, A., *et al.*, IEEE Trans. on Magnetics **24**, 1421 (1988).
- [44] Mito, T., *et al.*, IEEE Trans. on Magnetics **25**, 1663 (1989).
- [45] Makida, Y., *et al.*, Adv. in Cryogenic Engineering **37**, 401 (1992).
- [46] Drumm, H., *et al.*, Nucl. Instr. and Meth. **176**, 333 (1980).
- [47] Allison, J., *et al.*, Nucl. Instr. and Meth. A **236**, 284 (1985).
- [48] Anraku, K., *et al.*, IEEE Trans. on Nuclear Science NS-40, 717 (1993).
- [49] Massam, T., CERN 76-21 (1976).
- [50] Matsumoto, H., *et al.*, IEEE Trans. on Nuclear Science NS-43, 2195 (1996).
- [51] Imori, M., *et al.*, IEEE Trans. on Nuclear Science NS-39, 1389 (1992).
- [52] Imori, M., *et al.*, IEEE Trans. on Nuclear Science NS-40, 913 (1993).
- [53] Sacki, T., *et al.*, Nucl. Instr. and Meth. A **355**, 506 (1995).
- [54] Anraku, K., *et al.*, IEEE Trans. on Nuclear Science NS-39, 987 (1992).
- [55] Yoshida, T., Proc. of the 5th BESS Workshop, KEK Proceedings 94-11, 31 (1994).
- [56] Goossens, M., *ZEBRA - Overview of the ZEBRA system*, CERN Program Library Q100/Q101. CERN, 1993.
- [57] Application Software Group, *HEPDB - Database Management Package*, CERN Program Library Q180. CERN, 1993.
- [58] Karimäki, V., Nucl. Instr. and Meth. A **305**, 187 (1991).
- [59] Bruyant, F., *et al.*, *GEANT - Detector Description and Simulation Tool*, CERN Program Library W5013. CERN, 1993.



- [60] Nakamura, K., *et al.*, Phys. Rev. Lett. **52**, 731 (1984).
- [61] Kuzichev, V. F., Lepikhin, Yu. B., and Smirnitsky, V.A., Nucl. Phys. A**576**, 581 (1994).
- [62] Gorin, Yu. P., *et al.*, Yad. Fiz. **18**, 336 (1973).
- [63] Allaby, J. C., *et al.*, Yad. Fiz. **12**, 538 (1970).
- [64] Afonas'ev, V.N., *et al.*, Yad. Fiz. **40**, 34 (1984).
- [65] Afonas'ev, V.N., *et al.*, Yad. Fiz. **47**, 1656 (1988).
- [66] Carroll, A. S., *et al.*, Phys. Lett. B**80**, 319 (1979).
- [67] Stephens, S. A., accepted for publication in Astroparticle Physics (1996).
- [68] Pfeifer, Ch., Roesler, S. and Simon, M., Phys. Rev. C**54**, 882 (1996).
- [69] Inoue, A. *et al.*, The bulletin of the Institute for Space and Astronautical Science, the special issue on the scientific ballooning (in Japanese) p.79 (1981).  
The original source code used in our calculation is provided by Dr. Shibata of Aoyama Gakuin University, based on the above reference.
- [70] Seo, E. S., *et al.*, Ap. J. **378**, 763 (1991).  
Also, Seo, E. S. Ph.D. thesis, Louisiana State Univ. (1991)
- [71] Particle Data Group, Phys. Rev. D**54**, 166 (1996).
- [72] Alexandreas, D. E., *et al.*, Phys. Rev. Lett. **71**, 2524 (1993).
- [73] Wright, E.L., Ap. J. **459**, 487 (1996).
- [74] Page, D. N. and Hawking, S. W., Ap. J. **206**, 1 (1976).  
Halzen, F., Zas, E., MacGibbon, J. H., and Weekes, T. C., Nature (London) **353**, 807 (1991).



卒論製本  
ヤマザキ  
☎ (03) 3956-1681